GROUND-PENETRATING RADAR AND THERMAL MODELING OF ACTIVE LAYER THAW BENEATH ARCTIC STREAMS

By

Troy Richard Brosten

A dissertation

submitted in partial fulfillment

of the requirements for the degree of

Doctor of Philosophy, Geophysics

Boise State University

September 2008

to my family

ACKNOWLEGMENTS

Completion of this dissertation was achieved with the help from numerous individuals for whom I am eternally grateful. I want to thank my academic advisor and dissertation committee chair, Dr. John Bradford, for his guidance and expertise. He also helped ensure my financial stability throughout my stay, provided me with flexibility and encouragement to contribute to and learn from research projects outside of my dissertation work, and proved to be a challenging adversary in the occasional racquetball game which helped provide stress relief as I tried to minimize impending bruises from a little blue ball. I'm grateful to Dr. James McNamara for bringing me to Boise by inviting me to contribute to an arctic research project that turned out to be the focal point of my research and also served as a committee member. I thank my remaining committee members, Dr. Kasper van Wijk and Dr. James Ferguson, for their insight and helpful comments in addition to Dr. Peter Annan who volunteered to become my external reviewer and provided me with additional, insightful, comments. Dr. Paul Michaels also provided valuable feedback and advice.

I thank the Arctic Hyporheic Team: Jay Zarnetske, Dr. Michael Gooseff, Dr. William Bowden, Morgan Johnston, Ken Hill, Julia Larouche, Joel Homan, and Karen Cozzetto who helped make fieldwork on the North Slope productive, enjoyable, and memorable. I thank my coauthors Dr. John Bradford, Dr. James McNamara, Jay Zarnetske, Dr. Michael Gooseff, and Dr. William Bowden, who helped prepare and

submit chapter 2, “Profile of temporal thaw depths beneath two arctic stream types using ground-penetrating radar”, to *Permafrost and Periglacial Processes* (Brosten et al., 2006). I thank past and present fellow graduate students: Carlyle Miller, Scott Hess, Vijay Raghavendra, Joel Homan, Mike Whitson, Monty Busbee, Mike Thoma, Josh Nichols, Joel Brown, Emily Hinz, Gene Kurz, and many more who provided helpful comments and entertainment throughout this process. I also thank Carlyle Miller, now Dr. Miller, who helped me over many Matlab hurtles and expanded my knowledge on CSAMT methods through many day of fieldwork and office discussions.

Special thanks is expressed to my wife Lisa who has always been supportive throughout many long nights-to-make-the-deadline and weeks of fieldwork and, of course, her exceptional pies which helped fuel me through many of those long nights. Through her passion to expand literary horizons I’ve developed a renewed appreciation for the English language. Her exceptional grammar and English writing skills resulted in significantly improved manuscripts.

I am grateful to the Arctic LTER program, Toolik Field Station camp personnel, VECO Polar Resources, and Air Logistics for assistance with field logistics. Funding was provided by a departmental fellowship from the Department of Geosciences, Boise State University, the US National Science Foundation Grant No. OPP 03-27440, the USDA (Grant NRI 2004-35102-14802), and support from the Landmark University Grant Program.

AUTOBIOGRAPHICAL SKETCH

My research interests include electrical and electromagnetic methods and their application to solve hydrological, environmental, and exploration problems. Through my dissertation work I've also developed a love/hate interest in heat flow modeling. In my free time I enjoy golfing, skiing, camping, cooking, gardening, biking, racquetball, and pretty much anything that makes me appear as if I know what I'm doing.

Summary of Life Events

- 1972 (March): Born in Plains, MT.
- 1990 (June): Graduated from Bigfork High School, Bigfork, MT.
- 1996 (May): Completed B.S. in Earth Science at Montana State University, Bozeman, MT.
- 1996 (two weeks after graduation): Enlisted in the U.S. Army as a Combat Engineer. Spent my enlistment time in Germany with occasional deployments to Bosnia.
- 1999 (March): Hydrology technician at Colville National Forest, Colville, WA.
- 2002 (May): Completed M.S. in Geophysical Engineering at Montana Tech, Butte, MT.
- 2002 (May): Began working for the U.S. Army Corps of Engineers as a Research Geophysicist, Vicksburg, MS.
- 2004 (August): Started Ph.D. program in Geophysics at Boise State University, Boise, ID.
- 2005 (September): Married to Lisa Roullard at the Botanical Garden, Boise, ID.

- 2008 (June): The birth of my daughter, Ashley Rose Brosten.

- 2008 (September): Completed Ph.D. in Geophysics at Boise State University, Boise, ID.

ABSTRACT

Seasonal thaw depth beneath arctic streams significantly impacts physical and biological processes within arctic stream environments. The impact of greater seasonal thaw for extended periods of time can alter ecosystems that have, in the past, resulted from more prevalent permafrost environments. Effects of climatic change on arctic stream environments necessitate the need for more information on characteristics of seasonal thaw and processes that occur within the thawed layer. Multiple ground-penetrating radar (GPR) methods and one-dimensional (1D) thermal modeling were used to investigate seasonal thaw beneath arctic streams and determine the dominant thermal process.

Study sites were selected to include stream reaches that span a range of geomorphologic conditions in rivers and streams on Alaska's North Slope. Results from seasonal time-lapse common-offset GPR transects, gathered throughout the summer season of 2004, illustrated that low-energy stream environments react slowly to seasonal solar input and maintain thaw thicknesses longer throughout the late season. Thaw depths beneath high-energy streams respond quickly in the beginning of the season and appear to decrease just as quickly over the late season period.

Continuous multi-offset (CMO) GPR method improves the quality of subsurface images through stacking and velocity filtering and provides measurements of vertical and lateral velocity distributions. Detailed velocities were estimated from CMO transects,

gathered in August 2005, using reflection tomography processing methods. Resulting velocity tomograms were then used to estimate water content and porosity using the Topp equation. Porosity estimates were then used to help constrain a 1D finite-difference thermal model.

Within the high-energy stream environments three-dimensional (3D) GPR data illustrate greater thaw depths beneath riffle and gravel bar features relative to the neighboring pool features. Due to differences in thermal properties the low-energy stream sites indicate the opposite: greater thaw depths beneath pools and thinner thaws beneath the connecting runs. Results provide detailed 3D geometry of active layer thaw depths that can greatly improve hydrological studies seeking to quantify transport and biogeochemical processes that occur within the hyporheic zone.

Using the finite-difference approach a 1D heat transport model with phase change was developed to estimate seasonal temperatures beneath two arctic streams to determine the dominant thermal process occurring beneath the stream sites. The model was driven by stream water or near-surface temperature data recorded at select stream sites near Toolik Field Station, AK, for the summer months of 2004 and 2005. Model temperatures were calibrated to measured temperatures at corresponding depths and evaluated against interpreted thaw depths from cross-sectional GPR images gathered over the 2004 summer season. Results are in reasonable agreement with observed temperatures and GPR thaw depth estimates and imply thaw processes dominated by thermal conduction. Discrepancies between model and observed values are likely due to homogenous soil

property assumptions, oversimplified convection influence assumptions, and deviations from the 1D model.

TABLE OF CONTENTS

LIST OF TABLES

LIST OF FIGURES

PREFACE

The individual chapters within this dissertation were prepared with the intent to eventually publish the material from each chapter in the peer-reviewed literature. The chapters are essentially stand-alone manuscripts with references made to material in other chapters when appropriate. The material presented adheres to a common theme of characterizing active layer thaw beneath arctic streams using ground-penetrating radar and thermal modeling methodologies. The introductory discussion (Chapter 1) describes the general layout of the dissertation and how each individual chapter is tied into the central theme of the dissertation.

1 INTRODUCTION

A century long warming trend in the Alaskan arctic [*Lachenbruch et al.*, 1982; *Lachenbruch and Marchall*, 1986] has caused permafrost warming, and in some areas, thawing [*Osterkamp*, 1995; *Osterkamp and Romanovsky*, 1999; *Osterkamp et al.*, 2000; *Zhang and Osterkamp*, 1993]. The impact of warming permafrost can significantly alter ecosystems that have relied on permafrost as a foundation [*Jorgenson et al.*, 2000]. Future assessment of warming permafrost and active layer thaw on ecosystems requires an improved understanding and characterization of these processes within specific environmental settings. This study presents methodologies that characterize the active layer thaw beneath arctic stream environments through multiple ground-penetrating radar (GPR) methods and numerical one-dimensional (1D) thermal modeling providing significant information about the subsurface architecture which can aid hydrological and biological studies within arctic stream environments. Knowledge of the active layer is particularly important in the arctic where the seasonal thaw may limit subsurface flow and biogeochemical cycling within stream ecosystems.

Numerous studies have characterized active layer thaw and permafrost features of arctic terrestrial environments through the use of common-offset GPR methods [*Annan and Davis*, 1976; *Arcone and Delaney*, 1982; *Arcone et al.*, 1993; *Arcone et al.*, 1998b; *Arcone and Delaney*, 2003; *Delaney et al.*, 1990; *Doolittle et al.*, 1990; *Doolittle et al.*, 1992; *Hinkel et al.*, 2001]. Other studies have utilized temperature measurements and

modeling of the thermal processes to characterize the active layer and warming permafrost [*Kane et al.*, 1991; *Lachenbruch et al.*, 1982; *Osterkamp and Romanovsky*, 1996; 1997; *Romanovsky and Osterkamp*, 1995; 2000; *Woo and Xia*, 1996; *Zhang et al.*, 1996; *Zhang and Stamnes*, 1998]. Few studies have extended these methodologies to characterize active layer thaw and its interaction with subsurface water flow beneath arctic stream environments [*Arcone et al.*, 1992; *Arcone et al.*, 1998a; *Best et al.*, 2005; *Bradford et al.*, 2005; *Delaney et al.*, 1990; *Schwamborn et al.*, 2002] and fewer still have used non-invasive geophysical results to inform and validate thermal models.

The movement of stream water flowing into the near sub-surface and returning to the stream channel is known as hyporheic exchange flow. The spatial extent of this exchange defines the hyporheic zone (Figure 1.1). Hyporheic exchange processes have a significant effect on biogeochemical cycling within stream ecosystems [*Gooseff et al.*, 2002; *Jones et al.*, 1995; *Mulholland et al.*, 1997]. These processes have been studied in temperate stream systems [*Arntzen et al.*, 2006; *Harvey and Bencala*, 1993; *Hill et al.*, 1998; *Kasahara and Wondzell*, 2003; *Vervier et al.*, 1993; *Wondzell and Swanson*, 1999; *Wroblicky et al.*, 1998] and, to a lesser extent, in arctic stream environments [*Edwardson et al.*, 2003; *Greenwald et al.*, 2008; *Zarnetske et al.*, 2007; *Zarnetske et al.*, 2008]. Hydrological and biological studies of hyporheic flow typically involve point measurements through piezometer installation which provides an inadequate understanding of the subsurface architecture. A critical component to these studies includes knowledge of the 3D distribution of the depth of thaw through time.

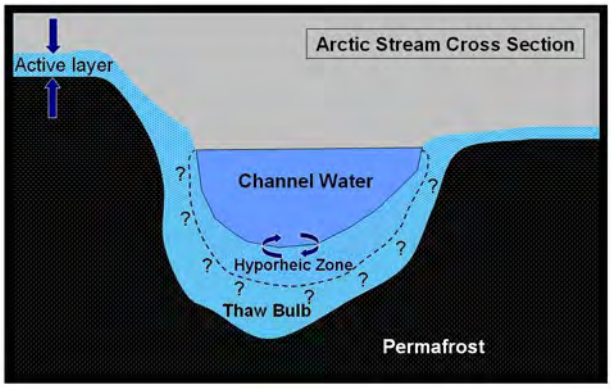

Figure 1.1. The extent of the hyporheic zone is defined as the area where channel water and subsurface water mix. In arctic streams the hyporheic zone exists within the seasonal thaw layer, defined as the thaw bulb beneath the streams [*Greenwald et al.*, 2008].

Geophysical methods present opportunities to collect many times more data, non-invasively, and in a shorter amount of time. The use of geophysical methodologies to characterize problems in other scientific disciplines has increased, however this area of interdisciplinary collaboration is still in its infancy. Immense opportunities for further advancements exist.

The following chapters document GPR methodologies and results from time-lapse, multi-offset, and 3D imaging used to characterize the active layer beneath arctic stream sites (Figure 1.2). GPR results were used to inform and validate thermal models with the intent to determine the dominant thermal process that controls the development of the active layer. While each of the GPR methods presented in these studies are not new, in of themselves, their application to study and characterize the development of the active layer thaw and hyporheic flow beneath arctic streams is unique and original.

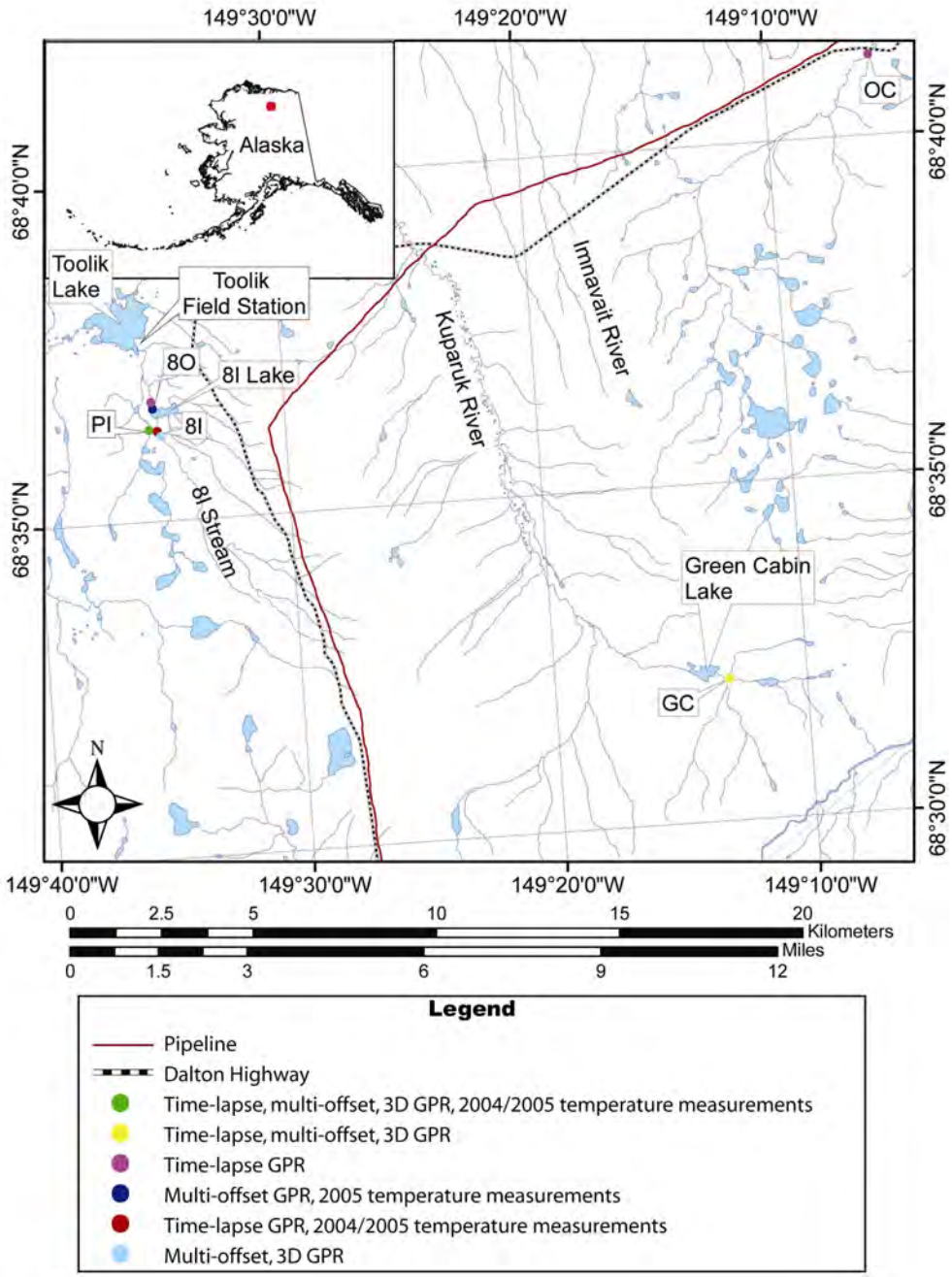

Figure 1.2. Locations of all study sites. Note the different survey methods which varied by site.

1.1 Time-Lapse Ground-Penetrating Radar

Geophysical time-lapse studies can provide an immense amount of information on subsurface conditions. Advances in collection and processing methods have significantly improved the feasibility of time-lapse experiments with numerous successes, illustrating an increased understanding of subsurface processes through these monitoring methods [*Lane et al.*, 2006; *Lumley*, 2001; *MacBeth et al.*, 2006; *Miller et al.*, 2008]. One distinct advantage of a time-lapse investigation is the collection of multiple datasets, compared to the usual single snapshot image. Differences between images provide information about subsurface processes and property interactions.

Chapter 2 presents a common-offset GPR time-lapse study conducted at five stream sites on the North Slope of Alaska and has been published in *Permafrost and Periglacial Processes* [*Brosten et al.*, 2006]. The purpose of the study was to provide a time series of the evolution of the active layer thaw under peat-bed and alluvial stream types over open waters during the summer season of 2004. GPR transects were acquired weekly during the first summer month, June, and then on a monthly basis until September. Time-lapse images proved to be advantageous where a distinct moving boundary, noted from image to image, is interpreted as the active layer/permafrost reflection, rather than misinterpreting water bottom multiples as the thaw front.

1.2 Multi-Offset Ground-Penetrating Radar

Conventional GPR surveys are mostly acquired with a constant transmitter-receiver offset. EM velocities for the GPR images are estimated by one of three methods:

1. Radar reflectors are directly correlated with significant boundaries identified in the borehole data. Drawbacks include misinterpretation, limited lateral resolution, and the expense of deploying a destructive method.
2. Moveout of scattering diffractions within the data image can be used to estimate velocities. However, diffractions are not always present and when they are, their distribution determines the limits of the lateral and vertical velocity estimates.
3. Lastly, sparsely located common-midpoint (CMP) soundings are gathered (perhaps at one or two points) along the survey line and then normal moveout (NMO) analysis is used to estimate root-mean-square (rms) velocity distribution. Next, Dix inversion computes interval velocities from the rms velocities [*Dix*, 1955]. Drawbacks to the latter method include limited lateral velocity control and errors associated with NMO assumptions which include planar flat reflections and small velocity gradients [*Al-Chalabi*, 1973; *Al-Chalabi*, 1974; *Yilmaz*, 2001].

Several studies show significantly improved images when an entire GPR survey is acquired with CMP geometry [*Bradford*, 2003; 2004; *Bradford*, 2006; *Bradford and Deeds*, 2006; *Deeds and Bradford*, 2002; *Fisher et al.*, 1992; *Greaves et al.*, 1996; *Liberty and Pelton*, 1994; *Pipan et al.*, 1999; *Pipan et al.*, 2003]. With CMP acquisition, multi-trace reflection seismic processing methods can be applied for accurate depth imaging from laterally and vertically continuous GPR velocity measurements. An

additional advantage of CMP data includes improved suppression of coherent and random noise.

Chapter 3 illustrates continuous multi-offset (CMO) GPR methods used to obtain spatially distributed porosity estimates in the substream environment. Results are utilized to image the hyporheic zone and subsurface porosity from transects collected in August 2005, across four arctic streams north of the Brooks Range, AK, and one transect gathered on September, 2007, across a temperate stream site within the Sawtooth Mountains near Boise, ID. The objective of this study was to accurately image GPR velocity structure, then use these measurements to estimate porosity estimates using the petrophysical relationship defined by the Topp equation [*Topp et al.*, 1980]. This information will provide input to future hyporheic flow and heat flow models to better understand hyporheic zone processes.

1.3 3D Ground-Penetrating Radar

Advances in data processing software and data acquisition instruments have enabled research methods to expand to three-dimensional (3D) data collection and analysis for a more complete characterization of subsurface structures. 3D GPR has been used in multiple research areas including archaeology [*Grasmueck et al.*, 2004; *Leckebush*, 2003; *Leucci and Negri*, 2006; *Negri and Leucci*, 2006], geology [*Asprion and Aigner*, 1999; *Beres et al.*, 1995; *Guidry et al.*, 2007; *Kostic and Aigner*, 2007], hydrology [*Bradford and Wu*, 2007; *Bradford*, 2008; *Kruse et al.*, 2006], and geological engineering applications [*Anderson et al.*, 2007; *Grasmueck*, 1996]; however the benefits

provided by 3D GPR to map near-surface structures in permafrost environments has not, as of yet, been fully exploited. One recent investigation took advantage of the dielectric contrast between ice wedges and the surrounding material using 3D GPR to interpret the 3D geometry of ice-wedge polygons on the Arctic Coastal Plain of northern Alaska [*Munroe et al.*, 2007].

2D groundwater flow modeling efforts [*Zarnetske et al.*, 2008] found that hyporheic exchange, within arctic streams, occurs up to a threshold depth primarily determined by hydraulic head gradients established by the stream morphology. Hyporheic studies seeking to quantify water storage and biogeochemical processes could be greatly improved with the addition of a more complete characterization of the active layer geometry provided by a 3D GPR survey.

Chapter 4 presents 3D GPR data collection methodology applied to acquire a volume dataset in August 2005, at three stream sites within the Kuparuk watershed on the North Slope, AK. This chapter expands on knowledge obtained from previous studies on arctic stream characterization [*Bradford et al.*, 2005; *Brosten et al.*, 2006] using 3D GPR to provide detailed variations of the seasonal thaw depth within changes in local streambed features. Results can be used to improve groundwater flow and particle tracking models seeking to quantify hyporheic exchange processes within arctic streams.

1.4 Thermal Modeling

Thermal modeling has been used extensively to visualize past climate changes [*Lachenbruch et al.*, 1982; *Lachenbruch and Marchall*, 1986] and evaluate and predict

future climate trends [*Kane et al.*, 1991]. Additional investigations have studied the effects of snow cover on the thermal regime of the active layer and permafrost within terrestrial environments [*Goodrich*, 1982; *Zhang et al.*, 1996; *Zhang and Stamnes*, 1998]. Few studies have employed non-invasive surface geophysical methods to inform thermal models. Specifically, amounts of unfrozen water content within the active layer, provided by multi-offset GPR transects, can significantly improve thermal model results where models not accounting for effects from unfrozen water will produce large errors [*Riseborough*, 2002; *Romanovsky and Osterkamp*, 2000].

There are also a limited number of published investigations of thermal processes beneath arctic streams. Thermal modeling can provide valuable insight on the dominant affects from thermal conduction and advective processes on the development and expansion of the active layer and its affects on hyporheic processes. Wankiewicz [1982] studied thermal processes of a river talik beneath two arctic rivers through modeling measured subsurface temperatures in April, August, and November 1977-1978. Wankiewicz [1982] concluded conduction as the dominated heat transfer process at one site while macrodispersion of heat from ground water flow was the dominate process at the second site.

Chapter 5 illustrates a 1D heat transport model, with phase change developed to predict summer month temperatures beneath three stream sites on the North Slope, AK. Observed stream water temperatures or near-surface temperatures were used to drive the model to predict active layer seasonal thaw from early June to mid October 2004 and mid-May to mid-October 2005. Multi-offset GPR transects helped inform the models

with volumetric water content estimates. Additionally, seasonal time-lapse GPR transects, gathered in 2004, are compared to modeled thaw depth estimates for validation.

2 PROFILES OF TEMPROAL THAW DEPTHS BENEATH TWO ARCTIC STREAM TYPES USING GROUND-PENETRATING RADAR

2.1 Abstract

Thaw depths beneath arctic streams may have significant impact on the seasonal development of hyporheic zone hydraulics. To investigate thaw progression over the 2004 summer season we acquired a series of GPR profiles at nine sites from May - September, using 100, 200, and 400 MHz antennas. We selected sites with the objective of including stream reaches that span a range of geomorphologic conditions on Alaska's North Slope. Permafrost depths interpreted from GPR data were constrained by both recorded subsurface temperature profiles and by pressing a metal probe through the active layer to the point of refusal where the active layer is defined as the seasonal thaw layer that resides on top of the permafrost. We found that low-energy stream environments react much more slowly to seasonal solar input and maintain thaw thicknesses longer throughout the late season whereas thaw depths increase rapidly within high-energy streams at the beginning of the season and decreased over the late season period.

2.2 Introduction

Streams on the North Slope of Alaska can be broadly classified as peat or alluvial. This streambed condition can be considered a geomorphologic property of the stream.

Several studies have shown that stream geomorphology can have strong controls on hyporheic flow paths [*Harvey and Bencala*, 1993; *Kasahara and Wondzell*, 2003; *Morrice et al.*, 1997; *Wroblicky et al.*, 1998]. In streams underlain by permafrost, hyporheic flow is the movement of water from the channel into the active layer and back. For the purpose of this paper the thaw bulb is defined as the active layer area directly beneath streambed channels, whereas more common usage defines it as the thawed zone under or surrounding a man-made structure placed on or in permafrost [*Everdingen*, 2005]. Thus, hyporheic flow carries heat into the bed sediments and, as a result, controls the depth of thaw, setting up a feedback loop between stream geomorphology, hyporheic flow, and depth of thaw. To understand how streambed morphologies control thaw bulb expansion, which, in turn, affects hyporheic processes, it is important to understand the temporal evolution of the thaw bulb in streams with different morphologies.

Arcone et al. [1992; 1998a] successfully illustrated ground-penetrating radar (GPR) capabilities to profile groundwater and taliks, subsurface pockets that remain unfrozen year around, beneath frozen stream channels on the Sagavanirktok flood plain. Bradford et al. [2005] showed that it is possible to measure the depth of thaw under peat-bed streams across open water in August 2003 using GPR. These previous studies were limited in scope in that they provided either early season measurements within a frozen alluvial steam environment or one measurement in time within a peat-bed stream. The purpose of the current study is to provide a time series of the evolution of the thaw bulb under peat-bed and alluvial stream types over open waters during the summer season.

This purpose is also in direct support of ongoing studies by the authors investigating hyporheic dynamics in arctic streams [*Zarnetske et al.*, 2007].

2.3 Field Sites

The Kuparuk watershed is underlain by continuous permafrost with thickness ranging from 250 m near the foothills to over 600 m near the coast [*Osterkamp and Payne*, 1981]. Temperatures at 150 cm deep range between –9 °C to 3 °C, averaging –1 °C annually where the active layer thaws to depths of over 150 cm in the terrestrial soils during the summer seasons and begins to re-freeze in mid-September. Annual air temperatures range from –40 °C to 21 °C and averaged –8 °C for 2004 [*LTER*, 2004].

Study sites, located in the Kuparuk watershed (Figure 2.1) were selected to include stream reaches that spanned a range of geomorphologic conditions in rivers and streams on Alaska's North Slope. The streams were divided into two categories: 1) low-energy water flow with organic material lining the streambeds (peat streams) or 2) high-energy water flow with cobble to gravel material lining the streambeds (alluvial streams).

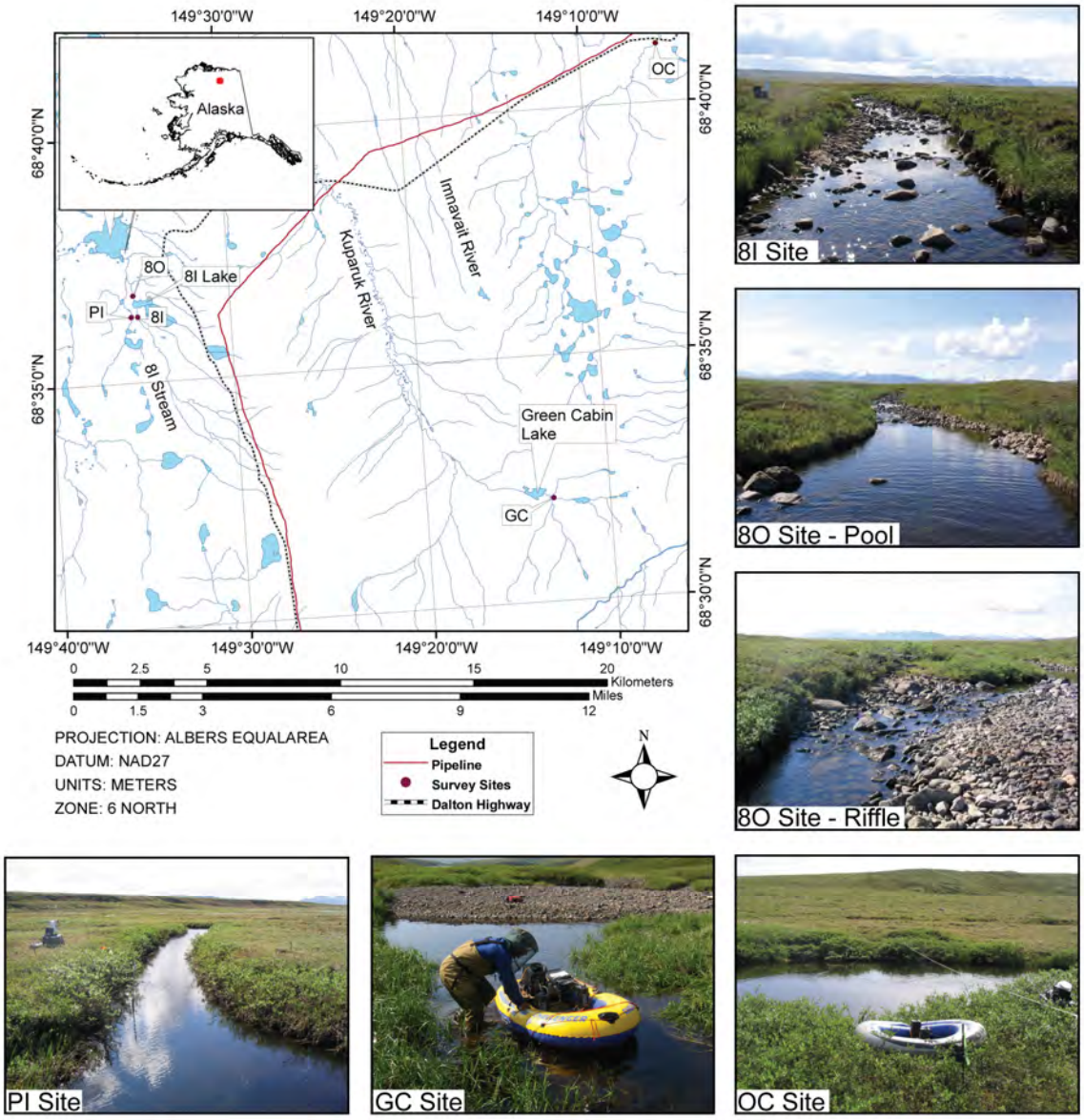

Figure 2.1. Locations of the five study sites within the Kuparuk watershed.

The Peat Inlet (PI) and Green Cabin (GC) sites represent the low-energy water flow environment and are described as beaded streams (deep pools connected by shallow, narrow channels). The GC stream reach is the stream right channel entering a confluence located upstream of Green Cabin Lake and is characterized by two large pools connected by a shallow channel. The upstream pool has a peat-lined stream bottom while the

second, downstream pool, is gravel-lined along the streambed. Radar profiles were collected across the middle of both pools and across the connecting channels upstream and downstream of each pool. To represent results at this site and avoid redundancy, only two of the five profile lines will be discussed (Table 2.1).

Table 2.1. Site Names with Stream Morphology and GPR Profile Descriptions.

	Site Name	Geomorphology/GPS Coord.	GPR Profile Description
High-energy	8I Inlet (8I)	Gravel to cobble-lined stream with riffle-pool-riffle morphology. 0.97% gradient 06 W 0394707, 7612535	Run 6 m across and 0.2 m deep. Subsurface temperature sensors installed near profile lines.
	8I Outlet (8O)	Gravel to cobble-lined stream with riffle-pool-riffle morphology. 1.18% gradient Pool – 06 W 0394582, 7613443 Riffle – 06W 0394593, 7613456	Pool – 7 m across and 0.6 m deep. Riffle – 7 m across and 0.2 m deep.
Low-energy	Green Cabin (GC)	Organic-lined with beaded morphology. Channel walls are described with a gradual gradient where the connectors are very shallow with fast moving water. Pool section streambed bottom is lined with cobble material. Connector – 06W 0409402, 7603959 Pool – 06W 0409390, 7603956	Connector – 4 m across and 0.2 m deep. Pool – 8 m across and 1 m deep.
	Peat Inlet (PI)	Organic-lined stream with beaded morphology. Deeply incised pools and connectors with near-vertical channel walls. 0.90% gradient 06 W 0394444, 7612794	Connector – 2 m across and 1 m deep. Subsurface temperature sensors installed near profile line.
High/low-energy	Okruknyik Creek (OC)	Organic-lined stream with beaded morphology. Streambed bottom lined with gravel/cobble material indicating high-energy events. 0.16% gradient 06 W 0414902, 7620835	Pool – 12 m across and 2 m deep.

The PI stream reach flows into Toolik Lake and is characterized by large, deep pools (12 m wide, 2.5 m deep) connected by relatively deep channels. Radar profiles were collected across one of the deeply incised connecting channels in the same location where Bradford et al. [2005] collected radar profiles in August 2004 (Table 2.1).

I-8 stream is in close proximity to the PI site and also flows into Toolik Lake. It, however, represents the high-energy flow environment. The I-8 Inlet site represents a run section of the stream and (8I) is located upstream of I-8 lake. The next site, I-8 Outlet (8O), is located downstream of I-8 Lake, where radar profile were acquired across a pool and riffle section of the stream (Table 2.1).

Oksrukuyik Creek (OC), located just upstream of the Dalton Highway crossing, is a hybrid of the two previous categories. The stream reach is described as beaded and is characterized by a series of incised large pools connected by relatively fast moving, shallow channels; however, the streambed bottom along the entire reach is lined with gravel-to-cobble sized rocks rather than organic matter which indicates intermittent high-energy flow events. Radar profiles were gathered across one of the pools and across the upstream and downstream connectors of the same pool. Results from this site will focus on the images collected over the pool (Table 2.1).

2.4 Methods

GPR data were collected at the five sites from May - September 2004. Profiles were gathered on a weekly to monthly basis to measure changes in the thaw bulb thickness over the summer season and evaluate the effectiveness of GPR within the varying environments. In addition, we recorded channel and thaw bulb temperatures using thermocouples placed at varying substream depths within two of the five GPR data collection sites (PI and 8I) to help constrain and verify GPR interpretation.

2.4.1 Ground-Penetrating Radar (GPR)

GPR is a non-invasive method used to explore the shallow subsurface with electromagnetic waves. The transmitting antenna creates a pulsed electric field which propagates into the subsurface and is reflected where abrupt changes in electrical properties occur across interfaces. The receiving antenna records a trace of the reflected wave field in time. Multiple measurements are made along the surface, producing a cross-sectional reflection profile image of electric impedance contrasts in the subsurface [*Davis and Annan*, 1989].

There is a large electrical contrast between water and ice. Using the time dependence equation given by Olhoeft [1981] the dielectric constant for water, at 0 ºC, is 87-88 and 3.2 for ice [*Davis and Annan*, 1989]. Consequently, as water freezes within the subsurface, the dielectric permittivity (a measure of molecular polarizability of the wet sediments) decreases while the velocity of propagation increases [*Scott et al.*, 1990]. Because GPR reflections primarily result from contrasts in electric permittivity, GPR is an ideal tool for mapping the saturated soils/permafrost boundary. Numerous studies have shown that GPR has been used successfully to detect spatial and temporal variations in the permafrost boundaries within terrestrial soils [*Arcone et al.*, 1998b; *Doolittle et al.*, 1990; *Doolittle et al.*, 1992; *Hinkel et al.*, 2001; *Pilon et al.*, 1985; *Wong et al.*, 1977].

Problems that arise while collecting substream radar images include attenuation of signal due to the strong frequency dependence of radar wave velocity and image distortion due to velocity contrasts. High frequencies travel faster and attenuate more quickly in water, which causes the dominant frequency to shift towards the lower end of

the spectrum, resulting in lower resolution potential. For the data presented here, frequency decreases due to loading and frequency-dependent attenuation are significant and measurable such that attenuation through water lowers the frequency in 200 and 100 MHz data to ~120 and ~70 MHz, respectively [*Bradford et al.*, 2005]. Stream water discharge and temperature variations can increase the dissolved solid concentration levels in the water, which causes higher conductivities and results in greater attenuation rates and even lower resolution potential [*Bradford et al.*, 2005]. Water conductivity values at the study sites were very low (~40 μS/cm), with no apparent seasonal variation, therefore their effects on the data are negligible. Additionally, image distortion occurs where reflections are pushed down due to large velocity contrasts between water and saturated soils. Depth migration with the right velocities corrects for the distortion by placing the reflectors in their proper spatial location. Despite these limitations, several studies have successfully demonstrated high-resolution water bottom images over cold-region freshwater bodies [*Arcone et al.*, 1992; *Arcone et al.*, 1998a; *Best et al.*, 2005; *Delaney et al.*, 1990; *Schwamborn et al.*, 2002].

GPR resolution is limited by wavelength which is related to velocity, v, and frequency, f, through the relation $\lambda = v/f$. This relationship shows that higher frequencies result in smaller wavelengths which are capable of resolving finer features; however, higher frequencies also attenuate more quickly, therefore decreasing the depth of investigation; thus a tradeoff exists between depth of investigation and resolution potential. For this study, the wavelength relationship to velocity works in our favor

because the velocity within the water-saturated thaw bulb region is lower than in the permafrost region, leading to greater resolution potential within the area of interest.

Data were acquired using a Sensors and Software pulsed radar system with a high-power transmitter (1000V) used for all antenna frequencies. Early in the field season we used the 400 and 200 MHz antennas to maximize resolution potential, and then shifted to the 200 and 100 MHz antennas later in the summer season to increase the depth of penetration. We placed the radar antennas in the bottom of a small rubber boat, then pulled the boat across the bank and through the stream while collecting radar traces at a constant distance interval via a string odometer system. Stakes were placed at the start and end points where the profile lines were collected so that the GPR lines were collected at the same locations throughout the season. Despite the location control, differences are apparent in some of the stream profiles due to variations in stream water discharge.

In addition, depth to the thaw front (freeze/thaw interface) was measured on the stream banks and shallow streambed areas by pressing a metal probe into the ground to the point of refusal. At 8I and PI, subsurface temperature profiles were used to constrain GPR interpretations with the assumption that the depth at which the temperature is 0 ºC is the boundary between the active layer and the permafrost.

We applied the following processing flow to each dataset:

1. Time zero correction with first break correlation to remove start of record delay and system drift.

2. DC shift and bandpass filtering with a 25-50-400-800 (for the 200 MHz) and a 12-25-200-400 (for the 100 MHz) Ormsby filter to attenuate the low frequency transient and high frequency random noise.
3. Amplitude correction which varied by site.
4. Kirchhoff depth migration coupled with iterative velocity model refinement [*Yilmaz,* 2001].

Because we were interested in thaw bulb depths, our velocity models only included values for water and the water saturated substrate material. A velocity value of 0.032 m ns^{-1} was used for water at 0 ^{o}C, and a velocity value of 0.05 m ns^{-1} was used for saturated peat material based on results reported by Bradford et al. [2005] and was also within range of values reported in other studies [*Davis and Annan,* 1989; *Moorman et al.,* 2003]. From the migration velocity analysis (using a velocity value of 0.07 m ns^{-1} for the saturated gravel/sand material) we collapsed the diffractions and minimized migration artifacts.

High amplitude water bottom and permafrost multiples, and diffraction patterns caused by out-of-plane point sources within the gravel-lined stream site profiles presented interpretation challenges. Time lapse images helped identify the thaw front despite the presence of multiples or diffraction patterns. Additionally, due to radar resolution limitations, temperature data profiles significantly improved our ability to interpret the permafrost boundary in early season radar images.

2.4.2 Temperature Measurement

Temperature was measured using Type-T thermocouple wire connected to a Campbell Scientific CR10X datalogger and AM16/32 multiplexer using a CR107 reference thermistor. Errors associated with Type-T thermocouples are ±1.0 °C over the range of -65 to 130 °C. Thermocouples were installed in vertical profiles by driving a steel sleeve and interior bar into the streambed. The bar was then removed and the thermocouples were inserted into the sleeve. Lastly, the sleeve was removed from the sediment and pulled over the thermocouple wire, leaving the thermocouples in place. We installed 4 streambed profiles and 1 soil profile in 8I and 2 streambed profiles in PI at 20 cm increments to varying depths. Temperature profiles at site 8I reached a depth of 107 cm, while those at site PI reached a depth of 38 cm. The shallow depths at PI are due to frozen soil and deep water at the time of installation. Continuous subsurface temperature readings were recorded from late May throughout the remaining year.

2.5 Results

2.5.1 Low-Energy

At the GC site (connector), the late May reflections (200 MHz) of the thaw front were difficult to discern from the water bottom reflections due to resolution limitations where $\lambda/4$ provides an approximate vertical resolution limit [*Yilmaz,* 2001]. Assuming a dominate frequency of 200 MHz with loading at ~120 MHz and a velocity in water-saturated peat of 0.05 m ns^{-1}, the signal wavelength is 0.416 m and the vertical resolution limits are roughly 10 cm, meaning that objects separated by less than this distance cannot

be individually identified. For the 100 MHz antennas with loading at ~70 MHz and a velocity of 0.07 m ns^{-1} in water-saturated gravel the vertical resolution is 25 cm. Within a month the boundary became discernible (Figure 2.2a-b). As the thaw depth increased we recorded a separate and easily recognizable strong, continuous reflection from the thaw front where the maximum thaw bulb thickness, 51 cm, was recorded on September 21 (Figure 2.2c-d). The later season profiles show relatively weak reflections at the water-to-peat bottom boundary due to relatively small contrasts in the permittivity between the two media. Also notable are the pulldown in the reflectors under the channel due to the lateral velocity change from the water-filled channel to water-saturated soil (Figure 2.2a and c) and correct positioning of the reflector pullup after depth migration was applied (Figure 2.2b and d).

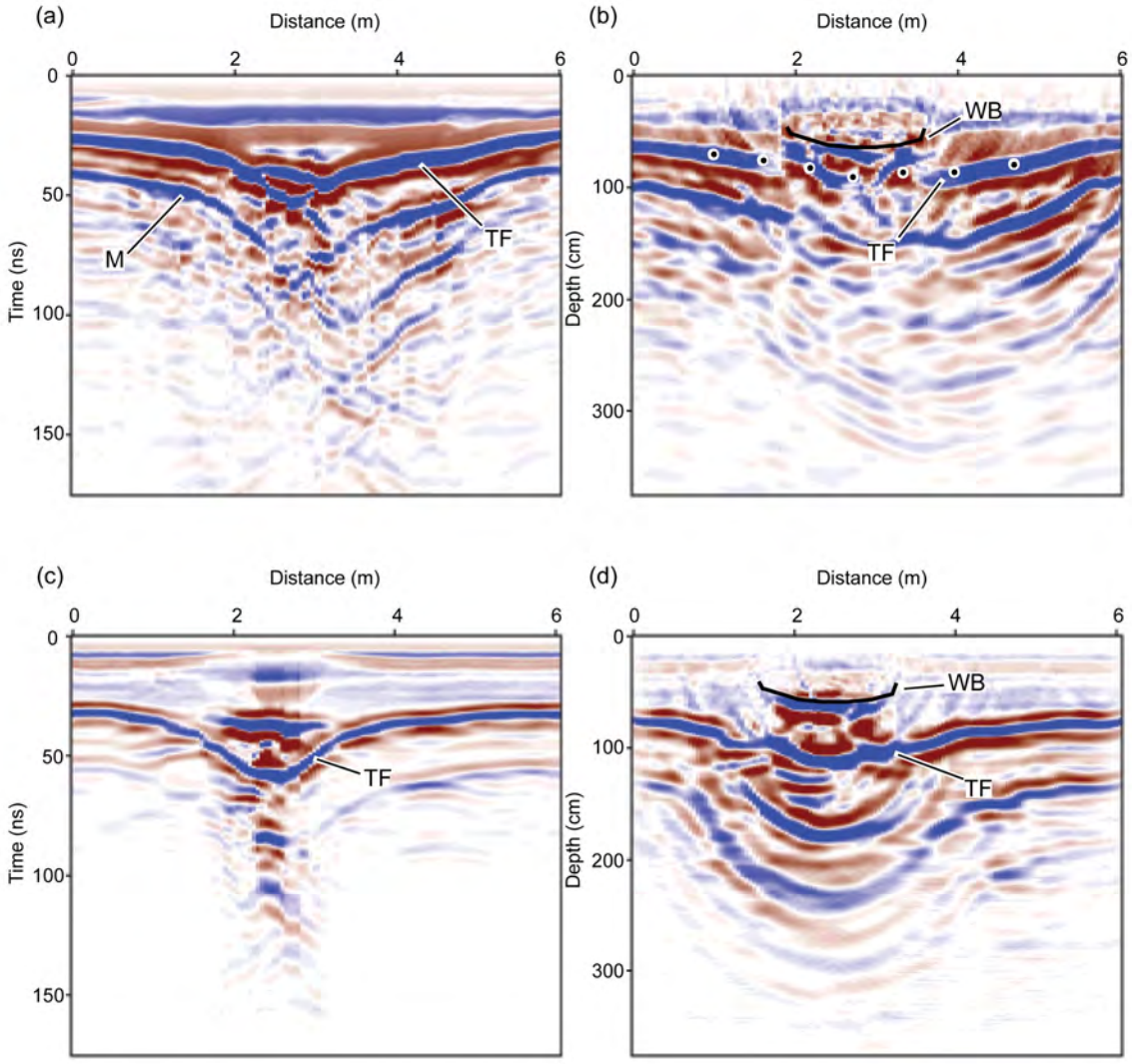

Figure 2.2. (a) Preprocessed image from GC-connector recorded on June 28, 2004 (200 MHz), (b) depth migrated image, (c) preprocessed image recorded September 21, 2004 (200 MHz), (d) depth migrated image. (—) interpreted water bottom, (●) thaw front, (TF) thaw front reflection, (WB) water bottom, (M) multiple.

Resolution was not problematic in early season, 200 MHz profiles from the pool site (GC-pool) due to initially deeper thaw depths where the thaw bulb was easily resolved (Figure 2.3a-b). The maximum thaw bulb thickness, 104 cm, was recorded on September 21 (Figure 2.3c-d). Relative reflection strength was higher in pool profiles

in comparison to connector profiles. This difference in amplitude indicates greater permittivity contrast caused by the gravel-lined pool bottom.

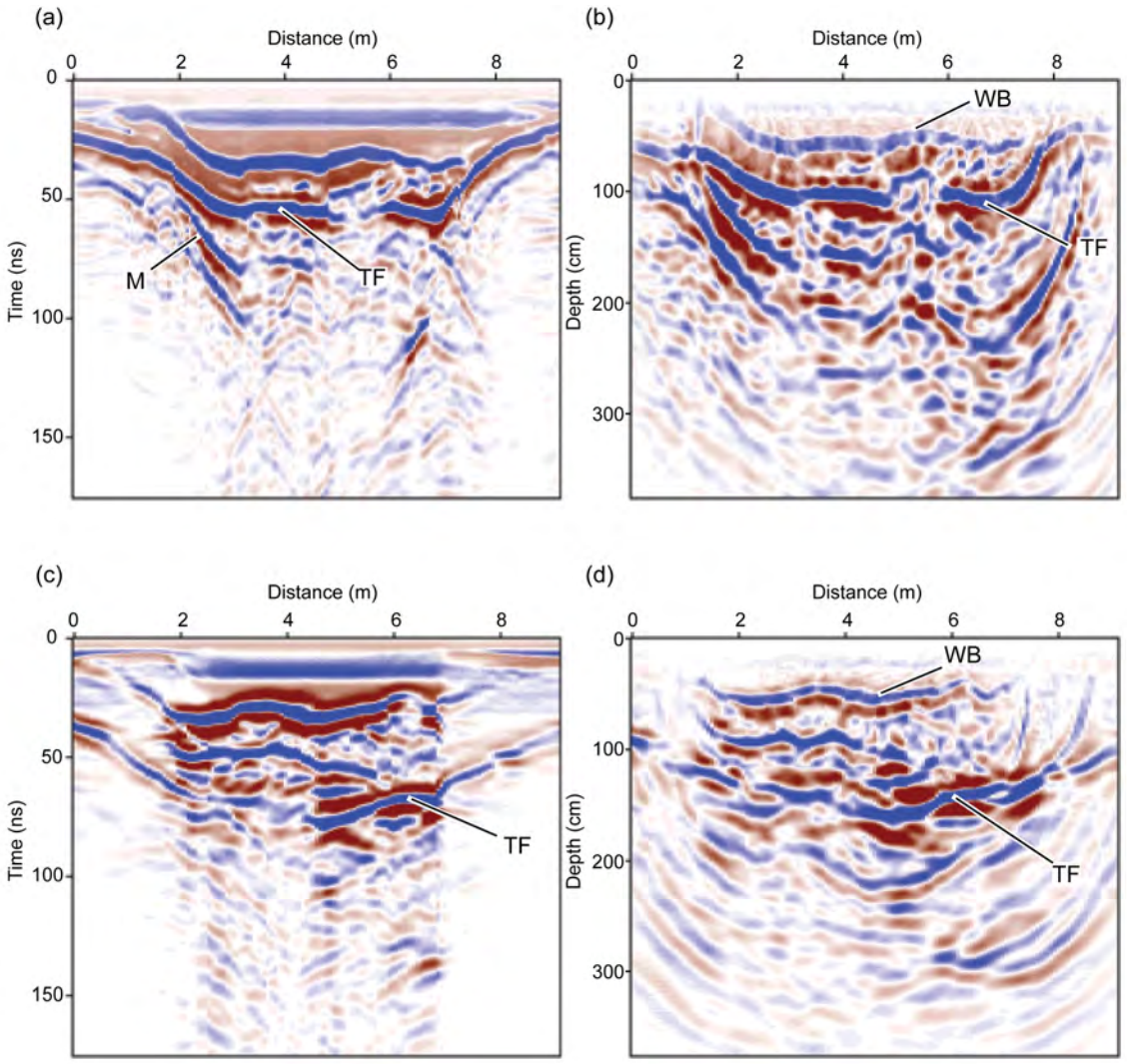

Figure 2.3. (a) Preprocessed image from GC-pool recorded on June 28, 2004 (200 MHz), (b) depth migrated image, (c) preprocessed image recorded September 21, 2004 (200 MHz), (d) depth migrated image. (TF) thaw front reflection, (WB) water bottom. (M) multiple.

Results at the PI site were very similar to those noted within the GC-connector profiles. The thaw front proved easy to identify from a strong continuous reflection

throughout the season (Figure 2.4). Despite the physical differences, the PI site being deeply incised with greater water depths, the thaw depth seasonal patterns at PI and GC-connector are remarkably similar.

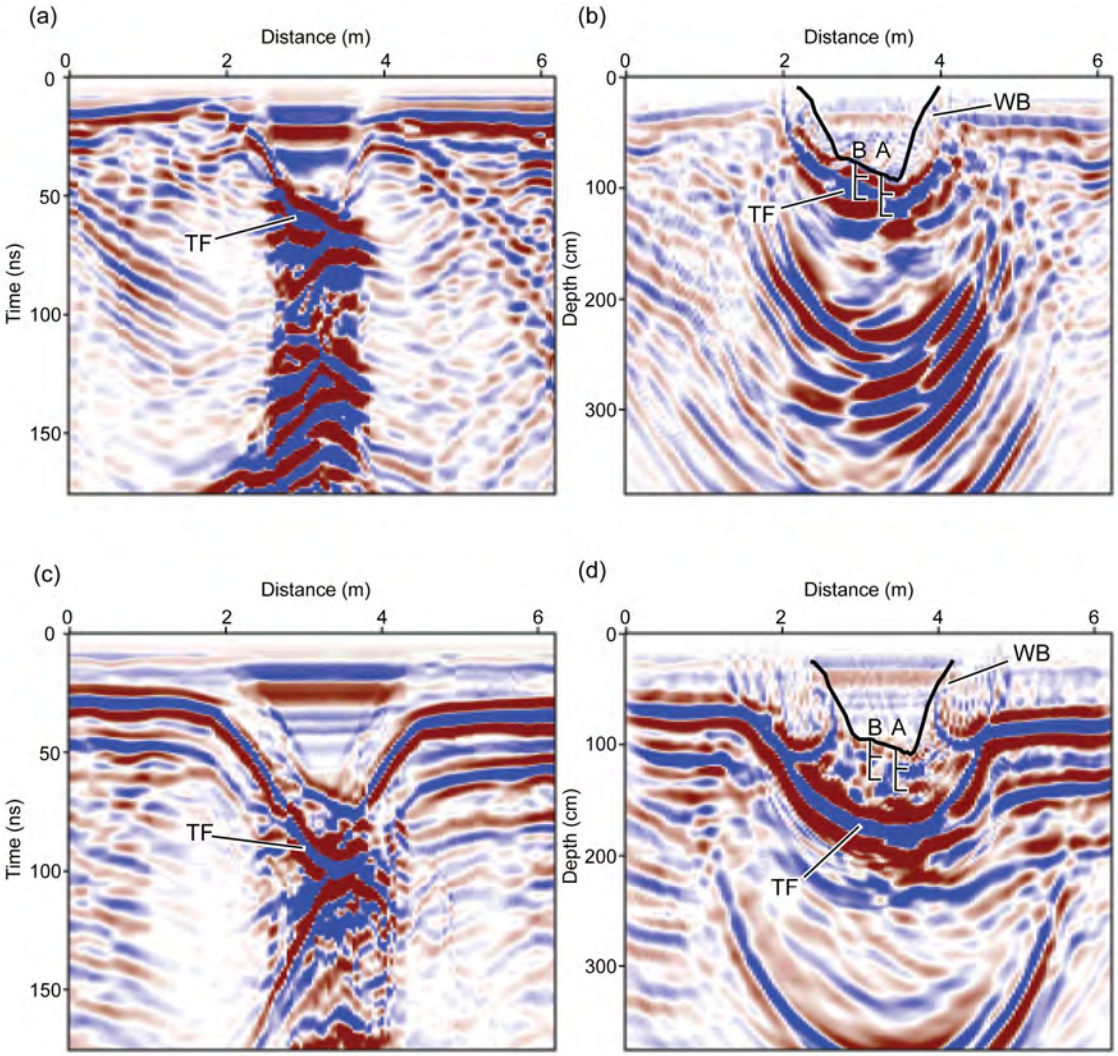

Figure 2.4. (a) Preprocessed image from PI site recorded on June 7, 2004 (200 Mhz), (b) depth migrated image, (c) preprocessed image recorded on August 6, 2004 (200 MHz), (d) depth migrated image. (—) interpreted water bottom, (TF) thaw front reflection, (WB) water bottom, temperature sensor locations represented at B (16 and 36 cm) and A (18 and 38 cm).

Subsurface temperature values recorded by the thermocouples helped us to interpret the thaw front in the early season profiles and confirmed interpretations in the later season images. We began logging temperature profiles on May 31. Prior to our initial logging, profile A had just thawed to 18 cm, but profile B did not thaw to 16 cm until 9 days later (June 12). Likewise, profile A thawed to 38 cm on June 27 while Profile B remained frozen at 36 cm until July 11. Warmer temperature values recorded at profile A correlate with the radar profiles where a deeper reflection is noted on the right side of the streambed (Figure 2.4b), indicating greater thaw depths beneath the thalweg of the stream. Maximum thaw beneath the thalweg may be caused by more heat going into the system from the warmer instream water temperatures. As the season advances and the temperatures increase, thalweg effects became less prevalent and the maximum thaw depth becomes more evenly distributed across the center of the streambed (Figure 2.4d). The August profile from PI (Figure 2.4a-b) also correlates with the radar image collected by Bradford et al. [2005] where the maximum thaw depth was estimated at 61 cm in August 2003 and 63 cm in August 2004.

The alluvial-peat Oksrukuyik Creek (OC), despite having a peat-influenced morphology, experienced the greatest overall thaw depths compared to the other peat-lined stream sites. We collected early season radar images with 200 MHz antennas and then shifted to 100 MHz antennas in the later season to increase the depth of investigation. In the early season profile, within the unmigrated image, there is a continuous thaw front reflection obscured by high-amplitude water bottom diffractions (Figure 2.5a). After migration, the diffractions are collapsed and the water bottom and

frost table reflectors were moved to their correct spatial locations, resulting in a distinct reflection at the thaw front (Figure 2.5b). The August radar image, collected with 100 MHz antennas, captured a distinct reflection of the thaw front at a depth of 233 cm (Figure 2.5c). The boundary then becomes partly obscured from multiple scattering and water bottom multiples as the boundary depths decrease towards the sides of the channel (Figure 2.5c). The thaw front in the migrated image of the same profile is difficult to distinguish due to over-migration of multiples (Figure 2.5d). Migration algorithms only account for primary traveltimes therefore multiples are not treated correctly and always appear over-migrated.

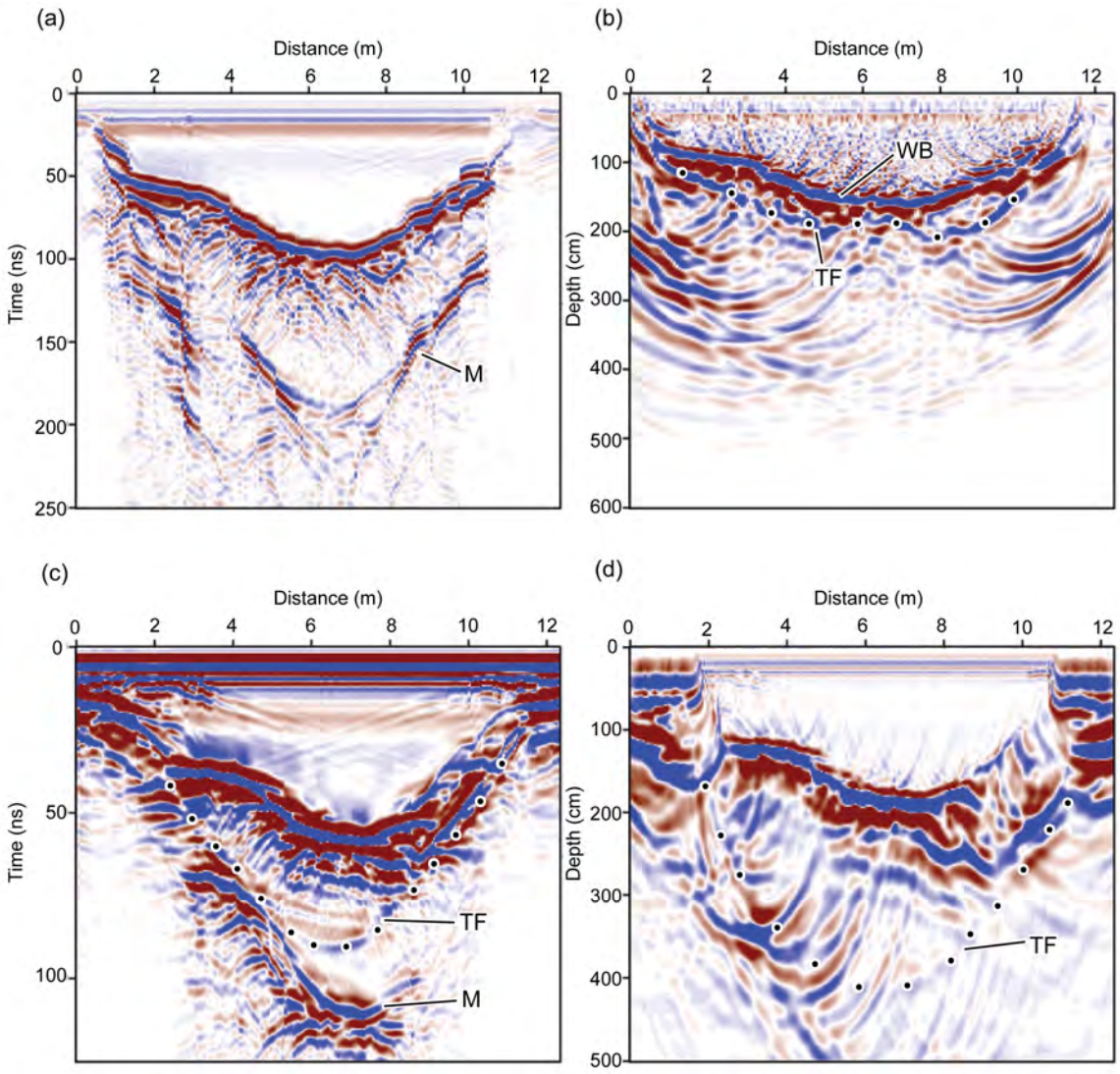

Figure 2.5. (a) Preprocessed image from OC recorded on June 2, 2004 (200 MHz), (b) depth migrated image, (c) preprocessed image recorded August 5, 2004 (100 MHz), (d) depth migrated image. (●) thaw front, (TF) thaw front reflection, (WB) water bottom, (M) multiple.

2.5.2 High-Energy

Imaging the thaw bulb within the gravel-lined stream sites proved to be more difficult due to a highly heterogeneous environment. Variable sand-to-gravel-to-cobble-to-boulder sized material under the streambeds caused, in some cases, severe multiple

scattering patterns within the radar images. These diffraction patterns effectively masked the location of the frost table beneath the streambed channels. Despite these limitations we were able to interpret the thaw front from a number of images.

Radar images collected at the 8I site were among the most difficult to interpret; however, subsurface temperature data collected at this site confirmed early season depth-to-thaw boundaries. Some of the later season profiles resolved the thaw front relatively well, whereas after migration the same images became difficult to interpret. This was due to 2D limitations where 3D point source diffractions cannot be collapsed by 2D migration to their correct spatial location because they occur off the 2D GPR line.

Stream temperature logging began at 8I following the snowmelt period on May 31, 2004. Three thermocouple profiles in the streambed show that subsurface thaw had started prior to May 31. In profile A the streambed was thawed past 47 cm, but remained frozen at greater depths. The streambed thawed to 67 cm, 87 cm, and 107 cm on June 2, June 5, and June 7, respectively. In profiles B and C the streambed was thawed past 80 and 82 cm, respectively, prior to our arrival in late May, but appears to have just thawed to 100 cm and 102 cm on June 2. Thaw occurs in the adjacent soil later than in the streambed. The soil was slightly above 0 °C at 8 cm deep when we began logging, but did not thaw until June 14 and June 19 at 28 cm and 48 cm, respectively.

Following thaw, all four streambed temperature profiles behaved similarly with peak temperatures occurring in early July. Streambed temperatures rose and fell, mimicking air temperature with slight lags at depth. Throughout the season subsurface temperature values decreased with depth until late-August when temperatures at greater

depths became warmer than temperatures at shallower depths. All profiles and all depths reached 0 ºC by late-September.

Images collected at the pool and riffle sections at the 8O site were more easily interpreted than the 8I profiles, probably because the subsurface was more homogeneous. Radar profiles over the pool illustrate an excellent continuous reflection from the thaw front throughout the season. Radar images over the riffle showed a clear reflection from the thaw front in both the migrated and unmigrated images (Figure 2.6). Profiles over the riffle resolved a much deeper thaw front under the exposed gravel bar, left side, and a thinner thawed region under the active stream section (3 – 6 m). Overall interpreted maximum thaw depths were greater at the 8O-riffle site than at the 8I site.

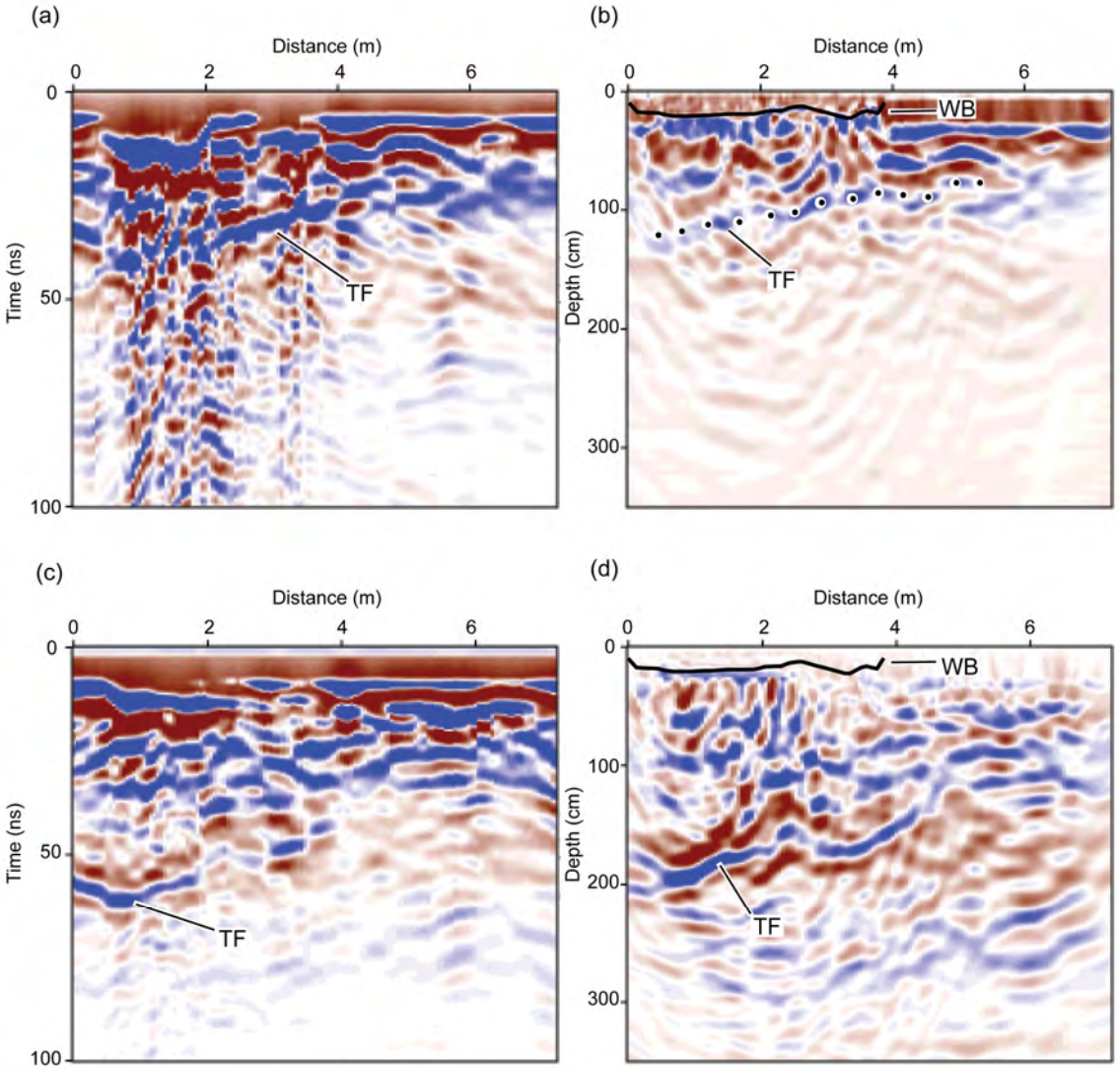

Figure 2.6. (a) Preprocessed image from 8O-riffle recorded on June 7, 2004 (200 MHz), (b) depth migrated image, (c) preprocessed image recorded June 22, 2004 (200 MHz), (d) depth migrated image. (—) interpreted water bottom, (●) thaw front, (TF) thaw front reflection, (WB) water bottom.

2.6 Discussion and Conclusions

Our results demonstrate that GPR methods are useful in monitoring subsurface seasonal thaw within both peat and alluvial stream environments. In some of the early season profiles the thaw front within the peat-lined streams was difficult to identify, due

to resolution limitations. Later season images were successful due to a typically homogeneous subsurface, small contrast between peat and water, and smooth channel bottoms. Successful images within gravel-lined streams were strongly site dependent and interpretations were significantly more complicated due to diffraction patterns caused by a highly heterogeneous subsurface and the irregular water/streambed interface. Identification of the thaw front reflection within the gravel-lined streams was greatly improved by gathering time-lapse profiles over the summer season where the moving boundary was properly identified. The same reflection in a one time seasonal image may be misinterpreted as a multiple.

Thaw bulb development within the two stream environments was distinctly different. Figure 2.7 illustrates interpretations of the thaw front depths for each site, from GPR and temperature data, throughout the field season period. Thaw depths increased to depths greater than 1 m within the first four weeks of the season within gravel-lined streams and to only 32 cm within peat-lined streams (Figure 2.7 and Figure 2.8). Based on multiple images gathered over the season, maximum thaw depths within the gravel-lined streams, which may represent the permafrost table, were recorded in August. In September the gravel-lined sites began to refreeze while the peat-lined sites continued to thaw. Maximum thaw depths in the latter were recorded up to the last site visit in September, indicating a heat lag in the peat-lined streams (Figure 2.8).

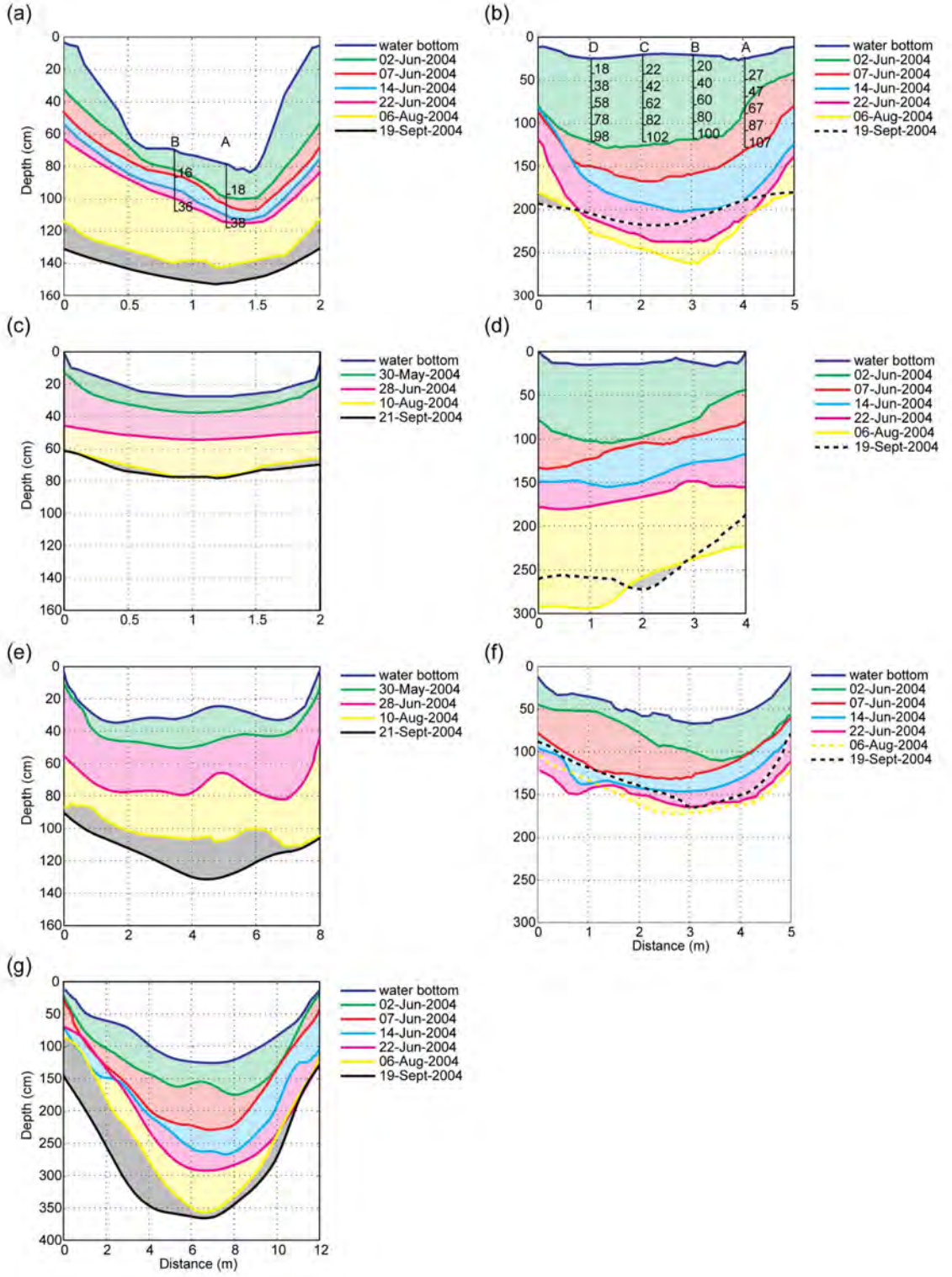

Figure 2.7. Frost/thaw boundary depths interpreted from GPR images and temperature data when available. (- - -) frost/thaw boundary interpreted at a shallower depth than earlier GPR profiles. (a) PI with temperature sensor locations (cm) measured from the

stream channel bottom, (b) 8I with temperature sensor locations (cm) measured from the stream channel bottom, (c) GC-pool, (d) 8O-pool, (e) GC-connector, (f) 8O-riffle, (g) OC.

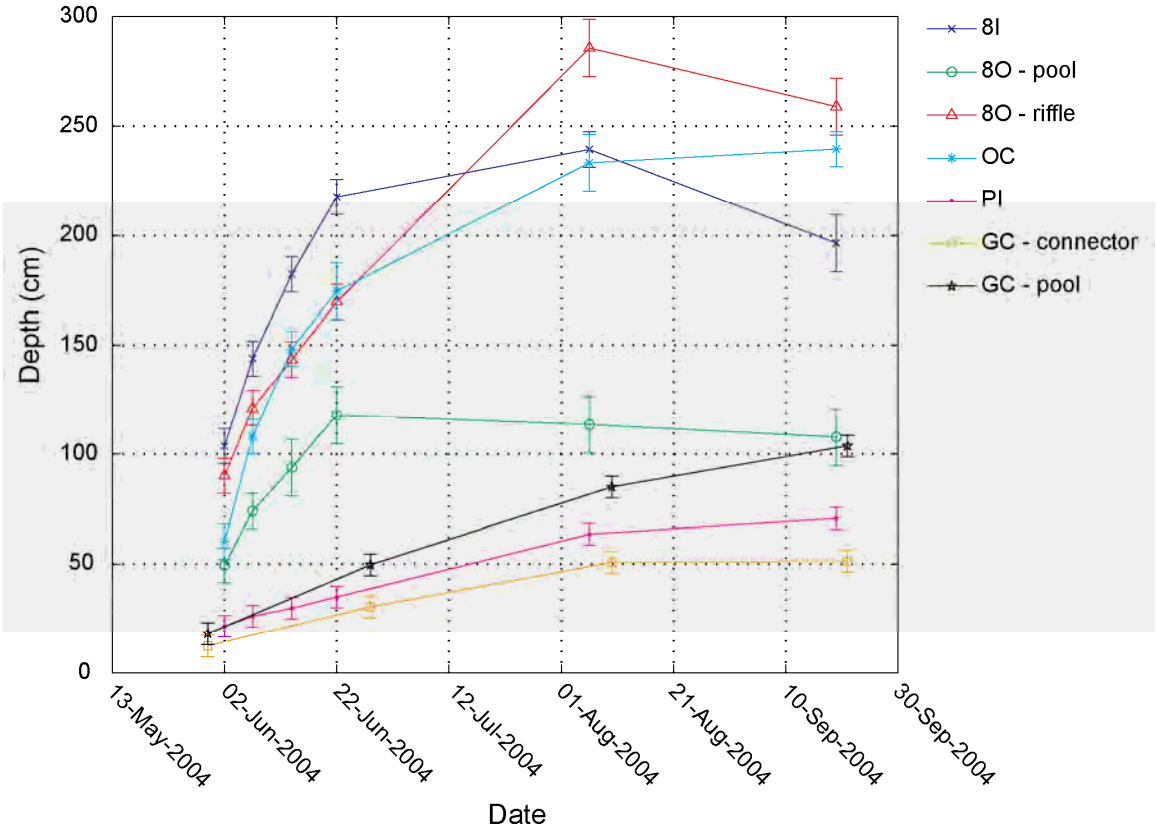

Figure 2.8. Maximum thaw-bulb depths for the five sites. For the 200 MHz data a ± 5 cm error is calculated for the peat-lined stream sites. At the gravel-lined stream site a ±8 cm error is estimated for interpretations made from the 200 MHz and a ±13 cm error is estimated for the 100 MHz data.

Temperature profiles recorded at 8I coincide with the interpreted GPR profiles where the thaw bulb grew rapidly in the early season. Thermocouples did not reach to the depth of the interpreted permafrost table recorded in August; however, the temperature gradient which inverted late August (cooler temperatures at shallow depths)

indicates a change in the thermal input into the system (Figure 2.9). The September GPR interpretation illustrates thaw bulb retreat from colder temperatures (Figure 2.7).

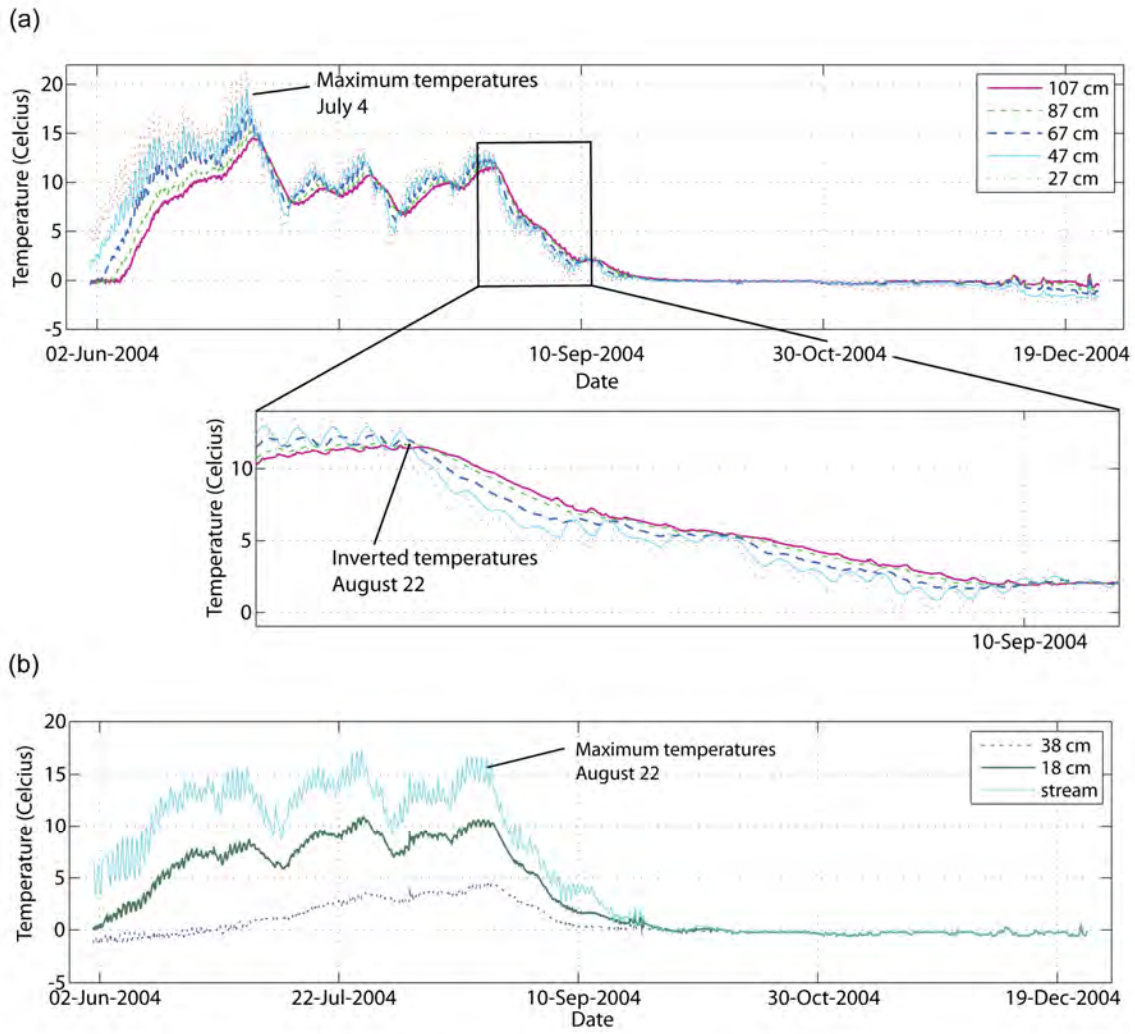

Figure 2.9. Temperature data from (a) string A at 8I site and (b) string A at PI site.

Early season thaw depths between 8I and 8O-riffle were both similar in trend with much greater thaw depths interpreted at the 8O-riffle in the later season. Variation in the thaw bulb thicknesses between 8I and 8O-riffle is likely due to heat transfer from a greater surface area of exposed rocks (left side) within the riffle section at 8O. Overall

thaw depths within the 8O-pool section were much smaller and are likely due to minimal rock exposure compared with the 8I and 8O-riffle sections.

Comparisons between temperature values recorded at PI and 8I illustrate distinct differences in thermal input between the two systems. Maximum temperatures are reached by July 4 and August 22 at 8I and PI, respectively. At the PI site temperature gradients are much larger and shallow temperatures (16 and 18 cm) are always warmer than the deeper (36 and 38 cm) temperatures over the field season period. At 8I temperature gradients are much smaller, over a greater depth range, and a temperature inversion occurs at the same time maximum temperatures are recorded at 38 cm beneath the PI site (Figure 2.8). Differences between sites could be due to the deeper water at PI, combined with the peat lining that covers the streambed.

The pool profile at OC responded similarly to the pool section at GC in that thaw depths at both sites continued to increase up to the last site visit in September. However, the OC site recorded much greater thaw depths with a maximum thaw depth of 240 cm on September 20 (Figure 2.8). One possible cause for the continued thaw at OC may be the result of more substantial and persistent flows experienced by OC which, in turn, promoted sub-channel thaw through September.

Comparisons between the two stream types illustrate distinct differences in the seasonal thaw bulb development. Gravel-lined streams respond much more quickly to thermal input and peat-lined sites display a much slower response in early season and either maintained or expanded their thawed regions through the late season (Figure 2.8). These observations indicate rapid heat absorption and heat loss in the gravel-lined

streams whereas the peat-lined streams illustrate an insulating effect that extends past the maximum solar input time frame.

3 MULTI-OFFSET GPR METHODS FOR HYPORHEIC ZONE INVESTIGATIONS

3.1 Abstract

Porosity of stream sediments has a direct effect on hyporheic exchange patterns and rates. Improved estimates of porosity heterogeneity will yield enhanced simulation of hyporheic exchange processes. Ground-penetrating radar (GPR) velocity measurements are strongly controlled by water content thus accurate measures of GPR velocity in saturated sediments provides estimates of porosity beneath stream channels using petrophysical relationships. Imaging the substream system using surface based reflection measurements is particularly challenging due to large velocity gradients that occur at the transition from open water to saturated sediments. The continuous multi-offset (CMO) method improves the quality of subsurface images through stacking and provides measurements of vertical and lateral velocity distributions. We applied the CMO method to stream sites on the North Slope, AK, and the Sawtooth Mountains near Boise, ID, USA. From the CMO data, we measure velocity using reflection tomography then estimate water content and porosity using the Topp equation. These values provide detailed measurements for improved stream channel hydraulic and thermal modeling.

3.2 Introduction

The movement of stream water flowing into the near sub-surface and back out to the stream channel is known as hyporheic exchange flow (Figure 3.1). The spatial extent of this exchange defines the hyporheic zone. Hyporheic exchange processes have a significant effect on biogeochemical cycling within stream ecosystems [*Gooseff et al.*, 2002; *Jones et al.*, 1995; *Mulholland et al.*, 1997]. These processes have been studied in temperate stream systems [*Arntzen et al.*, 2006; *Harvey and Bencala*, 1993; *Hill et al.*, 1998; *Kasahara and Wondzell*, 2003; *Vervier et al.*, 1993; *Wondzell and Swanson*, 1999; *Wroblicky et al.*, 1998] and, to a lesser extent, in arctic stream environments [*Edwardson et al.*, 2003; *Greenwald et al.*, 2008; *Zarnetske et al.*, 2007; *Zarnetske et al.*, 2008].

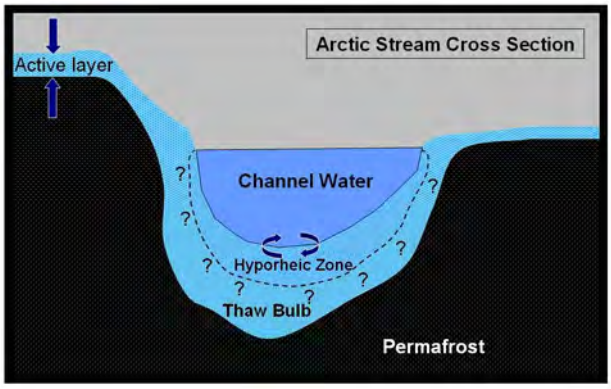

Figure 3.1. The extent of the hyporheic zone is defined as the area where channel water and subsurface water mix. In arctic streams the hyporheic zone exists within the seasonal thaw layer, defined as the thaw bulb beneath the streams [*Greenwald et al.*, 2008].

Rates of hyporheic exchange flow in a stream reach are governed by spatial distributions of hydraulic head and hydraulic conductivity, which are typically measured at point, rather than reach, scales. The spatial distribution of hydraulic conductivity can be particularly important to understand given the high heterogeneity of sediments in

gravel-bed rivers [*Cardenas and Willson*, 2004]. However, obtaining distributed measurements of hydraulic conductivity by conventional piezometer methods in a streambed is impractical and invasive. Non-invasive, surface-based methods to obtain distributed measurements of hydraulic conductivity would add value to studies of hyporheic exchange.

For the ground-penetrating radar (GPR) frequency band of 10-1000 Mhz, the frequency dependence of the conductivity and dielectric permittivity are small for many earth materials and are often assumed to be constant. With this assumption, electromagnetic (EM) wave velocity, *v*, is related to dielectric permittivity, *K*, by $v = \frac{c}{\sqrt{K}}$, where *c* is the speed of light in a vacuum and $K = \varepsilon / \varepsilon_0$ (ε_0 is the dielectric permittivity of a vacuum $8.85 \times 10^{-12} F/m$ and ε is the dielectric permittivity of the material). The magnetic permeability, μ, is assumed to be equal to μ_0, the free space permeability ($4\pi \times 10^{-7} H/m$).

Given the previous assumptions, the dielectric permittivity dominates EM velocity variations where water is a highly polarizable naturally occurring material (with a permittivity of $K \approx 81$ in contrast to typical soil grain material permittivity values of 4-6). Because water is always present, in the pore space of hyporheic sediments, it has a dominant effect on electrical properties. The relationship between permittivity and water content has been used in a number of previous studies to transform velocity to moisture content [*Bradford*, 2008; *Greaves et al.*, 1996; *Hanafy and Hagrey*, 2006; *Huisman et al.*,

2003; *Lunt et al.*, 2005; *Topp et al.*, 1980]. In fully saturated soils, water content is equivalent to porosity.

Because the sediments are fully saturated in the hyporheic zone, GPR velocity measurements are strongly tied to hyporheic zone porosity. In temperate and arctic stream environments unfrozen water content, which is related to porosity, is an important parameter that directly affects the depth and rate of freezing and thawing [*Hinzman et al.*, 1991; *Romanovsky and Osterkamp*, 2000]. The link between GPR measurements and hydraulic conductivity is more tenuous and is an area of active research. We do not attempt to derive hydraulic conductivity from GPR measurements in this study, however, it is important to recognize that previous studies have established empirical relationships where hydraulic conductivity is derived from dynamic viscosity, effective grain size, and porosity for sand and gravel systems [*Bear*, 1972; *Carman*, 1937; *Fitts*, 2002]. These relationships break down when clay is introduced to the system. Soils within the study sites presented in this study are composed of low-loss materials where GPR propagates effectively implying the presence of little to no clay.

Topp et al. [1980] presented an empirical relationship of water content as a function of dielectric permittivity based on four soil types (sandy loam to clay dominated). To test the validity of their relationship they expanded the study to include an organic soil, ground vermiculite mineral, and two sizes of glass beads. Through the petrophysical relationship presented by Topp et al. [1980] GPR can provide laterally and vertically continuous porosity measurements beneath stream channels. These porosity measurements in turn provide constraints on hyporheic zone hydraulic conductivity and

perhaps more effectively provide a measure of lateral variability in the hydraulic conductivity. These constraints have the potential to significantly improve the understanding of hyporheic flow and thermal dynamics.

Conventional GPR surveys are acquired with a constant transmitter-receiver offset. EM velocities for the GPR images are estimated by one of three methods; 1) radar reflectors are directly correlated with significant boundaries identified in the borehole data. Drawbacks include misinterpretation, lack of lateral resolution, and the expense of deploying a destructive method. 2) Moveout of scattering diffractions within the data image can be used to estimate velocities. However, diffractions are not always present and when they are their distribution determines the limits of the lateral and vertical velocity estimates. 3) Lastly, sparsely located common-midpoint (CMP) soundings are gathered (perhaps at one or two points) along the survey line and then normal moveout (NMO) analysis is used to estimate root-mean square (rms) velocity distribution. Next, Dix inversion computes interval velocities from the rms velocities [*Dix*, 1955]. Drawbacks to the latter method include limited lateral velocity variations and errors associated with NMO assumptions which include small offset-to-depth ratios, small vertical and horizontal velocity gradients, and planar flat-lying reflections [*Al-Chalabi,* 1973; *Al-Chalabi*, 1974; *Yilmaz,* 2001].

Several studies show significantly improved images when an entire GPR survey is acquired with CMP geometry [*Bradford*, 2003; 2004; *Bradford*, 2006; *Bradford and Deeds*, 2006; *Deeds and Bradford*, 2002; *Fisher et al.*, 1992; *Greaves et al.*, 1996; *Liberty and Pelton*, 1994; *Pipan et al.*, 1999; *Pipan et al.*, 2003]. With CMP acquisition,

multi-trace reflection seismic processing methods can be applied for accurate depth imaging from laterally and vertically continuous GPR velocity measurements. An additional advantage of CMP data includes improved suppression of coherent and random noise.

In this paper we present a method to obtain spatially distributed porosity estimates in the substream environment. We use the continuous multi-offset (CMO) method to image the hyporheic zone and subsurface porosity in four arctic streams north of the Brooks Range, AK, and a temperate stream site within the Sawtooth Mountains near Boise, ID, USA. Our primary objective was to accurately image GPR velocity structure, then use these measurements to estimate porosity distribution using the petrophysical relationship defined by the Topp equation [*Topp et al.*, 1980]. This information will provide input to future hyporheic flow and heat flow models to better understand hyporheic zone processes.

3.3 Methods

Employing CMO methods over stream channels is more challenging than land based surveys. One difference is determining a feasible method to successfully bridge across actively flowing steam channels while maximizing coupling between the antennas and the earth surface. Additionally, results can be largely affected by rapid elevation changes from stream banks to the active channel which can be accounted for with an accurate elevation survey of the profile line. Perhaps the greatest challenge however, is imaging the large velocity contrast present at the transition from free flowing water, in

the stream channel, to water saturated sediments where the velocity may increase by a factor of three or more. This change can occur laterally across nearly vertical boundaries thus severely violating the assumptions of NMO analysis and necessitating more accurate velocity estimation and prestack depth imaging techniques.

At all sites, CMO data were gathered by extending a 25 – 30 cm wide board across the stream, just above the stream water flow level. This board then served as a bridge along which we acquired GPR measurements. Traces were gathered in common source gathers by incrementally stepping the receiver across the stream at a set distance interval while the transmitter remained stationary. Once completed, the transmitter was moved a set distance along the profile line and the process repeated until the transmitter reached the end of the profile.

Premigration processing steps for all data sets include time zero correction, bandpass filtering, amplitude correction, and/or automatic gain control that varied by site. For the arctic sites an additional three-CDP mix is included to improve the stacking display. Initially, NMO velocity analysis with constant stacking velocities was applied to each data set and produced significant improvements in signal to noise (S/N) ratio when compared to the conventional common-offset image. NMO assumptions are violated in the stream environment where the velocity increases from ~0.032 m ns^{-1} in the stream water to 0.05 – 0.08 m ns^{-1} in the surrounding saturated sediments [*Brosten et al.*, 2006]. Additionally, the reflector geometries in the substream environment often proved to be complex with steeply dipping and truncated reflectors. We applied prestack depth

migration (PSDM) and reflection tomography to improve velocity estimates and image accuracy.

The PSDM process requires a starting velocity model as initial input then the velocity model is refined iteratively until a good migration result is obtained. Our method for deriving the starting model varied by site (see site specific descriptions below). The output of PSDM is a set of common image point (CIP) gathers that display reflector horizons as a function of offset and depth. When the correct velocity is used the reflection depth is independent of offset, whereas incorrect velocity leads to reflectors displaying apparent offset dependence. This offset dependent depth is defined as residual moveout (RMO).

To derive the final velocity model we utilized Stork's [1992] method of reflection tomography which consists of tomographic inversion to minimize RMO in the post-migration domain.. A typical processing sequence goes as follows: PSDM is applied with the starting velocity model, RMO is computed for a selected reflector, tomography updates the velocity model, and PSDM is applied with the new velocity model. This process continues iteratively until the RMO is minimized for all coherent reflectors. For a detailed review of PSDM with reflection tomography as applied to GPR imaging, see [*Bradford*, 2006; *Bradford*, 2008].

3.4 Field Examples

3.4.1 Arctic Sites

Gathering GPR reflection data to study frozen ground in the arctic regions has been well documented by an extensive number of published investigations [*Annan and Davis*, 1976; *Arcone and Delaney*, 1982; *Arcone et al.*, 1998b; *Delaney et al.*, 1990; *Hinkel et al.*, 2001; *Moorman et al.*, 2003]. Fewer published studies exist which focus on identifying thaw features and the active layer thaw beneath arctic streams and rivers [*Arcone et al.*, 1992; *Arcone et al.*, 1998a; *Bradford et al.*, 2005; *Brosten et al.*, 2006]. Many of the above mentioned studies successfully used wide-angle reflection and refraction (WARR) in conjunction with conventional constant transmitter-receiver offset surveys to exploit the low permittivity of permafrost underlying a seasonal thaw to determine permittivity and velocities of the two layers. But these were only for single or sparsely located locations which does not allow for PSDM or laterally continuous velocity measurements.

The Arctic stream sites we studied are located within the Kuparuk watershed north of the Brooks Range, AK, where the drainage area is underlain by continuous permafrost with thicknesses ranging from 250 m near the foothills to over 600 m near the coast [*Osterkamp and Payne*, 1981]. Based on results from the 2004 fieldwork campaign [*Brosten et al.*, 2006] four sites were selected and revisited for CMO data collection in early August 2005 (Figure 3.2). The stream sites encompassed two general geomorphologic conditions found in rivers and streams on Alaska's North Slope; 1) low-

energy water flow, organic material lining, beaded morphology, 0.90% gradient, and 2) high-energy water flow, riffle-pool-riffle morphology, cobble to gravel material lining, 0.97 –1.18% gradient.

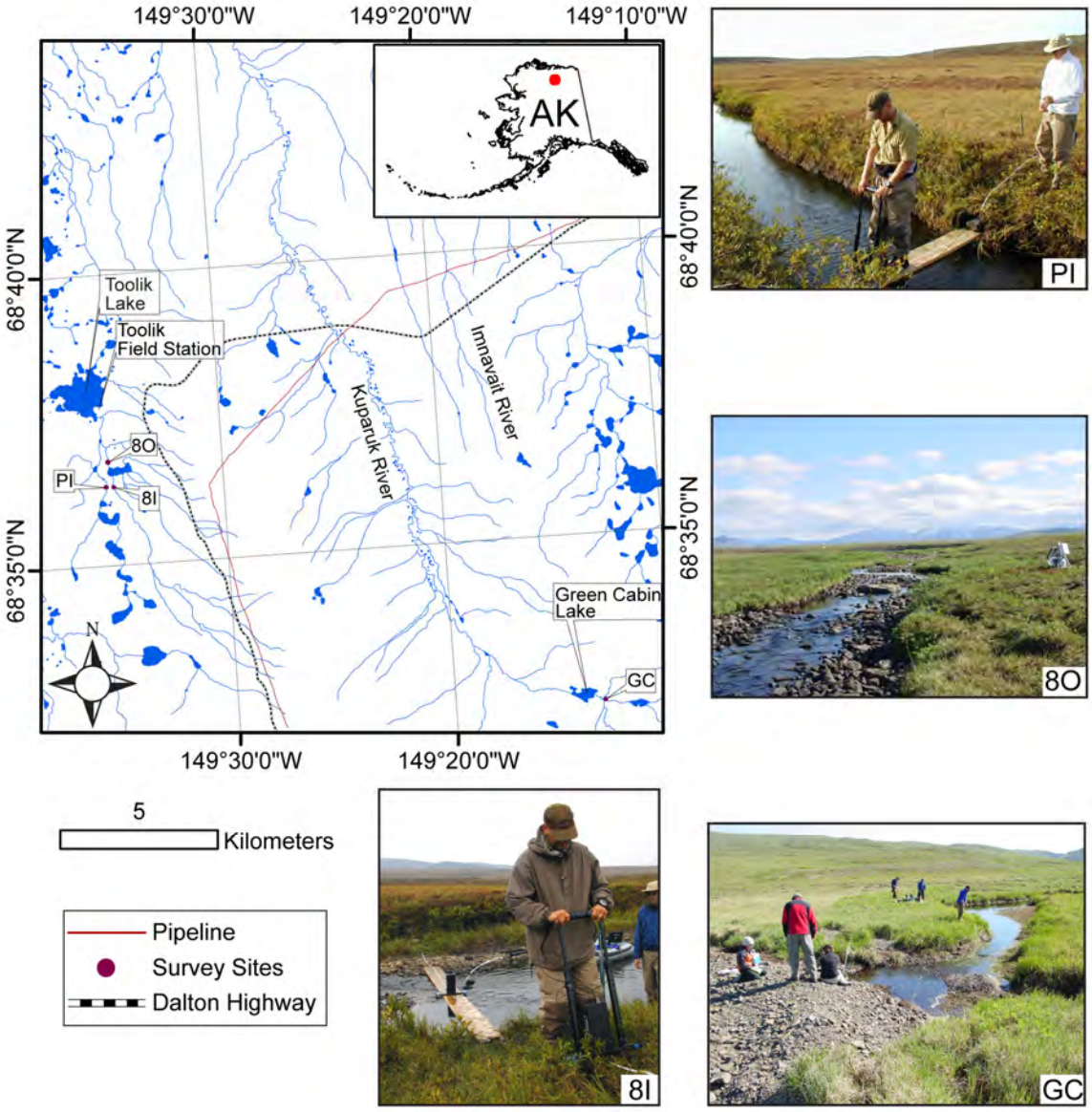

Figure 3.2. Locations and photos of four arctic stream study sites (8I, 8O, PI, and GC) within the Kuparuk watershed, AK.

All of our arctic sites have the potential to contain some fraction of peat or sand and cobble sediments. Therefore, we use Topp's general equation and estimate an uncertainty of ±5% in porosity values based on Topp's relationships for equivalent sand and organic soil types. We expect that values for sand dominated sites may be overestimated by 5% and values within the peat dominated sites may be underestimated by 5%. Past studies, e.g. Ponizovsky et al. [1999], comparing estimates from Topp's equation to laboratory measurements reported a good fit for sand material. We acknowledge the uncertainty in our porosity measurements, specifically within the peat dominated sites, but maintain that GPR can provide laterally and vertically continuous porosity approximations, within 5% accuracy, beneath stream channels.

3.4.1.1 Peat Inlet Stream Site (PI), AK

The Peat Inlet (PI) is the first of two low-energy peat lined stream sites. The profile along the PI stream was collected across one of the deeply incised connecting channels located ~0.5 km north of Toolik Field Station. We started trace gathers at the PI site 2 m in from the stream channel on the stream bank right side, continued across the stream and ended 3 m in from the stream channel on the stream bank left side. Data were acquired with 200 MHz antennas in common-source point gathers with 0.2 m receiver and 0.4 m source intervals, 0.6 m near offset. Additional acquisition details are given in (Table 3.1) and apply to all the arctic sites.

Table 3.1. Acquisition Parameters for the Arctic Stream Sites, North Slope, AK.

Survey Type	Transverse electric, 2D
GPR system	Sensors and software, Pulse EKKO 100-A, 200-MHz unshielded antennas, 1000 V transmitter
Min/max offset	0.6 m/12 m
No receivers/source	up to 58
Source interval	0.4 m
Receiver interval	0.2 m
Sampling interval	0.4 ns
Recording time	300 ns
No. stacks/source	8

The deeply incised bank sides of the PI site made the reflection tomography processing steps more challenging. We migrated only the near offset data, 60 cm, using a water velocity at 0.032 m ns^{-1} in order to locate the water bottom in the image. Then, for the starting velocity model we set the water channel, in the proper spatial location, to 0.032 m ns^{-1} and the remaining area to 0.055 m ns^{-1} based on scattering diffraction velocities noted by Bradford et al. [2005]. They achieved good migration results by including a positive vertical velocity gradient within the seasonal thaw layer that is consistent with lithology grading from saturated peat to water-saturated sand/gravel. We used the velocity model that resulted from our first-pass reflection tomogram analysis to migrate the image. Due to significant topography variations at this site the image was corrected to a local datum generated from elevation measurements collected along the profile line. The resulting image illustrates an excellent active layer/permafrost boundary reflector easily seen on both sides of the stream bank and underneath the stream as well

(Figure 3.3a). The moisture content model shows fairly homogenous porosity estimate of ~43% throughout the active-layer (Figure 3.3b).

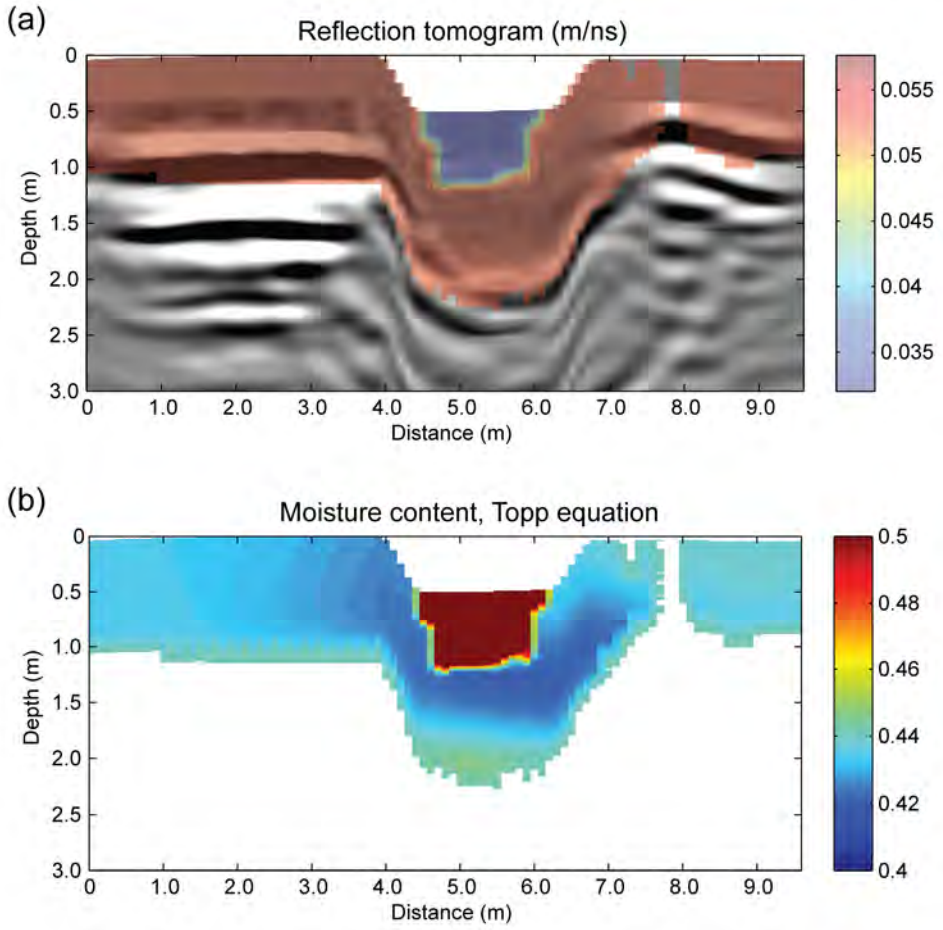

Figure 3.3. (a) PSDM image of PI profile with the reflection tomogram used for migration overlaid. (b) Moisture content estimated from the velocity model in (a), colors have been scaled to show variations in the thaw layer.

Common-source gathers illustrate strong subsurface refraction events from the velocity increase between active layer and frozen soil (e.g. Tx @ 0 m, Figure 3.4a, indicated by yellow arrows). These events become less apparent and the direct wave disappears completely as the transmitter moves across the profile (Tx @ 3.2 and 5.6 m)

due to rapid topography changes along the profile line. A reflection event from the active layer/permafrost boundary in the first gather (Tx @ 0.0 m) is barely evident at the near offset before it is obscured by refraction energy. The backdipping moveout shown by the reflection in the third gather located over the stream channel (Tx @ 5.6 m) results from a steeply dipping reflector. A synthetic common-source gather (last gather in Figure 3.4a) was generated using a 4^{th} order finite difference solution of the scalar wave equation. The synthetic gather was evaluated against the common-source gather collected at the start of the profile line (Tx @ 0 m) to verify model velocities. The model includes a 2 m layer of air to account for the air wave and permafrost/air mixing in the refraction phase, 1 m by 2 m water channel at 0.032 m ns^{-1}, 1m thick active layer with a velocity at 0.055 m ns^{-1} for saturated peat, all underlain by continuous permafrost at 0.168 m ns^{-1} (Figure 3.4b). Similar refraction events, indicated by yellow arrows from left to right, represent the direct wave, thaw/frozen refraction, direct wave through the water channel, and the thaw/frozen refraction on the far side of the channel. A reflection event from the active/permafrost boundary that arrives at ~40 ns near offset (black arrows) is also evident within both gathers. This demonstrates that, despite the simplified model, the synthetic velocity model is a reasonable representation of the true velocity distribution.

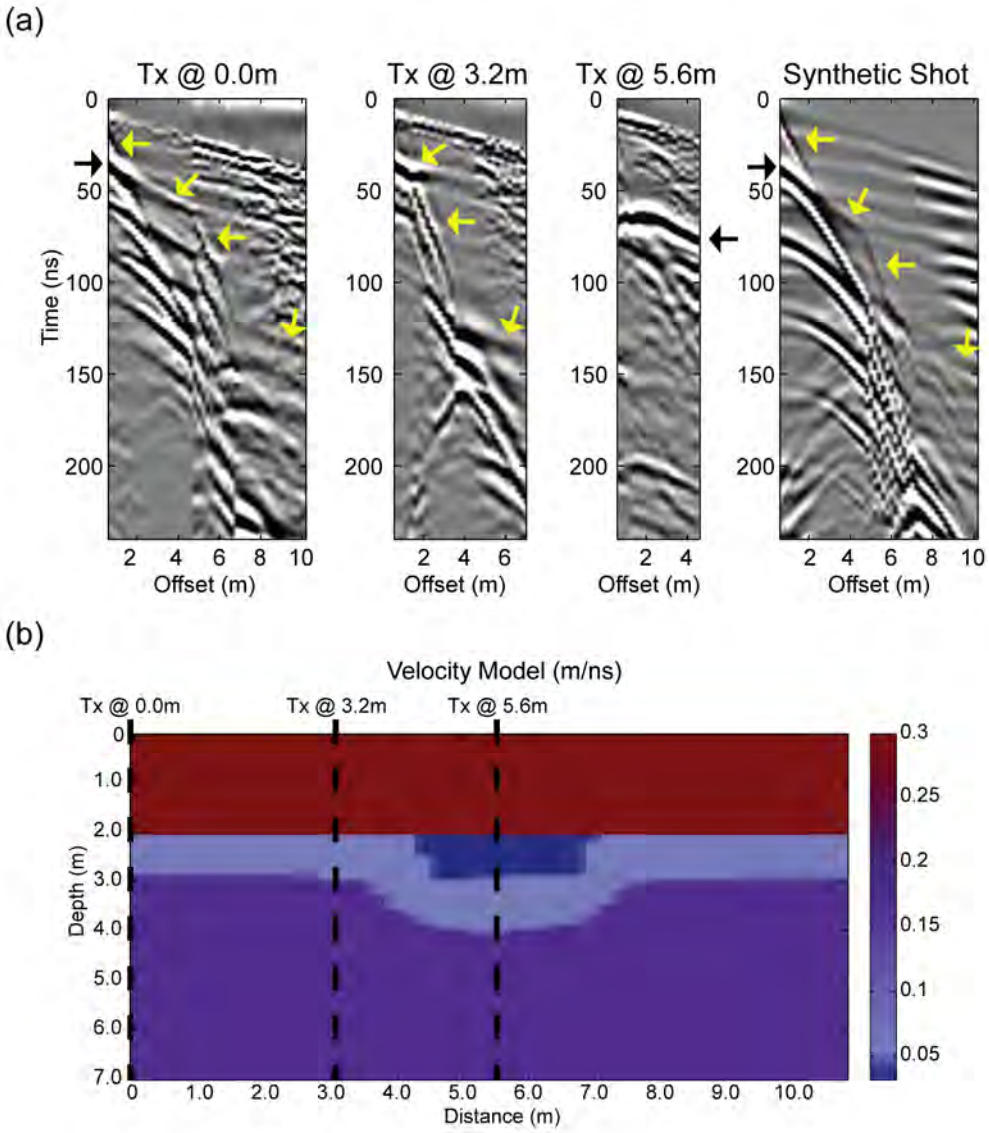

Figure 3.4. (a) Filtered and gained common-source gathers along PI profile. Note that the last gather is a synthetic. Black arrows indicate the thaw/frozen reflection event and yellow arrows, from left to right, for Tx @ 0.0m and synthetic shot represent the direct wave, thaw/frozen refraction, direct wave through the water channel, and the thaw/frozen refraction on the far side of the channel. Yellow arrows, from left to right, for Tx @ 3.2m shot gather represent thaw/frozen refraction, direct wave through the water channel, and the thaw/frozen refraction on the far side of the channel. Tx @ 5.6m is over the stream channel and shows a strong dipping reflection from backdipping moveout. (b) Velocity model used to generate a synthetic common-source gather with the same source and receiver spacing as Tx @ 0.0m for comparison.

We should note here that seasonal time-lapse common-offset GPR data were collected at this same profile line in the summer of 2004 [*Brosten et al.*, 2006]. The migrated data (Figure 3.3a) show thaw depths up to 1 m (about 0.35 m greater than the August 2004 interpretation). This is partly due to a higher velocity obtained from the reflection tomography analysis, ~0.057 m ns^{-1}, in comparison to the migration velocity of 0.05 m ns^{-1} used in the previous study. The remaining discrepancy is likely due to differences in the correctly interpreted water-bottom reflection caused by small permittivity contrast between the water and organic material lining the channel.

3.4.1.2 Green Cabin Lake Inlet Stream Site (GC), AK

The second low-energy study site (GC) is the right channel entering a confluence located upstream of Green Cabin Lake. The profile at this site was gathered across one of the connecting channels characterized by a shallow, actively flowing, stream with minimal channel incision. The site is located at a higher elevation than the other three sites resulting in cooler seasonal temperatures and therefore a shallower thaw depth is estimated at ~0.61 m (Figure 3.5a). The porosity estimates (Figure 3.5b) were slightly higher than those estimated at the PI site, specifically within a small area beneath the stream just above the permafrost (at 4 m along the profile line) that could represent a small pocket of localized sand disposition. This profile line was also studied during a field campaign in 2004 [*Brosten et al.*, 2006] however, the interpreted thaw depth from the 2005 profile is only ~0.11 m greater than the 2004 profile. Given the more rigorous approach to velocity estimation in the present study, we believe that these velocities are

more reliable and the thaw depth estimate is likely more accurate in this case, however it is not unreasonable to expect annual variations in the maximum thaw depth.

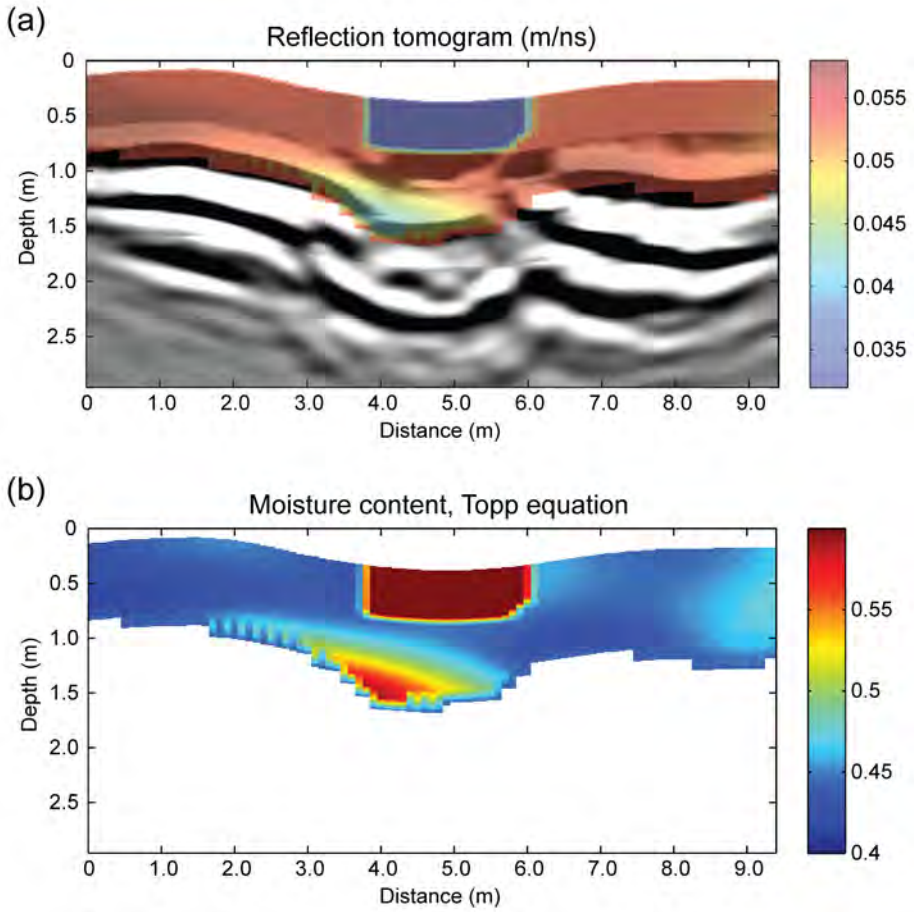

Figure 3.5. (a) PSDM image of GC profile with the reflection tomogram used for migration overlaid. (b) Moisture content estimated from the velocity model in (a), colors have been scaled to show variations in the thaw layer.

3.4.1.3 I-8 Lake Inlet Stream Site (8I), AK

The first high-energy gravel-lined stream site (8I) is located on the inlet stream to I-8 Lake and is in close proximity to the PI site (Figure 3.2). The CMO profile is located just downstream of a riffle section. The line starts on the stream bank left side on top of

an exposed gravel bar that extends along the line for the first 3 m of the line. The last trace gather ends on the stream bank right side ~3 m onto the terrestrial tundra.

Common-source gathers along the line illustrates the difficulty in interpreting reflection events (Figure 3.6). The thaw/frozen boundary in the first gather (Tx @ 0.0 m) is downward dipping causing the apex of the corresponding reflection event to occur well before the near offset trace (black arrow). Most of the leg from the same reflection is obscured by the direct wave where the interpreted near offset arrival is at ~60 ns. The second and third gathers display a reflection (annotated by black arrows) arriving at ~75 and ~100 ns, respectively and is interpreted as the thaw boundary reflection. The reflection event at ~100 ns in the last gather (Tx @ 6.8 m) exhibits a similar moveout to the one noted in the PI gather (Figure 3.4a, Tx @ 5.6 m) indicating an upward dipping event possibly caused by a rapid decrease in the thaw/frozen boundary. There is also a clear refraction event from the thaw/frozen boundary within the three gathers (yellow arrows) that arrives sooner as the transmitter steps down the line indicating a decrease in thaw towards the right side of the profile line. These refraction events are traveling upslope on the far side of the stream profile and therefore have high apparent velocities.

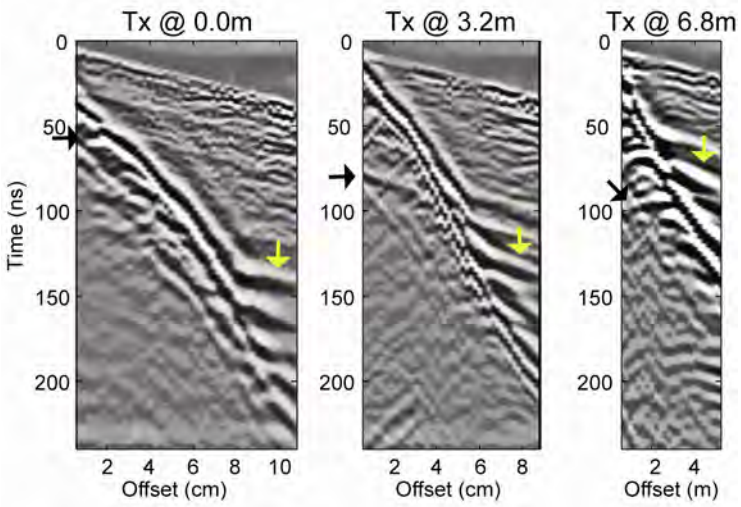

Figure 3.6. Filtered and gained common-source gathers along 8I profile. Black/yellow arrows show locations of reflection/refraction events, respectively, within each gather.

Values for the starting depth-velocity model were incorporated from velocities generated by Bradford et al. [2005]. Based on their results we used 0.075 m ns^{-1} as our starting depth-velocity model. Multiple coherent reflectors within the cross-section produced a velocity model displaying excellent detail in lateral velocity changes within the subsurface. The migrated image shows preferential thaw towards the exposed gravel bar for a maximum thickness of ~2.6 m (Figure 3.7a), likely due to enhanced heat conduction into the subsurface from exposed gravel warming up from solar radiation.

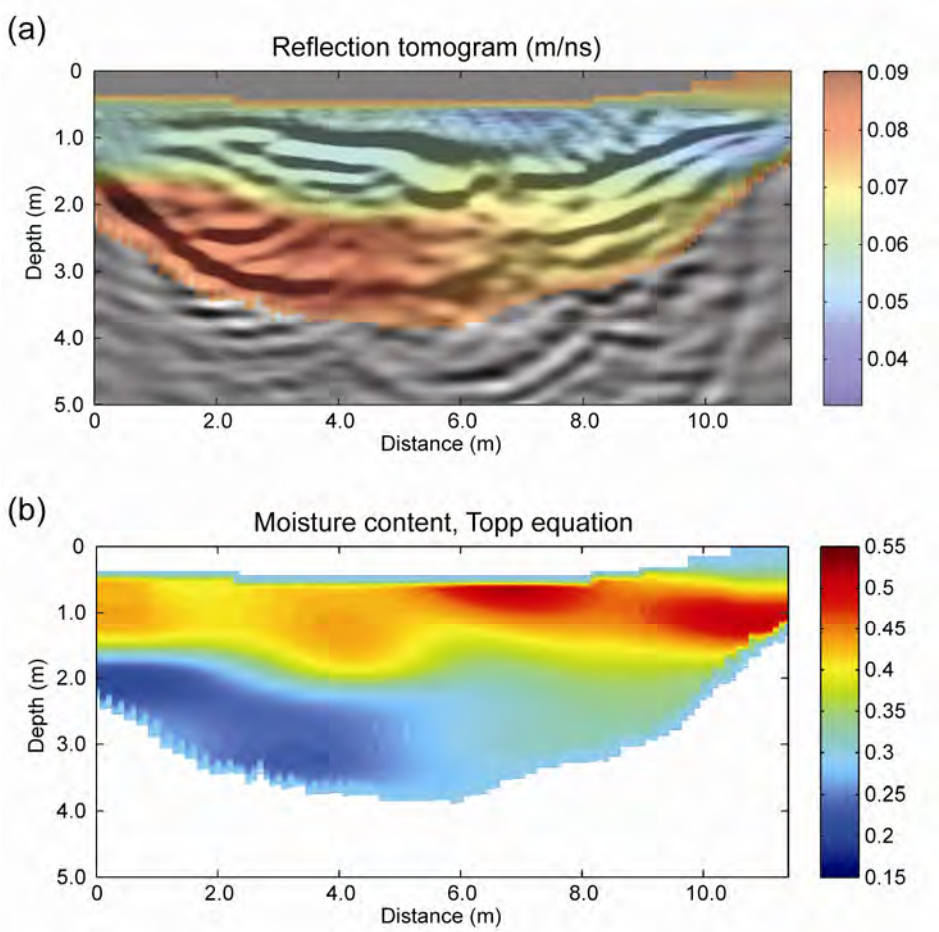

Figure 3.7. (a) PSDM image of 8I profile with the reflection tomogram used for migration overlaid. (b) Moisture content estimated from the velocity model in (a).

Porosity estimates are highest beneath the active stream channel and just beneath the peaty tundra on the stream bank right side. Moisture content is noticeably higher within the upper 1.5 m of the subsurface with a gradual decrease to ~20% beneath the gravel bar (Figure 3.7b).

3.4.1.4 I-8 Lake Outlet Stream Site (8O), AK

Trace gathering at the 8O site started just over 2 m to the left of the stream bank left side. Gathers were collected across the stream up to 3 m past the stream bank right side.

We were unable to use reflection tomography to refine the velocity model due to poor S/N in the post migration domain; however, the constant velocity stacked image from this site shows significant improvement in the S/N ratio in the multi-offset profile in comparison to the conventional common-offset profile (Figure 3.8). A pseudo common-offset GPR section was created by combining traces with 0.6-1.2 m offsets and constant-velocity (0.085 m ns^{-1}) normal moveout (Figure 3.8a) for comparison to the CMP stack generated with offsets up to 4.6 m and the same stacking velocity (Figure 3.8b). There is a noticeable improvement in the thaw/frozen boundary reflection beneath the stream at ~100 ns (~ 3.4 m maximum thaw depth). Our failure to generate a reasonable velocity model at this site emphasizes the extreme heterogeneity that can occur within these high-energy gravel-lined sites. In this case, the noise is primarily coherent noise caused by multiple 3D scattering near the streambed where the sediments consist of cobble to boulder sized material. This strong scattering also results in greater signal attenuation exacerbating the problem.

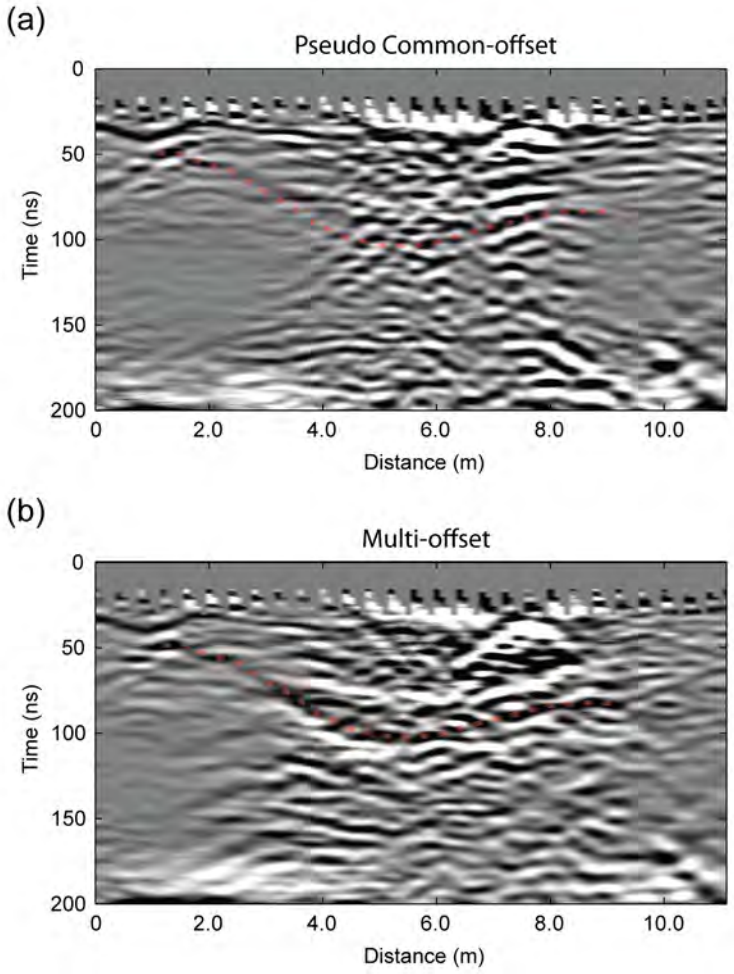

Figure 3.8. (a) Pseudo common-offset stack (0.085m/ns) at 8O site with 0.60-1.2m offsets (- - active layer/permafrost boundary). (b) Multi-offset stack (0.085 m/ns) with 0.60-4.6m offsets. There is noticeable improvement in the S/N ratio illustrated by a stronger reflector representative of the active layer/permafrost boundary beneath the stream (100 ns) (- - active layer/permafrost boundary).

3.4.2 Temperate Stream Site

Our research team acquired CMO data late September 2007 at an inlet stream that drains into Bull Trout Lake (BT), located within the Sawtooth Mountains near Boise, ID, USA (Figure 3.9). BT is a temperate, sand and gravel lined, low gradient (<0.05 m m^{-1}), riffle-pool-riffle morphology, with a drainage area of 9.7 km^2 at the lake inlet [*Arp et al.*,

2007]. The inlet stream lining is composed of late Pleistocene unsorted to moderately sorted sandy boulder till, sandy gravel, and coarse sand [*Freed et al.*, 2006].

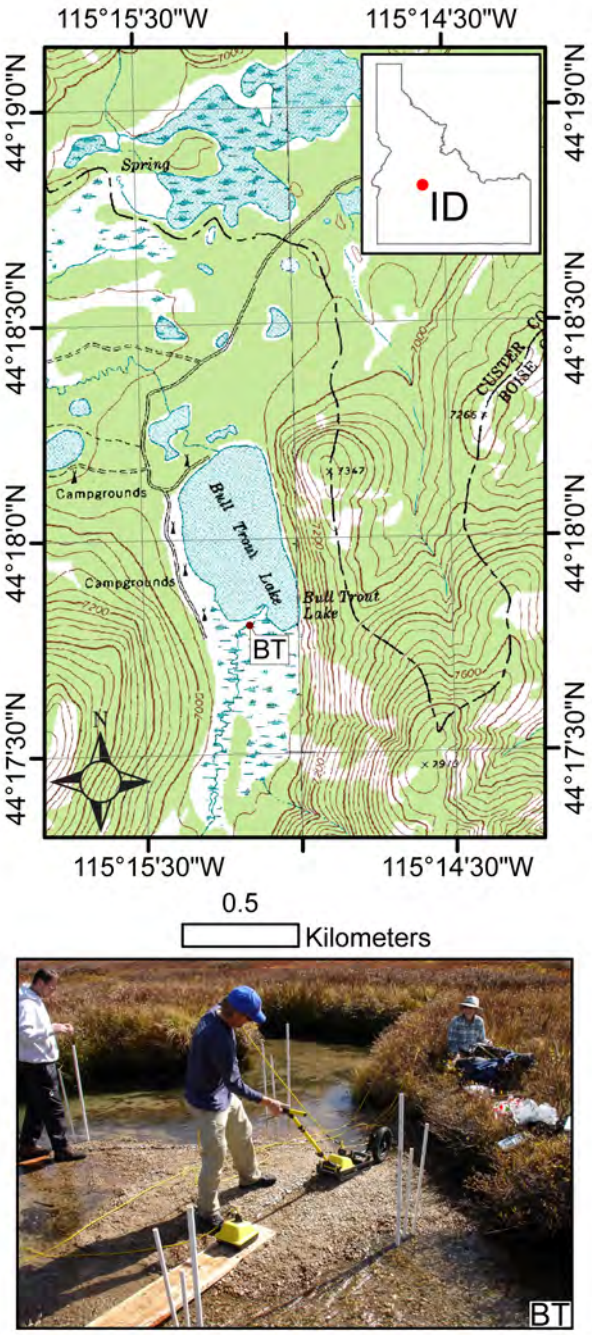

Figure 3.9. Location and photo of temperate stream site (BT) above the inlet of Bull Trout Lake, ID.

The collection method was similar to the method used in the arctic studies except that shielded 500 MHz antennas were used for data collection. In addition, the receiver was placed on a sled and triggered every 0.05 m, by an attached odometer wheel, as it was pushed away from the transmitter, starting at 0.1 m near-offset up to a maximum of 2m far-offset. Once completed, the transmitter was moved 0.1 m along the profile line and the process was repeated until the transmitter reached the end of the profile. Additional acquisition details are given in (Table 3.2).

Table 3.2. Acquisition Parameters for the Temperate Stream Site, Bull Trout Lake, ID.

Survey Type	Transverse electric, 2D
GPR system	Sensors and software, Pulse EKKO PRO, 500-MHz shielded antennas, 185 V transmitter
Min/max offset	0.1 m/2 m
No receivers/source	39
Source interval	0.1 m
Receiver interval	0.05 m
Sampling interval	0.2 ns
Recording time	100 ns
No. stacks/source	16

Multiple CMO data lines were gathered across a number of different stream features at this site. For the purpose of this paper, and to minimize redundancy, we will show only one of the profiles. The CMO profile started on the stream bank left side with the foot of the board embedded into the bank just above the water line. The line continued across 2 m of active channel and then continued and additional 2.5 m across a well-sorted sand/gravel point bar. Strong reflection events are evident throughout the

profile as illustrated by the common midpoint (CMP) gathers shown in Figure 3.10. High variability in the distribution of reflectors in the CMP gathers indicates significant subsurface complexity.

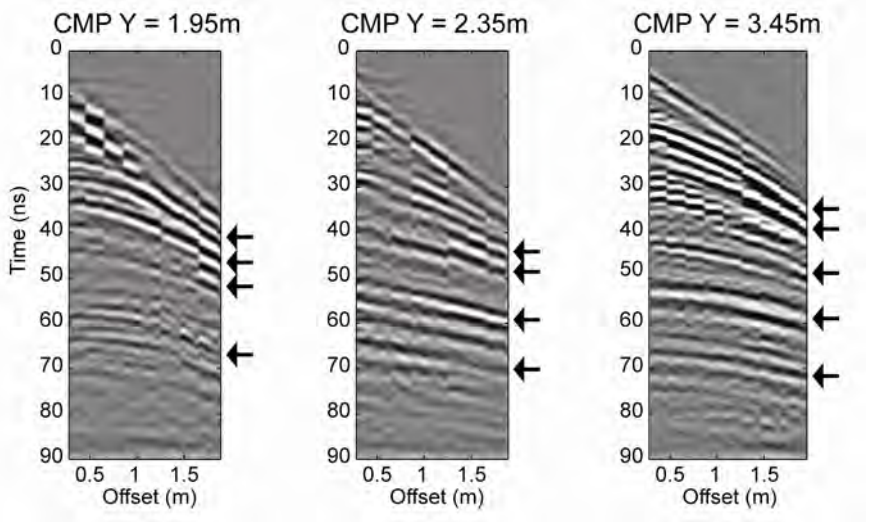

Figure 3.10. Common midpoint gathers (arrows indicate strong reflection events).

Clear reflectors from past channel erosion and deposition are seen at 0.5-1 m depth starting on the right side of the profile (gravel bar) and dipping downward towards the active channel on the left. Based on NMO analysis we used 0.065 m ns^{-1} for water-saturated sands as our starting depth-velocity model for the temperate stream site. The resulting reflection tomogram show slower velocities (~0.06 m ns^{-1}) along the same reflectors overlaying a faster velocity (~0.075 m ns^{-1}) layer that is confined by another slower velocity layer (0.065 m ns^{-1}) marked by strong reflectors at ~1.75 m (Figure 3.11a). The corresponding porosity estimates illustrate a distinct lower porosity content layer (~0.25%) enclosed by higher porosity layer (~0.35-.045%) above and below (Figure

3.11b). This noticeable layering indicates more porous well-sorted sand/gravel layers bounding a less porous poorly-sorted gravel layer.

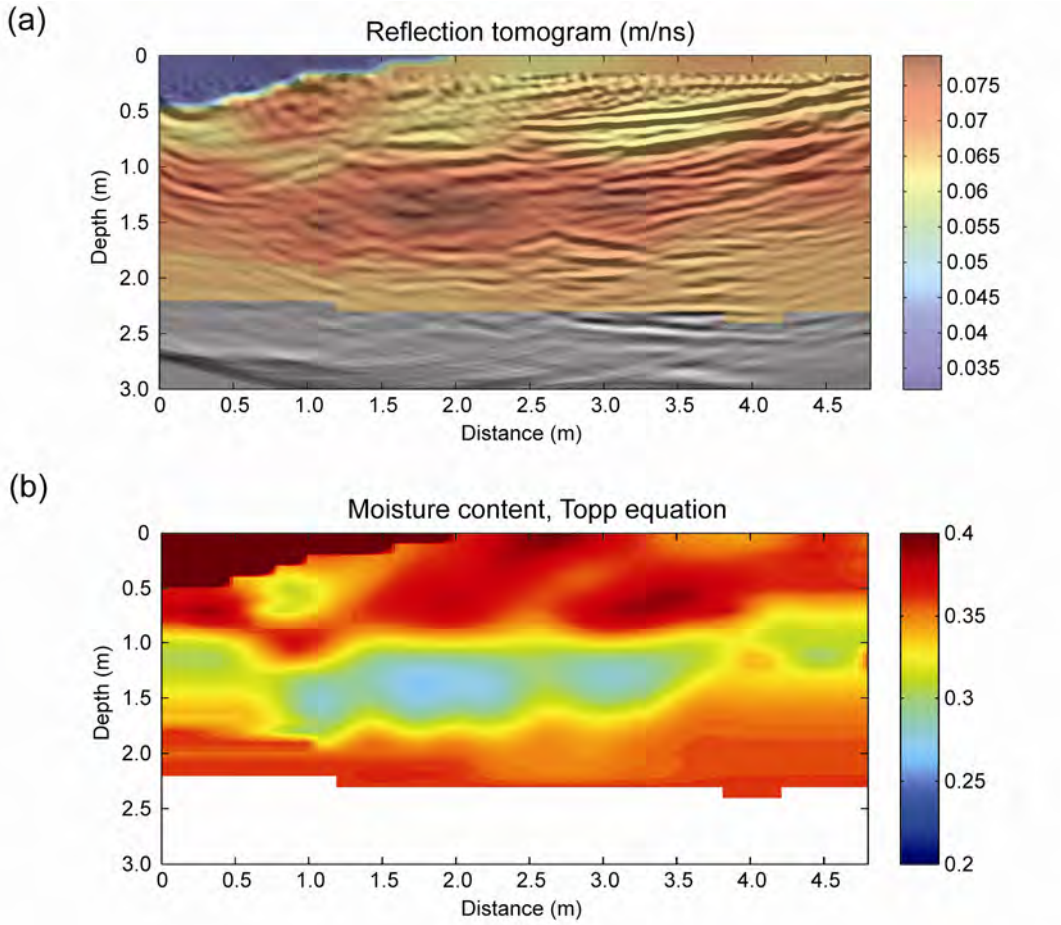

Figure 3.11. (a) PSDM image of BT profile with the reflection tomogram used for migration overlaid. Note the stream channel bottom at 0.5 m on the left and the highly coherent reflection layering beneath the gravel bar on the right side. (b) Moisture content estimated from the velocity model in (a), colors have been scaled to show variations in the saturated zone. The moisture content model provides an excellent display of layering from a high porosity material overlaying a lower porosity layer overlaying another high porosity layer.

3.5 Conclusions

Results from the five field sites presented in this study illustrate the benefits of continuous multi-offset GPR data including significant improvement in S/N ratio within the stacked GPR profiles, leading to a more detailed and confident interpretation. The field data example at Bull Trout Lake, BT, shows excellent detail of individual deposition events in addition to three distinct porosity layers revealed through reflection tomography analysis. The gravel-lined stream site results from the arctic studies illustrate a detailed lateral depth-velocity model at the 8I site but not 8O due to insufficient coherent reflectors. Our ability to generate an appropriate velocity model at 8I but not 8O suggests a high degree of the 3D diffraction scattering likely due to irregular high-energy depositional events. Whereas the depth-velocity models from the peat-lined stream sites show more homogenous constant velocities representative of the active layer thaw.

Continuous multi-offset GPR methods have the advantage of providing laterally continuous measurements of subsurface stratigraphy and properties, whereas borehole methods provide detailed vertical measurements at a single point. While more time consuming than conventional single offset methods, CMO profiles can be acquired and analyzed rapidly relative to the time required to install, sample and analyze borehole data. The real strength of the method is seen by combining a few direct borehole measurements with laterally extensive radar measurements.

PSDM methods, along with reflection tomography analysis, provide detailed depth-velocity models and migrated GPR profiles for interpretation. Through petrophysical relationships detailed porosity estimates beneath various stream environments can be

achieved. A large number of cross-sectional porosity measurements are obtained through non-invasive methods and provide a high degree of lateral detail that, in turn, provides information of the spatial distribution of hydraulic properties. These in-situ estimates can improve and help constrain hydrological and thermal models.

4 ESTIMATING 3D VARIATION IN ACTIVE-LAYER THICKNESS BENEATH ARCTIC STREAMS USING GROUND-PENETRATING RADAR

4.1 Abstract

We acquired three-dimensional (3D) ground-penetrating radar (GPR) data across three stream sites on the North Slope, AK, in August 2005, to investigate the dependence of thaw depth on channel morphology. Data were migrated with mean velocities derived from multi-offset GPR profiles collected across a stream section within each of the 3D survey areas. GPR data interpretations from the alluvial-lined stream site illustrate greater thaw depths beneath riffle and gravel bar features relative to neighboring pool features. The peat-lined stream sites indicate the opposite; greater thaw depths beneath pools and shallower thaw beneath the connecting runs. Results provide detailed 3D geometry of active layer thaw depths that can support hydrological studies seeking to quantify transport and biogeochemical processes that occur within the hyporheic zone.

4.2 Introduction

Developing an understanding of the permafrost and active layer in the arctic has been a primary research topic for numerous studies. Research has included permafrost and active layer temperature measurements to show the affects of changes in climate on past

and present thermal regime within the arctic tundra [*Kane et al.*, 1991; *Lachenbruch and Marchall*, 1986; *Osterkamp and Gosink*, 1991; *Osterkamp et al.*, 1994; *Romanovsky and Osterkamp*, 1995]. In addition to temperature measurements, two-dimensional (2D) ground-penetrating radar (GPR) has been used extensively in the arctic to study active layer and permafrost features [*Annan and Davis*, 1976; *Arcone and Delaney*, 1982; *Arcone et al.*, 1993; *Arcone et al.*, 1998b; *Arcone and Delaney*, 2003; *Bradford and Deeds*, 2006; *Delaney et al.*, 1990; *Doolittle et al.*, 1990; *Doolittle et al.*, 1992; *Hinkel et al.*, 2001]. GPR has also been employed to study active layer thickness and development across arctic streams and rivers [*Bradford et al.*, 2005; *Brosten et al.*, 2006], taliks [*Arcone et al.*, 1992; *Arcone et al.*, 1998a], and river channel morphology [*Best et al.*, 2005].

Advances in data processing software and data acquisition instruments have enabled research methods to expand to three-dimensional (3D) data collection and analysis for a more complete characterization of subsurface structures. 3D GPR has been used in multiple research areas including archaeology [*Grasmueck et al.*, 2004; *Leckebush*, 2003; *Leucci and Negri*, 2006; *Negri and Leucci*, 2006], geology [*Asprion and Aigner*, 1999; *Beres et al.*, 1995; *Guidry et al.*, 2007; *Kostic and Aigner*, 2007], hydrology [*Bradford and Wu*, 2007; *Bradford*, 2008; *Kruse et al.*, 2006], and geological engineering applications [*Anderson et al.*, 2007; *Grasmueck*, 1996]. However, the benefits provided by 3D GPR to map near-surface structures in permafrost environments has not, as of yet, been fully exploited. One recent investigation took advantage of the dielectric contrast between ice wedges and the surrounding material using 3D GPR to

interpret the 3D geometry of ice-wedge polygons on the Arctic Coastal Plain of northern Alaska [*Munroe et al.*, 2007].

The movement of stream water flowing into the near sub-surface and back out to the stream channel is known as hyporheic exchange flow (Figure 4.1). The extent of this exchange resides within the active layer and defines the hyporheic zone. Studies have shown that hyporheic exchange processes have a significant effect on biogeochemical cycling within stream ecosystems [*Gooseff et al.*, 2002; *Jones et al.*, 1995; *Mulholland et al.*, 1997] and temporary storage of stream water [*Harvey and Wagner*, 2000]. Through 2D modeling efforts Zarnetske et al. [2008] found that hyporheic exchange, within arctic streams, occurs up to a threshold depth primarily determined by hydraulic head gradients established by the stream morphology. Currently hydrological and biological studies of the hyporheic zone are conducted without much knowledge of the 3D subsurface architecture [*Wright et al.*, 2005]. Information provided by 3D GPR will improve hyporheic zone groundwater flow modeling by constraining the model domain in 3D space thereby reducing the uncertainty associated with transport processes such as water and solute exchange. 3D geometry is particularly important in the arctic regions where active layer thaw may limit hyporheic extent. It is critical to know the 3D distribution of the thaw depth to improve hyporheic studies seeking to quantify water storage and biogeochemical processes. This study provides a more complete characterization of the active layer geometry beneath arctic streams with the use of 3D GPR methodologies.

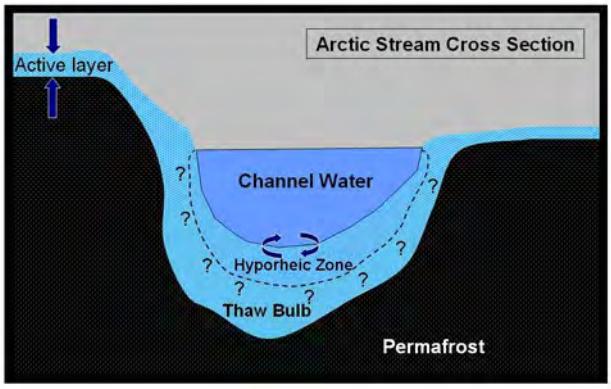

Figure 4.1. The extent of the hyporheic zone is defined as the area where channel water and subsurface water mix. In arctic streams the hyporheic zone exists within the seasonal thaw layer, defined as the thaw bulb beneath the streams [*Greenwald et al.*, 2008].

3D GPR data were acquired at three stream sites within the Kuparuk watershed on the North Slope, AK, (Figure 4.2) where continuous permafrost depths reach depths of 250 m near the foothills to over 600 m near the coast [*Osterkamp and Payne,* 1981]. In general streams on the North Slope, Alaska, can be grouped into two geomorphologic stream types. The first stream type is a high-energy stream system with cobble to gravel streambed lining and riffle-pool morphology (alluvial stream). The second stream type is a low-energy flow stream system with beaded morphology (pools connected by short runs) and organic streambed lining (peat stream). Survey grids were established to encompass local streambed features including either a pool/riffle or pool/run sequence. We selected sites based on results from time-lapse 2D GPR profiles collected previously at five study sites [*Brosten et al.*, 2006]. This paper expands on knowledge obtained from previous studies on arctic stream characterization using 3D GPR to provide detailed geometry of the seasonal thaw depth related to changes in local streambed features.

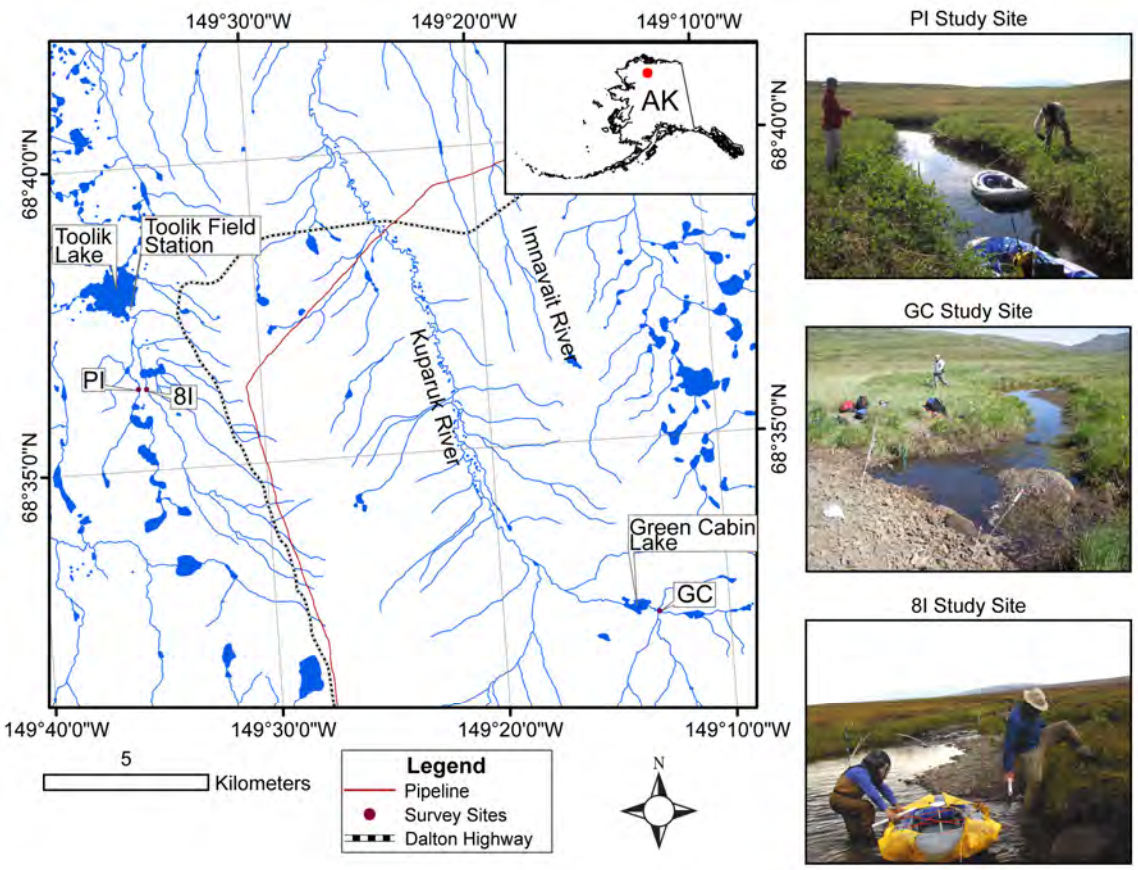

Figure 4.2. Locations of the three study sites selected for 3D GPR acquisition.

4.3 Methods

GPR data were acquired the second week of August 2005 using a Sensors and Software PE100A pulsed radar system with a 1000V transmitter. The transmitting and receiving 200 MHz antennas were placed at the bottom of a small rubber boat for data acquisition. Profile lines were gathered by pulling the boat across the stream ~1 m past the channel bank-to-bank while triggering at a constant time interval. Lines were collected at ~0.3 m intervals and continued upstream until a pool-riffle sequence was covered (Table 4.1). Precise spatial data were collected using differential global positioning system (DGPS) calibrated to the GPR system. Spatial data were corrected to

GPS base station data recorded at Toolik Field Station, AK (Figure 4.2) and then filtered to remove outliers over 0.05 m horizontal and 0.17 m vertical precision. After filtering over 95% of the remaining data points were within <= 0.05 m and 0.1 m horizontal and vertical accuracy, respectively. The following processing steps were applied to each dataset:

Table 4.1. GPR Acquisition Parameters.

System	Sensors & Software PE100A
Transmitter	1000 V
Antennas	200 MHz
# stacks/Trace	8
Trace Acquisition	0.2 s
Sampling Rate	0.4 ns
Recording Time	300 ns
Nominal Inline Trace Spacing	0.02-0.03 m
Nominal Crossline Trace Spacing	0.3 m

1. Time stamp method to obtain a spatial position for each GPR trace.
2. Each data cube was binned for 3D time migration where the bin sizes varied by site.
3. Bandpass filtering with a 25-50-400-800 Ormsby filter to attenuate low frequency transient and high frequency random noise.
4. Time zero correction with first break correlation to remove start of record delay and system drift.
5. Kirchoff 3D time migration.

Velocity models were determined from a 2D multi-offset GPR line collected across the stream within each 3D survey grid (Chapter 3). Velocities for the water saturated

material below the channel bottom ranged from 0.06 to 0.09 m ns^{-1} for the alluvial sites and 0.04 to 0.058 m ns^{-1} for the peat sites indicating a more homogeneous subsurface within the low-energy stream sites. Because the primary objective of this study is to estimate the relative active layer thickness beneath the channel streambeds, only mean velocities for the water-saturated substrate material were used for time migration. A velocity of 0.068 m ns^{-1} was used for migration of the saturated gravel/sand material datasets and 0.056 m ns^{-1} was used to migrate the saturated peat material datasets.

GPR resolution is limited by wavelength which is related to velocity, *v*, and frequency, *f*, through the relation $\lambda = v/f$. Higher frequencies result in smaller wavelengths which are capable of resolving finer features. However, higher frequencies also attenuate more quickly, decreasing the depth of investigation. Thus a tradeoff exists between depth of investigation and resolution potential where, in this case, λ represents the dominant frequency and $\lambda/4$ provides an approximate vertical resolution limit [*Yilmaz*, 2001]. The dominate frequency of our signal was ~120 MHz due to antenna loading; with a velocity in water-saturated peat of 0.056 m ns^{-1} the signal wavelength is 0.47 m and the vertical resolution limits are roughly ± 0.06 m, meaning that objects separated by less than this distance cannot be individually identified. A velocity of 0.068 m ns^{-1} in water-saturated gravel provides a signal wavelength of 0.57 m with a vertical resolution limit of ± 0.07 m.

Uncertainty in interpreted depths to the thaw/permafrost interface is linked to uncertainties in the velocity model and wavelength resolution. Depths, D_{est}, are estimated

using the two-way travel equation, $D_{est} = \frac{tv}{2}$, where *t* is the one-way travel time, ns, to the reflector and *v* is the velocity, m ns^{-1}. We estimated depth uncertainty by

$$\sigma_D^2 = \left[\left(\frac{\sigma_v}{V_m} D_{est} \right)^2 + \left(\frac{\lambda_d}{4} \right)^2 \right], \quad (4.1)$$

where σ_v is the velocity model standard deviation, V_m is the mean velocity value used to calculate the depth, D_{est} (where $V_m \approx v$), λ_d is the dominate wavelength and $\lambda_d / 4$ provides an approximate vertical resolution limit [*Yilmaz*, 2001].

4.4 Field Examples

The first study area (8I) is located along the inlet stream to I-8 Lake (Figure 4.2). This site represents the high-energy environment with a cobble/gravel streambed. The survey grid spanned across two pool areas (~0.8 m deep) and a riffle section located at the upstream section of the grid (25 m x 11 m) (Figure 4.3). Also worth noting is the presence of a gravel bar which resides along the left side stream bank of the survey area.

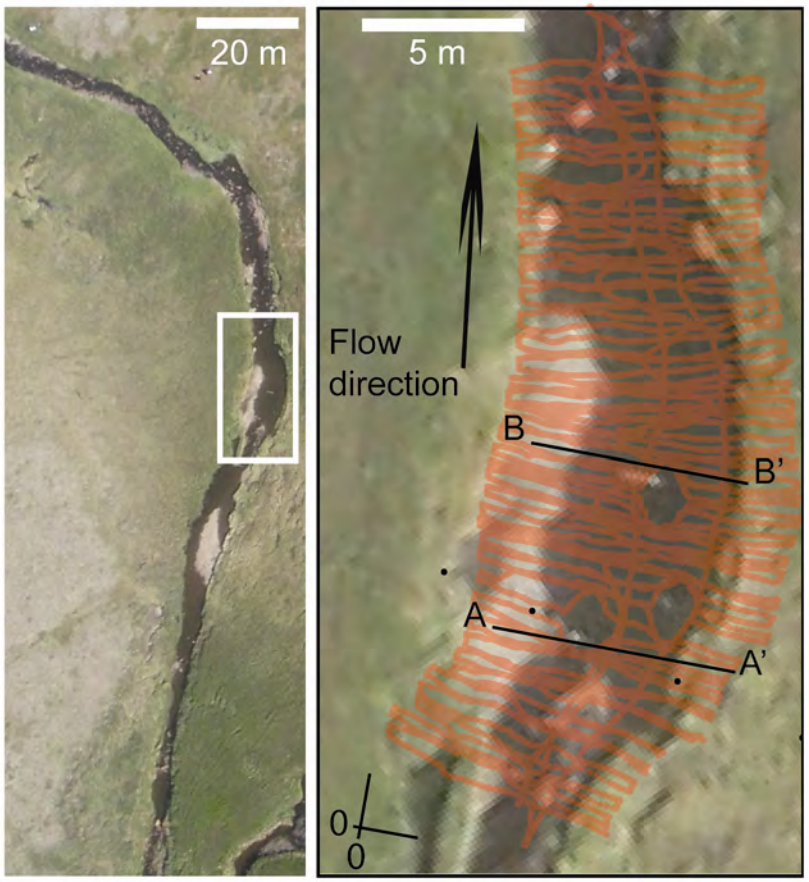

Figure 4.3. Aerial view of study site with GPR (orange) lines. The three holes within the dataset represent areas where either a capacitance rod or nested piezometers resided for data acquisition related to collaborative studies at this site. Zero/zero crosshair (lower left-hand side) indicates approximate location of the zero inline/crossline for the 3D dataset volume. (●) location of multi-offset GPR transect, (▬) location of inline transects shown in Figure 4.4 (a) and (b).

Within the 8I site, velocity estimates from the multi-offset data illustrated a high degree of variation, laterally and vertically across the stream site (Chapter 3) indicating likely velocity variations throughout the data volume. A velocity value of 0.068 m ns^{-1} may oversimplify true velocity variations within the 8I data volume but the migrated results collapsed the majority of the diffractions and improved reflector spatial coherence. Interpreted thaw thickness varied throughout the data volume where maximum thickness

up to 2.3 ± 0.38 m coincided with the riffle section and gravel bar located on the left side stream bank (Figure 4.4a and d). Thinner thaw thickness occurred beneath the pool areas where maximum thickness ranged up to 1 ± 0.21 m (Figure 4.4b-d).

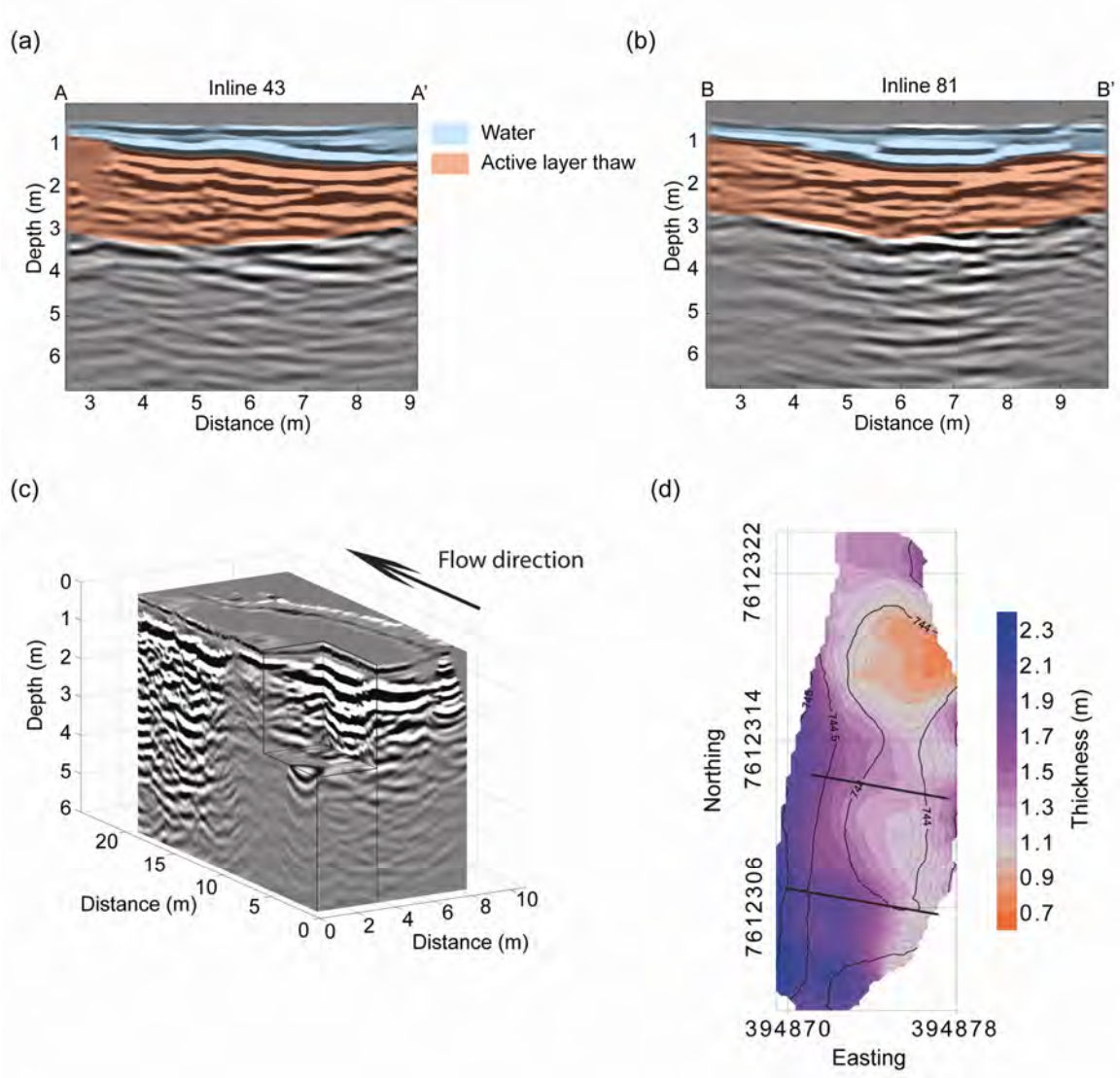

Figure 4.4. (a) Transect inline from 3D GPR survey with interpreted water and thaw depths. (b) Transect inline from 3D GPR dataset with interpreted water and thaw depths. (c) Chair display of 3D GPR survey sliced along the inline B - B' transect. (d) Interpreted seasonal thaw thickness (filled contours) from the 3D GPR dataset with water bottom contours (black) overlain where greatest thaw thickness coincides with the riffle and gravel bar areas. (—) location of inline transects shown in (a) and (b).

The Peat Inlet (PI) is the second study site and is an incised beaded stream with large, deep pools (12 m wide, up to 3 m deep) connected by relatively deep channels (1.5 m deep) (Figure 4.2). This site is a low-energy water flow environment with a peat-lined streambed. The survey spanned across a channel section, through a narrow pool, across another short channel section, and then into a deep large pool where cobbles/boulders were noted along the bottom of the last pool (16 m x 34 m) (Figure 4.5).

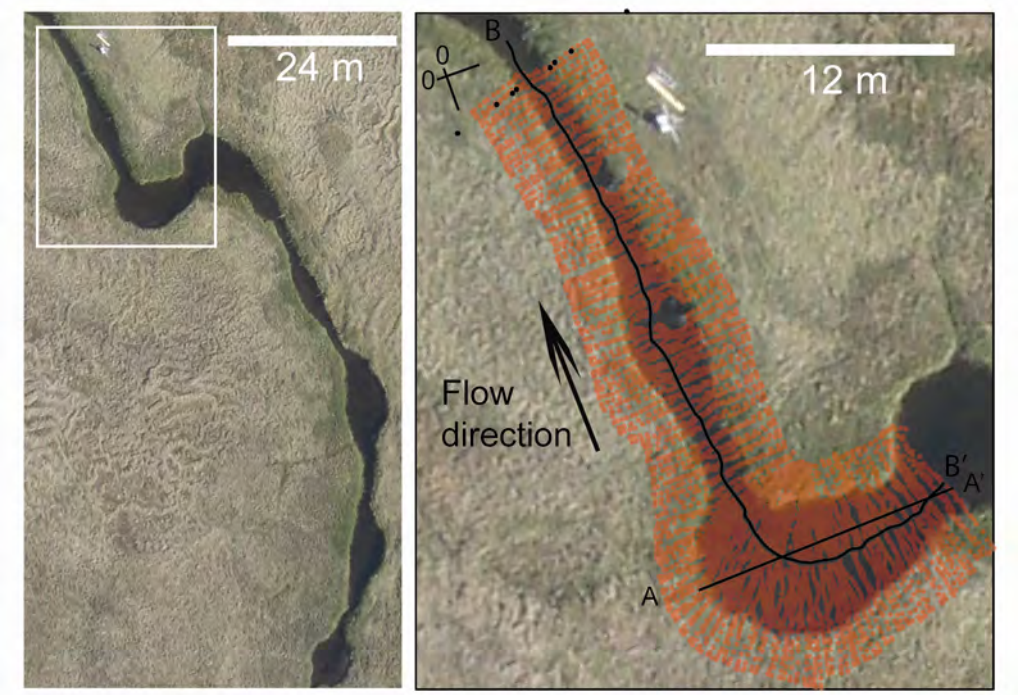

Figure 4.5. Aerial view of study site with GPR (orange) lines. Zero/zero crosshair (upper left-hand side) indicates approximate location of the zero inline/crossline for the 3D datasets over the stream and gravel bar. (●) location of multi-offset GPR transect, (▬) location of transects illustrated in Figure 4.7 (a) and (b).

Radar velocity variations within the PI site were much smaller than the 8I site with a mean velocity of 0.056 ± 0.002 m ns^{-1}. In this case the mean velocity is likely resulting in a more accurate depth estimate than at the alluvial site. The water bottom reflector at

this site was much less obvious due a gradational transition from channel water to saturated peat causing a smaller permittivity contrast between the two zones. Seasonal thaw thickness at the PI site was greatest beneath the pool areas with a maximum thickness up to 1.5 ± 0.13 m (Figure 4.6 and Figure 4.7). The narrow channel connectors coincide with shallower thaw up to 0.9 ± 0.12 m (Figure 4.6 and Figure 4.7).

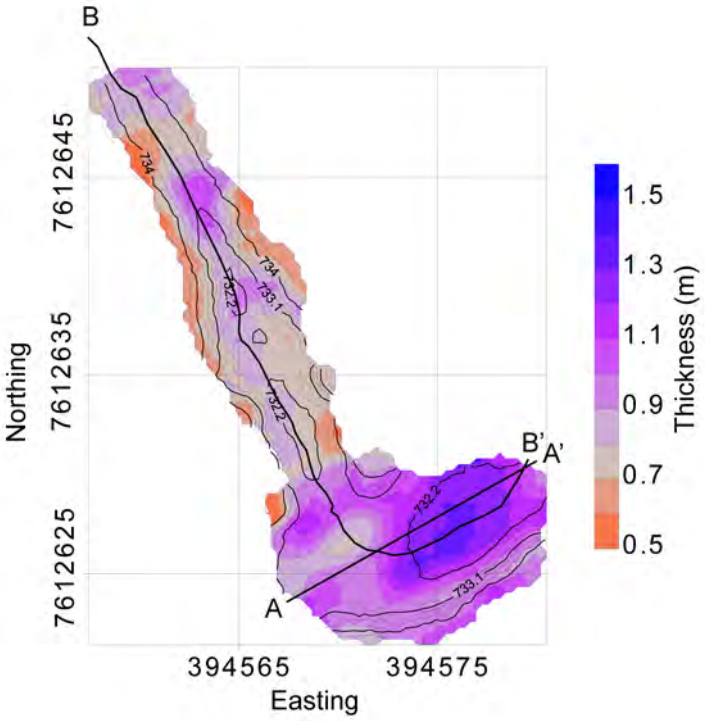

Figure 4.6. Interpreted seasonal thaw thickness (filled contours) from the 3D GPR datasets with water bottom and the surface gravel bar contours (black) overlain where maximum thaw thickness coincide with the deepest pool area. (—) location of transects illustrated in Figure 4.7 (a) and (b).

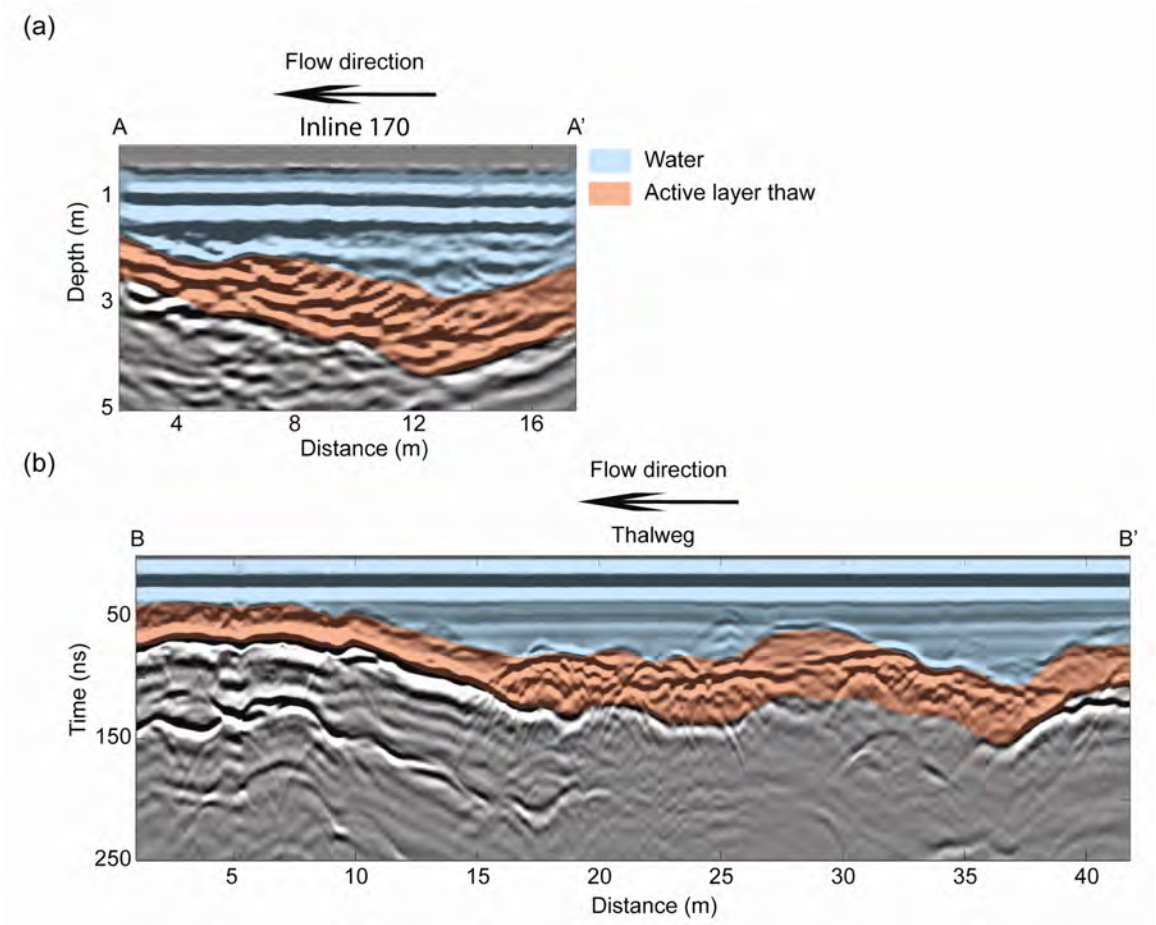

Figure 4.7. (a) Crossline transect from 3D GPR dataset with interpreted water and thaw depths. (b) Unmigrated thalweg transect with interpreted water and thaw depths.

The last site (GC) is located along the stream right channel flowing into a confluence upstream of Green Cabin Lake and represents a mix of the low-energy/high-energy environments that characterize the first two study sites (Figure 4.2). The 3D survey spanned across two large pools (up to 2 m deep) connected by a shallow channel (less than 0.5 m deep) for a total grid survey area of 12 m x 30 m (Figure 4.8). The upstream pool has a peat-lined stream bottom and the downstream pool is gravel-lined. A large gravel bar is located just above the confluence point of the two streams and acts as a topographic barrier, during low flow, for the stream right channel. At the time of the

survey in August 2005 the entire stream right channel flow transitioned from surface channel to subsurface flow through the gravel bar, at the stream channel/gravel bar boundary (see photo of GC site in Figure 4.2), and reappeared along the downstream end of the gravel bar where it merged with surface water in the gravel-lined, stream left channel. An additional 3D survey was conducted across the gravel bar (17 m x 22 m) to measure the thaw depths influenced from the evident subsurface flow.

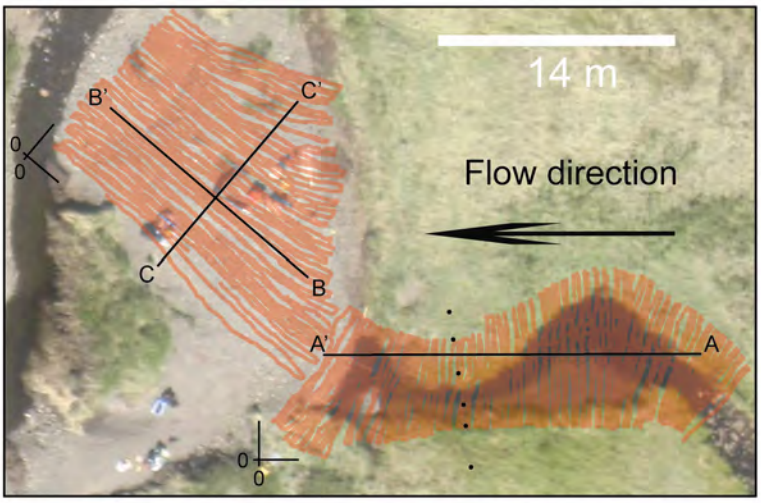

Figure 4.8. Aerial view of study site with GPR (orange) lines. Zero/zero crosshair (lower left-hand side) indicates approximate location of the zero inline/crossline for the 3D datasets over the stream and gravel bar. (●) location of multi-offset GPR transect, (▬) location of transects illustrated in Figure 4.9 (a), (b), and (c) sliced from the 3D dataset volumes.

Results from the GC site illustrate thaw thicknesses resulting from a combination of thermal processes which occur within both 8I and PI sites. A strong reflector representing the thaw/permafrost boundary was evident within both dataset volumes. Maximum thaw thickness within the stream section occurred beneath the pools with thickness values up to 2 ± 0.17 m (Figure 4.9a and Figure 4.10). Thaw thickness under

the gravel bar ranged up to 2.9 ± 0.47 m and is the subsurface zone with the greatest amount of seasonal thaw we have observed in tundra streams around Toolik (Figure 4.9b-c and Figure 4.10).

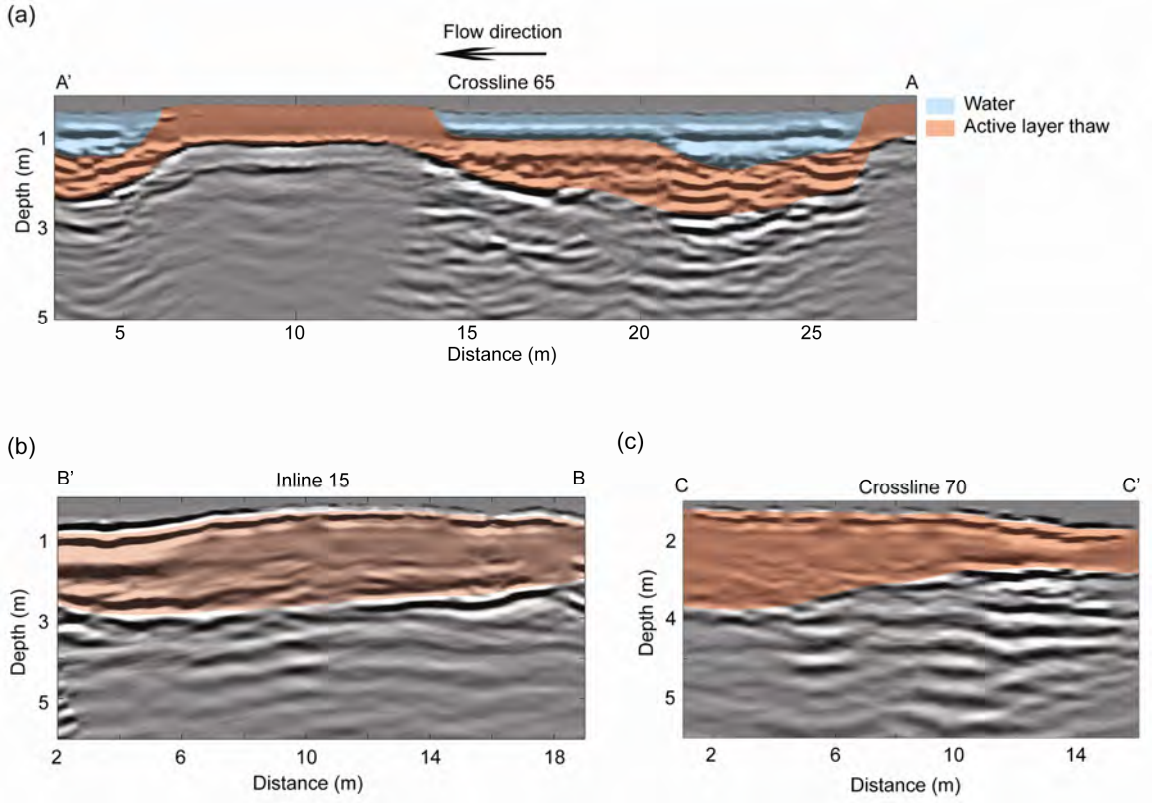

Figure 4.9. (a) Crossline transect from stream 3D GPR dataset with interpreted water and thaw depths. (b) Inline transect from gravel bar 3D GPR dataset with interpreted thaw depth. (c) Crossline transect from gravel bar 3D GPR dataset with interpreted thaw depth.

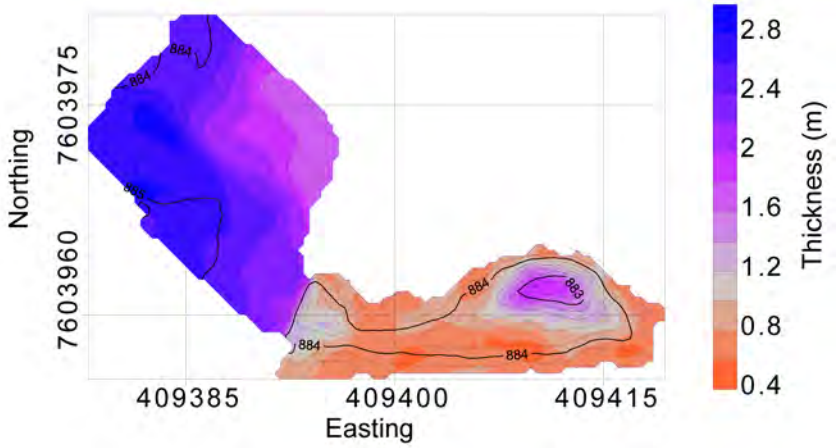

Figure 4.10. Interpreted seasonal thaw thickness (filled contours) from the 3D GPR datasets with water bottom and the surface gravel bar contours (black) overlain where maximum thaw thickness occurring over the gravel bar area.

4.5 Discussion and Conclusions

Results from the three study sites illustrate detailed 3D GPR interpretations of seasonal thaw thickness as it varies with changing streambed features. Within the high-energy site (8I) maximum thaw occurred beneath the riffle and gravel bar features. Deeper thaw within these areas is likely a response to heating of the exposed rock from solar radiation, conduction processes transferring heat downward from varying summer temperatures, and heat convection occurring from subsurface water flow. These processes also take place within the gravel bar at the GC site where the thermal response from radiation and convection is maximized from exposed rocks and the large hydraulic head gradient across the gravel bar resulting in maximum thaw thicknesses up to almost 3 m. Less seasonal thaw takes place under the pool regions likely due to a shallower water convection zone as well as greater water depths resulting in less thermal radiation

occurring beneath pool areas. Influence from convective processes within 8I is supported by solute injection experiment results where horizontal hydraulic conductivity values beneath pools were almost an order of magnitude smaller than the adjacent upstream riffle tails [*Zarnetske et al.*, 2008].

Thaw depths within the low-energy stream sites at PI and GC are primarily controlled by likely heat conduction processes where peat material has a low hydraulic conductivity and radiation is absorbed and carried away by greater, continuous channel water flow throughout the summer. Within the pool regions where thaw depths progress up to 2 m we propose the existence of a talik (a thawed region within the subsurface which remains thawed year around) that persists due to the insulating properties of the low-energy stream environments. Because of the water depth and associated insulation, little or no freezing may occur at the base of the deeper pools allowing for talik formation and persistence over several seasons resulting in greater maximum thaw depth.

Results from the three study sites help resolve problems that plagued GPR interpretations of the seasonal thaw/permafrost boundary in an earlier study [*Brosten et al.*, 2006] that included 3D point source diffractions. The 3D datasets provided the necessary information to collapse diffractions to the proper point source location after migration. New challenges arose from migration artifacts occurring along the boundaries of the 3D volume in addition to strong water bottom multiples, within the gravel-lined stream site (8I), causing difficulties in locating the proper reflector representative of the thaw/permafrost boundary.

This chapter has illustrated the use of 3D GPR within arctic stream environments. Results provide detailed maps of seasonal thaw thickness between two different stream environments where maximum thaws occur beneath opposing stream features (i.e. beneath riffles in the gravel-lined streams and pools in the peat-lined streams) likely due to very different thermal processes. Detailed thaw depth geometry provided by the 3D GPR surveys can be used to inform and significantly improve 3D groundwater flow and particle tracking models by constraining the model domain in 3D space and, in turn, reducing the uncertainty associated with hyporheic zone transport processes.

5 MODELING THERMAL PROCESSES BENEATH ARCTIC STREAMS ON THE NORTH SLOPE, AK

5.1 Abstract

Seasonal thaw depth beneath arctic streams significantly impacts physical and biological processes within arctic stream environments. To better understand the influence from thermal conduction on active layer thaw we developed, using the finite-difference method, a one-dimensional, heat transport model with phase change to estimate seasonal temperatures beneath two arctic stream types; a high-energy gravel-dominated stream and a low-energy peat-bedded stream. The model was driven by stream water or near-surface temperature data recorded at selected stream sites near Toolik Field Station, AK, for the summer months of 2004 and 2005. Model temperatures were calibrated to measured temperatures at corresponding depths and evaluated against interpreted thaw depths from cross-sectional ground-penetrating radar (GPR) images gathered over the 2004 summer season. Model temperatures were in reasonable agreement with observed temperatures and GPR thaw depth estimates. However, temperature variations between model and observed values increased with depth. The variations are likely due to a homogenous soil property assumption, oversimplification of convection processes, and deviations from the 1D model.

5.2 Introduction

Biological and physical processes that take place within arctic streams are strongly affected by the duration and extent of the active layer which resides beneath, and adjacent to, the stream channel and above the permafrost table. This area of active layer thaw is defined as the thaw bulb and has been shown to extend to greater depths than the surrounding terrestrial active layer thaw [*Brosten et al.*, 2006]. The movement of stream water flowing into the near subsurface and back out to the stream channel is known as hyporheic exchange flow and occurs within the upper portion of the thaw bulb (Figure 5.1). The extent of this exchange defines the hyporheic zone and is where nutrient cycling takes place.

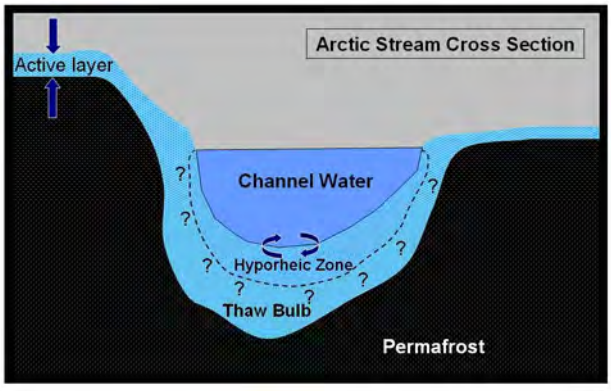

Figure 5.1. The extent of the hyporheic zone is defined as the area where channel water and subsurface water mix. In arctic streams the hyporheic zone exists within the seasonal thaw layer, defined as the thaw bulb beneath the streams [*Greenwald et al.*, 2008].

A preliminary study of seasonal thaw beneath arctic streams hypothesized that the thaw bulb may control hyporheic zone hydrology [*Bradford et al.*, 2005]. Time-lapse results illustrated rapid thaw bulb development, up to 1 m within the first week of June

2004, beneath gravel-lined stream sites and a slower more progressive thaw beneath the peat-lined sites [*Brosten et al.*, 2006]. Hydrologic and water chemistry results concluded that influence from seasonal thaw depth on hyporheic flow processes is minimal [*Greenwald et al.*, 2008; *Zarnetske et al.*, 2007] and that the hyporheic zone is influenced by depth of thaw only up to a threshold depth, which is controlled by hydraulic head gradients imposed by stream morphology [*Zarnetske et al.*, 2008].

These previous studies concluded that the depth of thaw does not influence hyporheic flow. In this study we approach the problem from another direction and attempt to determine if hyporheic flow affects the depth of thaw. The time-lapse study established that the seasonal thaw beneath arctic streams occurs at greater depths compared to the adjacent terrestrial tundra and thaw beneath gravel-lined streams progresses much quicker with deeper maximum thaw depths than the peat-lined streams [*Brosten et al.*, 2006]. Both scenarios suggest that hyporheic flow may be contributing to thaw bulb growth. A finite-difference, one-dimensional (1D), heat transport model with phase change was used to model seasonal thaw bulb temperatures. To determine if advected heat from hyporheic flow contributes to thaw bulb growth we added a simplified term to represent heat transfer from advection resulting in an enhanced conduction model. Model results from the conduction (conduction only) and enhanced conduction (conduction plus convection) are compared to determine influence of thaw from thermal conduction and advection processes.

There are an extensive number of published studies that have investigated and monitored thermal processes and properties within the terrestrial arctic active layer and

permafrost through modeling and temperature measurements [*Goodrich,* 1982; *Kane et al.*, 1991; *Osterkamp and Romanovsky*, 1996; 1997; *Romanovsky and Osterkamp*, 1995; 2000; *Woo and Xia*, 1996; *Zhang et al.*, 1996; *Zhang and Stamnes*, 1998]. Romanovsky and Osterkamp [1997] studied the thermal processes in the active layer and near-surface permafrost during seasonal thawing. Subsurface temperature data were used to calibrate a 1D finite element conductive heat flow model with a moving phase boundary [*Osterkamp and Gosink,* 1991; *Osterkamp and Romanovsky,* 1996] which was then used to simulate the seasonal thawing in the active layer and near-surface permafrost. Results indicated that unfrozen water content had a significant affect on temporal variations in thermal conductivities. Therefore, a conduction model could accurately predict thaw depths provided that the properly averaged thermal properties were used. Another study conducted by Zhang and Stamnes [1998] concluded air temperature as the most important parameter controlling soil temperatures.

Few studies have investigated thermal processes beneath arctic streams, likely due to logistical complications, and can provide valuable information for ecological impacts on the hydrological and biological environments as climate changes. Wankiewicz [1982] studied thermal processes of a river talik beneath two arctic rivers through modeling measured subsurface temperatures in April, August, and November 1977-1978. Wankiewicz [1982] concluded that conduction dominated heat transfer process at one site while macrodispersion of heat from ground water flow was the dominate process at the second site.

We present continuous subsurface temperature data recorded over the 2004-05 summer months at three stream sites on the North Slope, AK, for comparison to seasonal time-lapse GPR transects, gathered in 2004, by employing a 1D conductive heat transfer model with phase change to determine the amount of thaw caused by thermal conduction processes. In addition, effects from advection were investigated with an enhanced conduction term. Observed stream water temperatures or near-surface temperatures were used to drive the model to predict active layer seasonal thaw from early June to mid-October 2004 and mid-May to mid-October 2005. Modeled temperature results were compared and validated against estimated thaw depths interpreted from common-offset GPR transects gathered across two of the stream sites over the 2004 summer season. Models were calibrated to observed temperatures ranging down to depths of 1.6 m. Additionally, multi-offset GPR transects, gathered in 2005, provided water content estimates for the thermal models.

5.3 Field Sites

Study sites are located ~1 km south of Toolik Field Station on the North Slope, AK (Figure 5.2). The stream sites encompassed two general geomorphologic conditions found in rivers and streams on Alaska's North Slope; 1) low-energy water flow, organic material lining, beaded morphology, 0.03% gradient, and 2) high-energy water flow, riffle-pool-riffle morphology, cobble to gravel material lining, 0.70% gradient. The Peat Inlet (PI) site represents the low-energy water flow environment and is characterized by large, deep pools (12 m wide, 2.5 m deep) connected by shallow narrow channels (2.5 m

wide, 1 m deep). The next two sites represent the high-energy environment with one site located on the inlet stream to I-8 lake (I8) and the second site located downstream of the lake (8O). These two sites were selected to study the lake effect on thermal processes within the thaw bulb environment.

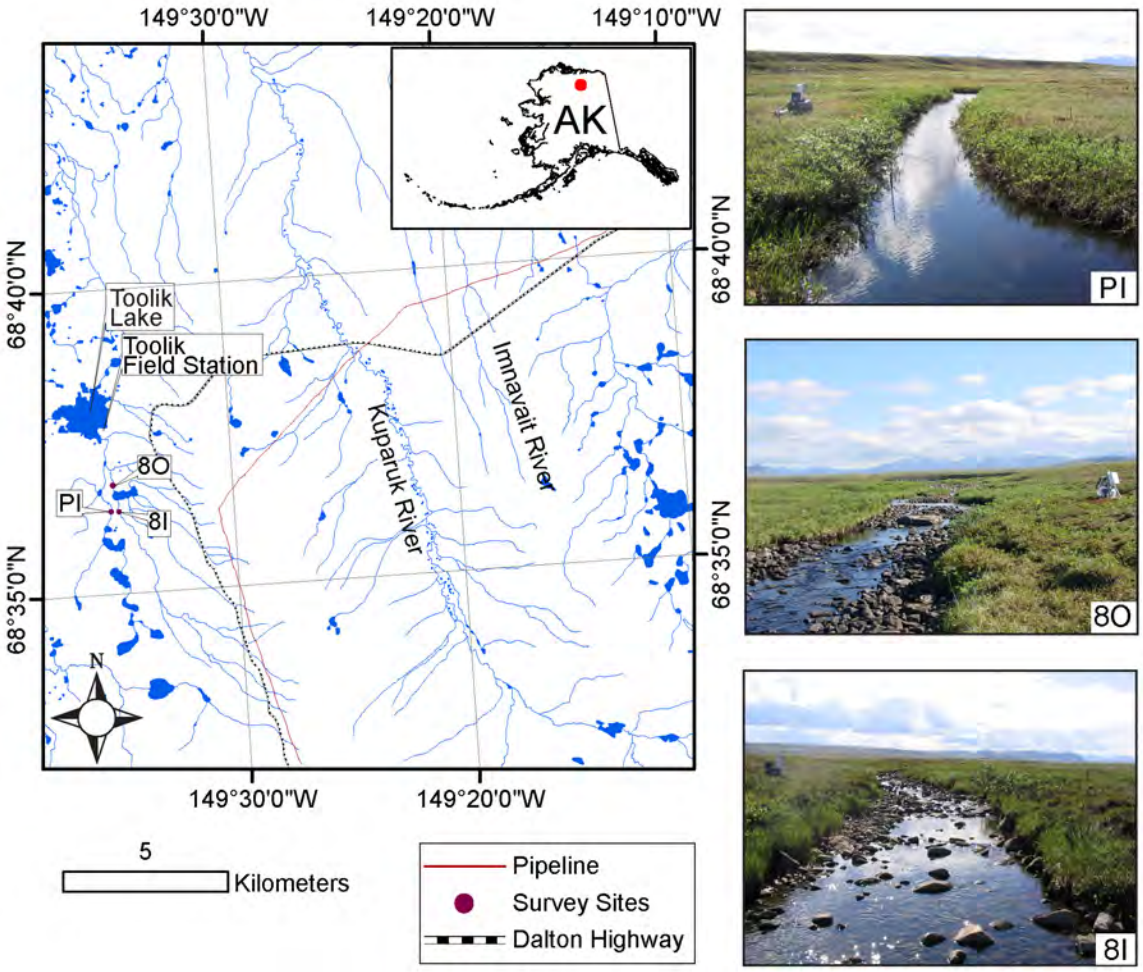

Figure 5.2. Locations and photos of the three thermocouple instrumentation study sites (8I, 8O, and PI) within the Kuparuk watershed, AK.

5.4 Methods

5.4.1 Heat Transfer Model

An explicit 1D heat conduction model was developed, using the finite-difference method, to investigate seasonal thaw beneath arctic streams. It is well established that unfrozen water can strongly influence heat and mass transport processes in soils [*Harlan*, 1973; *Jame and Norum*, 1980; *Nakano and Brown*, 1972; *Osterkamp*, 1987]. Therefore, an analytical approach was incorporated into the conduction model to account for the effects of unfrozen water on thermal properties [*Osterkamp*, 1987] (see Appendix C for details).

Assuming that unfrozen water does not move within permafrost then the 1D heat transport equation is

$$C\frac{\partial T}{\partial t} = \frac{\partial}{\partial z}\left(K\frac{\partial T}{\partial z}\right) \tag{5.1}$$

where T is the soil temperature (˚C), K is thermal conductivity (W m^{-1}˚C^{-1}), and C is the apparent volumetric heat capacity (MJ m^{-3}˚C^{-1}). The difference in density between ice and unfrozen water are neglected except in the latent heat term where it is incorporated into the apparent volumetric heat capacity,

$$C = C_v - L\left(\frac{\rho_i}{\rho_u}\right)\frac{\partial \theta_i}{\partial T}, \tag{5.2}$$

where C_v is the volumetric heat capacity (MJ m^{-3}˚C^{-1}), L is the volumetric latent heat of fusion for ice (J m^{-3}), ρ_i and ρ_u are the densities for ice and unfrozen water respectively, and θ_i is the volumetric ice content. Assuming that ρ_i and ρ_u are independent of

temperature then equation (5.2) can be expressed in term of volumetric unfrozen water content θ_u,

$$C = C_v - L\frac{\partial \theta_u}{\partial T}. \tag{5.3}$$

The unfrozen water content of a partially frozen soil or permafrost is represented by a power law where,

$$\theta_u = \left(\frac{\rho_b}{\rho_u}\right) a|T|^b, \tag{5.4}$$

ρ_b is the dry bulk density of the partially frozen soil or permafrost, a and b are empirically derived material-dependent constants [*Anderson et al.*, 1973; *Tice et al.*, 1981].

Temperature measurements recorded by thermocouples placed within the stream channel water or near surface defined the upper, driving, boundary for the model. The lower boundary was set at 30 m depth to ensure no significant effects on thermal processes at shallow depths. A constant geothermal heat flux of 0.0565 W m^{-2} [*Lachenbruch et al.*, 1982] was set at the lower boundary. Model stability is maintained while the Fourier number, *Fo*, [*Incropera and DeWitt*, 2002] remains at or below 0.5,

$$Fo = \frac{D_i \Delta t}{(\Delta z)^2} \leq \frac{1}{2}, \tag{5.5}$$

where D_i is the thermal diffusivity, Δz is the depth step ranging from 0.01 to 1 m and, Δt is the time step increment set at 1 minute.

Thermal diffusivity,

$$D_i = \frac{K_i}{C_i}, \tag{5.6}$$

is determined from the thermal conductivity, K_i, and apparent volumetric heat capacity, C_i, for the *i*th layer (Appendix C). Substitute equation (5.6) into (5.1) and the heat equation becomes

$$D_i \frac{\partial^2 T_i}{\partial z^2} = \frac{\partial T_i}{\partial t}, \tag{5.7}$$

for the *i*th layer. The 1D explicit form of the finite difference equation is

$$T_z^t = Fo\left(T_{z+1}^t + T_{z-1}^t\right) + \left(1 - 2Fo\right)T_z^t. \tag{5.8}$$

Measured temperatures on June 1, 2004 and May 15, 2005 were used as the initial temperature conditions. Temperatures for the remaining grid cells past the last measured temperature cell were extrapolated to the bottom boundary with an exponential decay to -7.95 ˚C (Figure 5.3) and represents the mean permafrost temperature measured from 1983 to 2001 at 30 m depth, Deadhorse, AK [*Osterkamp*, 2003].

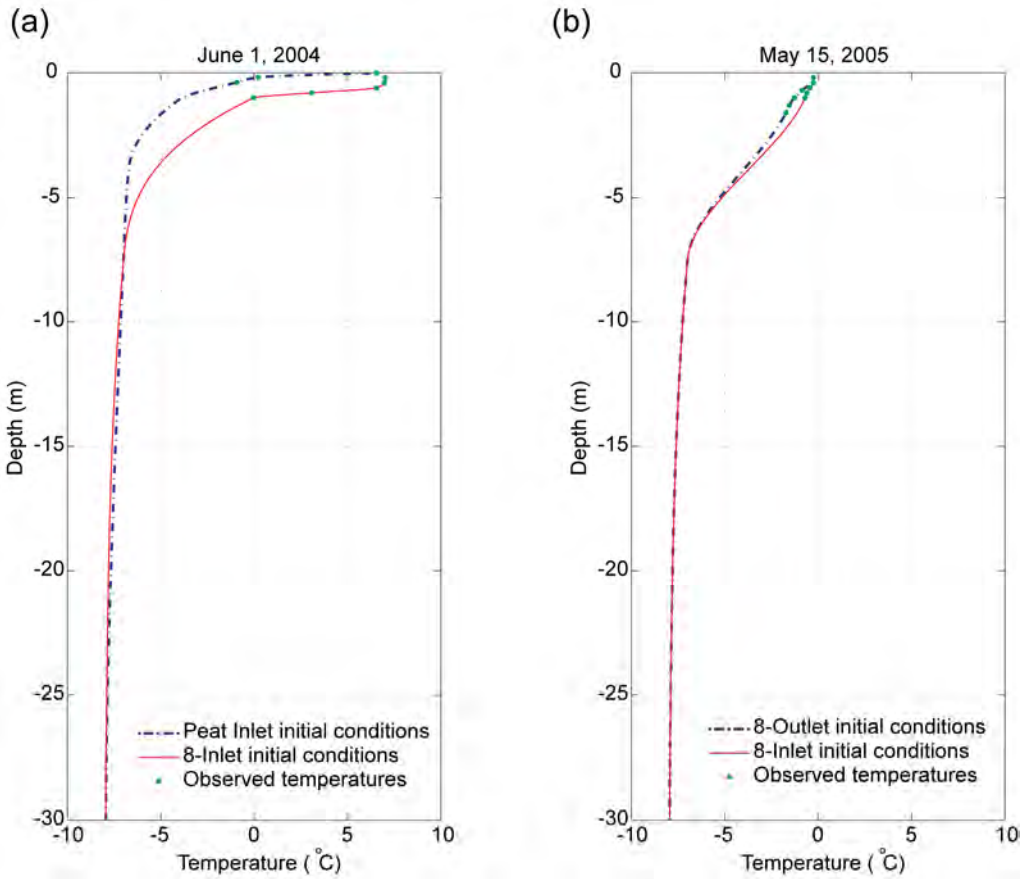

Figure 5.3. Temperature profiles of initial conditions for study sites. (a) 2004 initial conditions for 8I and PI sites with observed temperatures noted. (b) 2005 initial conditions for 8I and 8O sites with observed temperatures noted.

To account for advective heat transfer from hyporheic flow within the gravel-lined sites an additional heat transport term, in the vertical direction, was added where equation (5.1) becomes

$$C\frac{\partial T}{\partial t} = \frac{\partial}{\partial z}\left(K_e \frac{\partial T}{\partial z}\right) \tag{5.9}$$

and K_e is the effective conductivity defined as the sum of conduction and advection given by [*Wankiewicz*, 1982]

$$K_e = K + C_u \gamma_T K_h S\,. \tag{5.10}$$

The advection term is the product of the volumetric heat capacity for water (MJ $m^{-3}°C^{-1}$), C_u, transverse dispersivity (m), γ_T, hydraulic conductivity (m s^{-1}), K_h, and channel slope, S. In advective flows the thermal diffusivity, D, and kinematic viscosity, ν, are approximately equal,

$$D \approx \nu = \frac{\mu}{\rho}, \tag{5.11}$$

where μ is the dynamic viscosity and ρ is the fluid density. The advection term in equation 5.10 enhances the transport of heat vertically resulting in greater diffusivity values within the hyporheic flow region. In a 1D model this is a reasonable approach to account for additional heat input from advective processes. A positive transverse dispersivity term (in the vertical direction) is used to simulate maximum thaw scenarios while lateral dispersivity is assumed to be negligible.

Studies conducted by Zarnetske et al. [2008] observed hyporheic flow up to ~1 m depths; therefore, the effective conductivity term is assumed to reside within the upper first meter where its influence exponentially decreases to zero at the one meter depth cell. Due to the shallow hyporheic flow depths noted by Zarnetske et al. [2008] heat addition from subsurface water flow beneath the PI stream is assumed to be negligible and therefore not modeled.

One soil type with corresponding physical and thermal properties was assumed for each model. Table 5.1 provides a summary of the range of soil thermal and physical properties published in previous studies [*Hinzman et al.*, 1991; *Kane et al.*, 1991; *Lachenbruch et al.*, 1982; *Osterkamp and Romanovsky*, 1997; *Romanovsky and*

Osterkamp, 1997; *Williams and Smith,* 1989] where peat values were used for the PI site model and silt to gravel properties were used for the 8I and 8O models. Calibration of the models included selecting reasonable density and thermal conductivity values, based on past studies, which minimized differences between calculated and observed temperature profiles through trial and error model runs. Volumetric water content estimates were obtained from multi-offset GPR images gathered at or near the thermocouple sites in August 2005 (Chapter 3) using the pertrophysical relationship defined by the Topp equation [*Topp et al.*, 1980]. Hydraulic conductivity and slope values for 8I were acquired from field measurements gathered in 2005 upstream ~100 m from the 8I temperature site [*Zarnetske et al.*, 2007; *Zarnetske et al.*, 2008]. The same values were used at the 8O site with the assumption that differences in slope and hydraulic conductivity values between the two sites is negligible. Transverse dispersivity values reported by Pickens and Grisak [1981] ranged from 0.20 to 9.2 m where a positive value of 0.23 m were used for the 8I and 8O temperature models to simulate maximum thaw.

Table 5.1. Physical and Thermal Properties of the Active Layer and Near-Permafrost Soils Determined from Past Studies Where Subscripts *t* and *f* Represent Thawed and Frozen Soils with Their Corresponding Range of Values for Thermal Conductivity, Volumetric Heat Capacity, and Thermal Diffusivity.

Soil type	Density (kg m^{-3})	Volumetric water content θ (%)	Thermal conductivity K_t/K_f (W m^{-1} K^{-1})	Volumetric heat capacity C_t/C_f (MJ m^{-3} K^{-1})	Thermal diffusivity D_t/D_f (m^2 d^{-1})
peat	270-1100	35-88	0.3-0.6/0.5-1.7	2.6-3.0/1.26-2.4	0.01-0.02/0.07-0.08
silt	1100-2000	25-55	0.9-1.35/1.56-2.2	1.9-3.1/1.5-2.0	0.03-0.04/0.08-0.09
sand	1400-2000	40	2.2/--	1.48/--	0.05-0.06/0.01
sand/gravel	1620	38.9	2.0/3.39	2.9/1.95-2.04	--/--
gravel	1400-2000	--	--/3.59	--/1.54	0.05-0.06/0.14-0.09

Predicted temperatures were compared to observed temperatures at each study site for validation. An uncertainty analysis of the modeled temperatures, σ_T^2, was calculated by varying parameters independent of temperature which included soil thermal conductivity, soil density, and porosity, in addition to hydraulic conductivity, transverse dispersivity, and slope included for the enhanced conduction models,

$$\sigma_T^2 = \left[\left(\frac{\partial T}{\partial K_s} \sigma_{k_s} \right)^2 + \left(\frac{\partial T}{\partial \rho_s} \sigma_{\rho_s} \right)^2 + \left(\frac{\partial T}{\partial \theta_u} \sigma_{\theta_u} \right)^2 + \left(\frac{\partial T}{\partial K_h} \sigma_{k_h} \right)^2 + \left(\frac{\partial T}{\partial \gamma_T} \sigma_{\gamma_T} \right)^2 + \left(\frac{\partial T}{\partial S} \sigma_S \right)^2 \right], \tag{5.12}$$

where errors for parameter measurements are assumed to be normally distributed.

5.4.2 Temperature Measurements

Temperatures were measured using Type-T thermocouple wire connected to a Campbell Scientific CR10X datalogger and AM16/32 multiplexer using a CR107 reference thermistor. Uncertainty associated with Type-T thermocouples are ±1.0 °C over the range of -65 to 130 °C. Thermocouples were installed in vertical profiles by driving a

steel sleeve and interior bar into the streambed. The bar was then removed and the thermocouples were inserted into the sleeve. Lastly, the sleeve was removed from the sediment and pulled over the thermocouple wire, leaving the thermocouples in place.

We installed four streambed thermocouple strings in 8I (across a riffle section) and two temperature strings in PI (across a deeply incised channel section) at 0.20 m increments to varying depths in late August 2003 (Table 5.2). Two thermocouple strings were installed at the 8O site (across a riffle section), in August 2004 at 0.30 m increments (Table 5.2). Continuous subsurface temperature readings were recorded every four to six hours starting late May 2004, at the 8I and PI sites and August 2004 at the 8O site. Temperature variations for each approximate corresponding depth recorded by neighboring thermocouple strings, installed at each site, was negligible. Therefore, to avoid redundancy only one thermocouple string, from each site, was used for modeling purposes, string (2) for 8I, and string (1) for 8O and PI (Table 5.2). For all sites thermocouples were installed as deep as possible however the method employed limited our ability to install thermocouples past the maximum active layer thaw depth, into the permafrost layer.

Table 5.2. Thermocouple Strings at Depth for Each Study Site.

	Thermocouple String (depth in meters)			
Study site	(1)	(2)	(3)	(4)
8I	0.27	0.20	0.22	0.18
	0.47	0.40	0.42	0.48
	0.67	0.60	0.62	0.68
	0.87	0.80	0.82	0.88
	1.07	1.00	1.02	0.98
PI	0.18	0.16		
	0.38	0.36		
8O	0.40	0.31		
	0.70	0.61		
	1.00	0.91		
	1.30	1.21		
	1.60	1.51		

5.4.3 Ground-Penetrating Radar

Time-lapse GPR transects were gathered across the 8I and PI temperature recording site in 2004 at weekly intervals on June 2, 7, 14, and 22, August 6, and September 19. Maximum thaw depths were interpreted for each transect [*Brosten et al.*, 2006] and are compared to the zero degree isotherm depth estimated by the thermal model. GPR data were acquired using a Sensors and Software PE100A pulsed radar system, 1000V transmitter, and 200 MHz antennas. Also in August 2005 multi-offset GPR profiles were gathered across the 8I stream ~100 m upstream of the temperature site and across the 8O and PI temperature sites [*Brosten et al.*, in review]. The standard deviation from velocity models, derived from the multi-offset transect, in addition to the vertical wavelength resolution determined uncertainty in interpreted thaw depths from the GPR data. The GPR thaw depth uncertainty, σ_D, is defined by

$$\sigma_D^2 = \left[\left(\frac{\sigma_v}{V_m} D_{est} \right)^2 + \left(\frac{\lambda_m}{4} \right)^2 \right] \quad (5.13)$$

where σ_v is the velocity model standard deviation, V_m is the mean velocity value used to calculate the depth, D_{est}. Wavelength is related to velocity, *v*, and frequency, *f*, by $\lambda = v / f$ where λ_m is the mean wavelength and $\lambda_m / 4$ provides an approximate vertical resolution limit meaning that objects separated by less than this distance cannot be individually identified [*Yilmaz*, 2001].

5.5 Results

5.5.1 8I Site

Subsurface temperature measurements at the 8I stream site exhibited a rapid response to seasonal thermal processes for 2004 and 2005 (Figure 5.4 and Figure 5.5) and with a maximum temperature of ~18 ˚C at 0.20 m on July 2, 2004 (Figure 5.4b) and June 30, 2005 (Figure 5.5b). A temperature gradient is apparent during the initial thawing for both summer periods. Starting in July measured temperatures at greater depths (0.60, 0.80, and 1.0 m) inverted periodically with shallower temperatures (0.20 and 0.40 m) throughout the summer months indicate a rapid response to the fluctuating surface temperatures. Daily average temperatures at all depths, for both seasons, were above freezing by late May and cooled to 0 ˚C by late September.

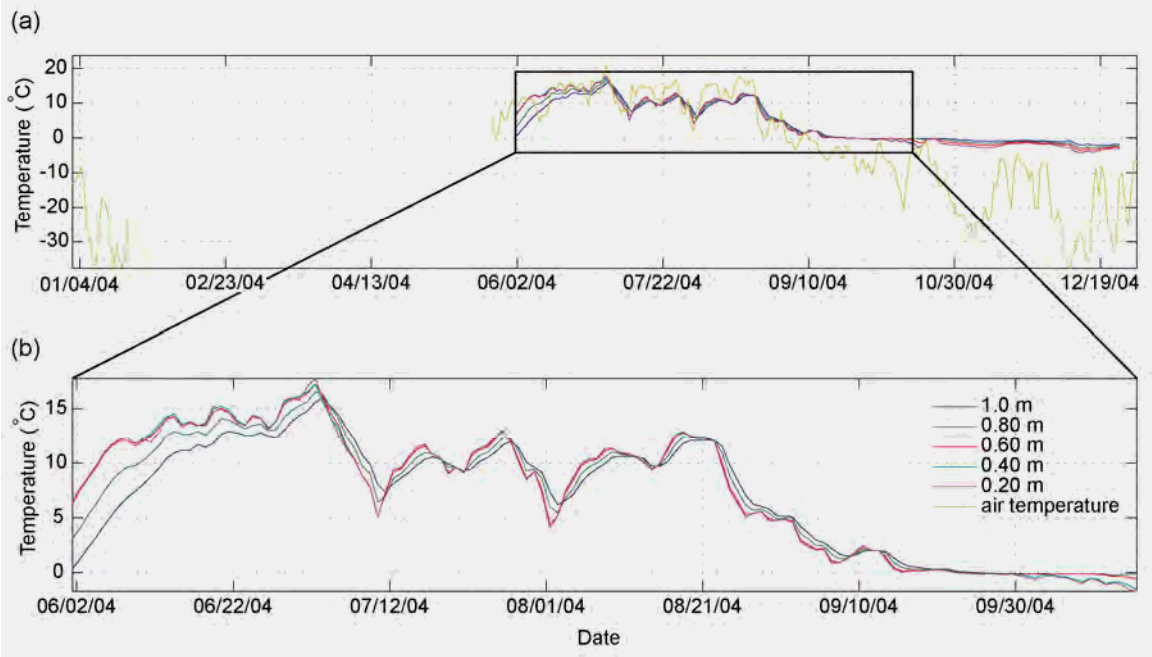

Figure 5.4. Daily average temperature profile recorded at the 8I stream site. (a) Recorded temperatures for 2004 (temperature logging started May 28, 2004) with temperatures measured from 0.20 to 1.0m depth at 0.20m increments. Air temperatures were recorded at the Toolik Field Station Meteorological Station [*Shaver*, 2004]. (b) Subset of the recorded temperatures used for model validation (1 June to 15 October).

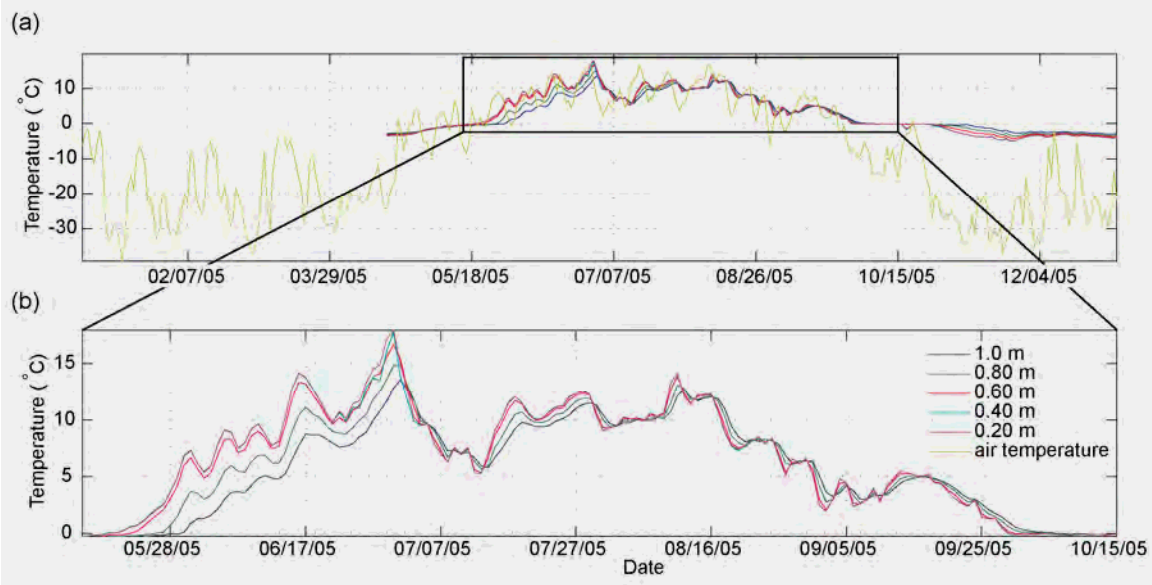

Figure 5.5. Daily average temperature profile recorded at the 8I stream site. (a) Recorded temperatures for 2005 (missing temperature data for the first ~4 months were due to instrument failure) with temperatures measured from 0.20 to 1.0m depth at 0.20m increments. Air temperatures were recorded at the Toolik Field Station Meteorological Station [*Shaver*, 2005]. (b) Subset of the recorded temperatures used for model validation (15 May to 15 October).

Parameter values used for the thermal model include a soil density of 1600 kg m^{-3}, soil thermal conductivity of 2.92 W m^{-1}˚C^{-1}, volumetric water content value of 0.30 (mean value derived from the GPR data), hydraulic conductivity of 1.5×10^{-2} m s^{-1}, and a slope value of 0.7% [*Zarnetske et al.*, 2008]. Predicted temperatures provided by the thermal model for 2004 underestimate observed temperatures at 0.40, 0.60, 0.80, and 1.0 m with differences increasing with depth (Figure 5.6). Maximum temperature differences, between modeled and observed, ranged up to ~6 ˚C in 2004 (Figure 5.6d) and ~5 ˚C in 2005 at the 1.0 m depth interval. Models with the enhanced conduction term for 2004 and 2005 both exhibit a slightly better fit to the observed values by removing the time lag between peaks and troughs within the temperature signature;

however, results from the additional advection term was minimal with less than 1˚C temperature difference, for most days, when compared to results from conduction alone. Therefore, only model results from the 1D conduction model were pursued for further analysis.

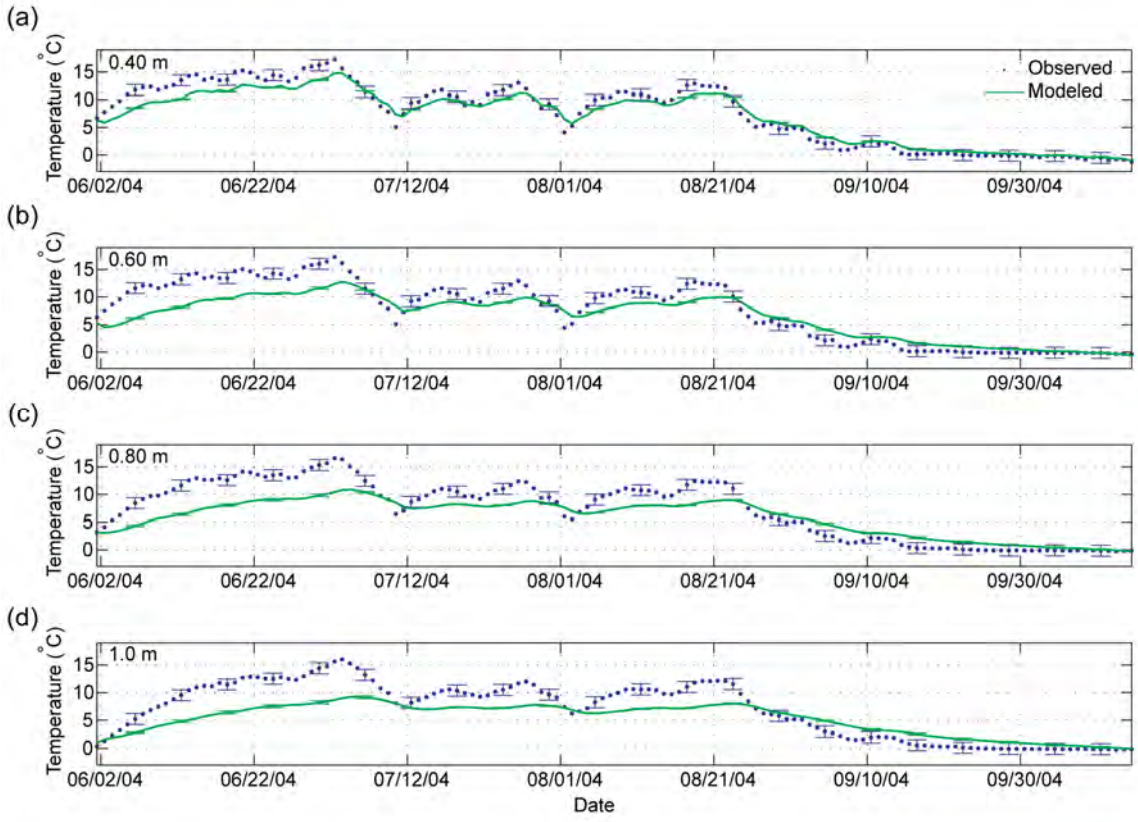

Figure 5.6. Comparison between 2004 daily averaged predicted and observed temperatures at (a) 0.40m; (b) 0.60m; (c) 0.80m; and (d) 1.0m.

The conduction models predicted maximum thaw depths (the zero isotherm) to 3.26 and 3.24 m on September 1, 2004 and, August 30, 2005 respectively (Figure 5.7a and Figure 5.8). Thaw depth estimates interpreted from the 2004 time-lapse GPR profiles ranged from 1.0 m, on June 2, up to 2.0 m on June 22 and are in good agreement

with depths to the 0 ˚C isotherm estimated from the thermal model (Figure 5.7b). The GPR thaw depth estimate for August 6 was 2.4 ± 0.38 m and is shallower compared to the 3.15 ± 0.10 m estimate from the thermal model. The last GPR acquisition on September 19 estimated a maximum thaw depth of 2.0 ± 0.33 m and is ~1 m less than the thermal model with an estimated thaw depth of 3.15 ± 0.05 m (Figure 5.7b).

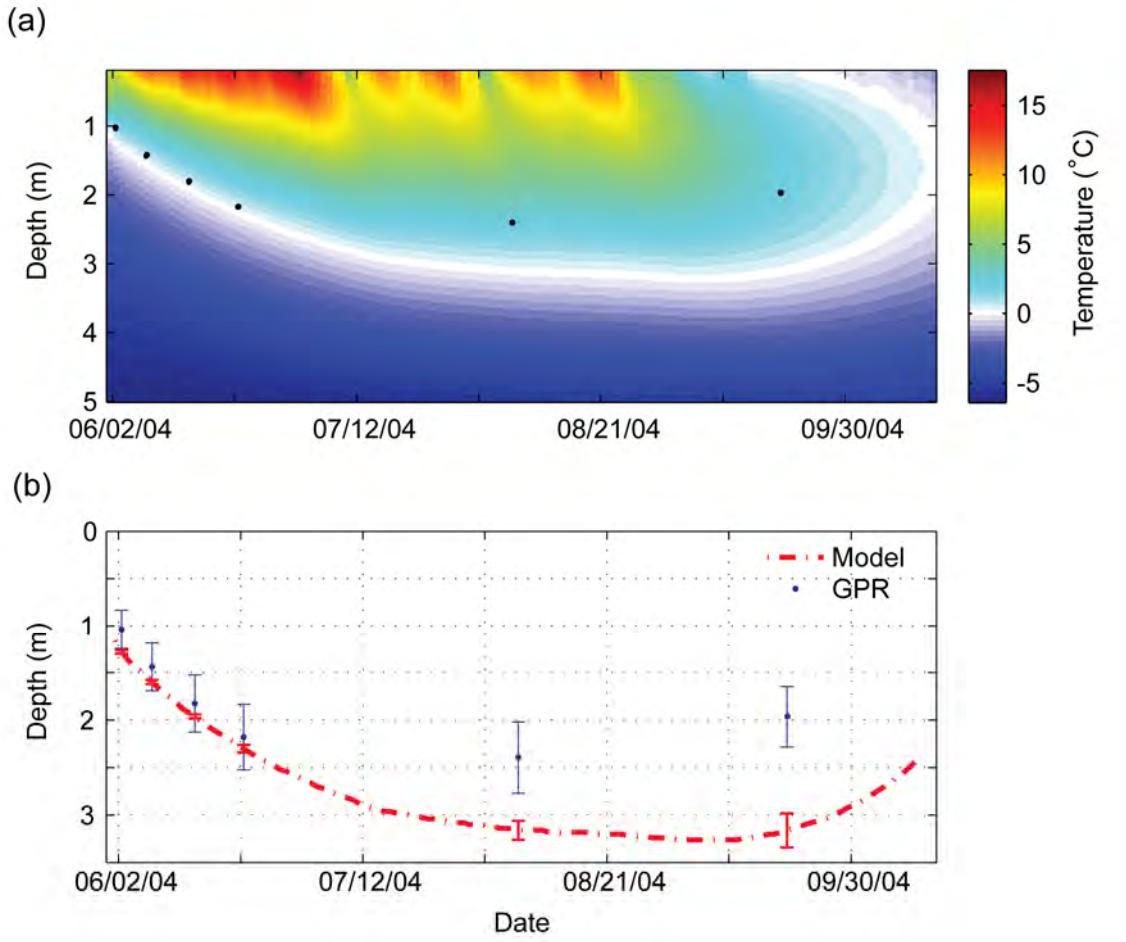

Figure 5.7. Simulated temperature results for 8I 2004. (a) Isotherm plot of modeled temperatures at depth. (●) represents thaw depth estimates from GPR transects collection on June 2, 7, 14, and 22; August 6; and September 19, 2004. (b) Comparison between the zero degree isotherm estimated from the thermal model, at depth, and estimated maximum thaw depths from GPR transects.

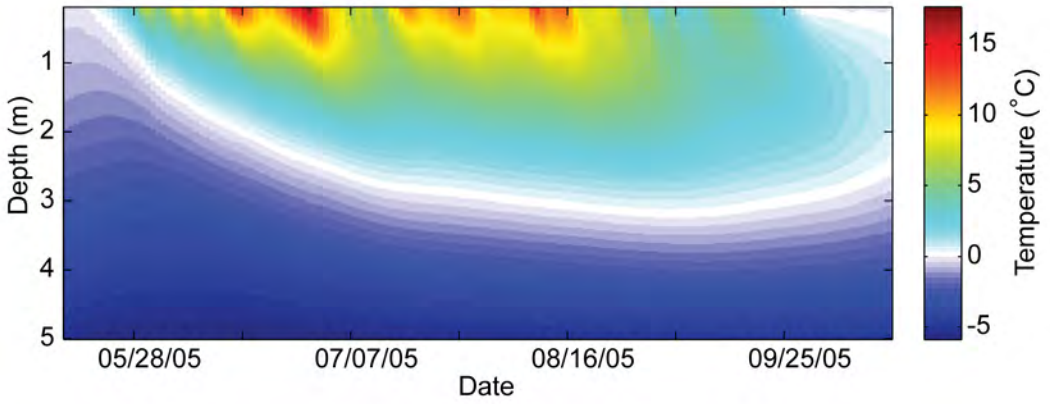

Figure 5.8. Simulated temperature results for 8I 2005. (a) Comparison between observed temperatures, thermal model with conduction, and thermal model with conduction and convection term. (b) Isotherm plot of modeled temperatures at depth.

5.5.2 8O Site

Temperatures recorded in 2005 at the 8O site illustrate an overall dampened temperature signature, due to the lake effect, where a maximum temperature peak of ~13 ˚C was reached briefly at 0.40 m on June 16 (Figure 5.9). Otherwise, all temperature depths at 8O remained below 8 ˚C with a consistent temperature gradient from shallow to deep observed temperature depths throughout the summer months (Figure 5.9b). Daily temperature averages at all depths were above 0 ˚C by early June and did not return to temperatures at or below 0 ˚C until October 21 (almost a full month later in comparison to 8I temperatures).

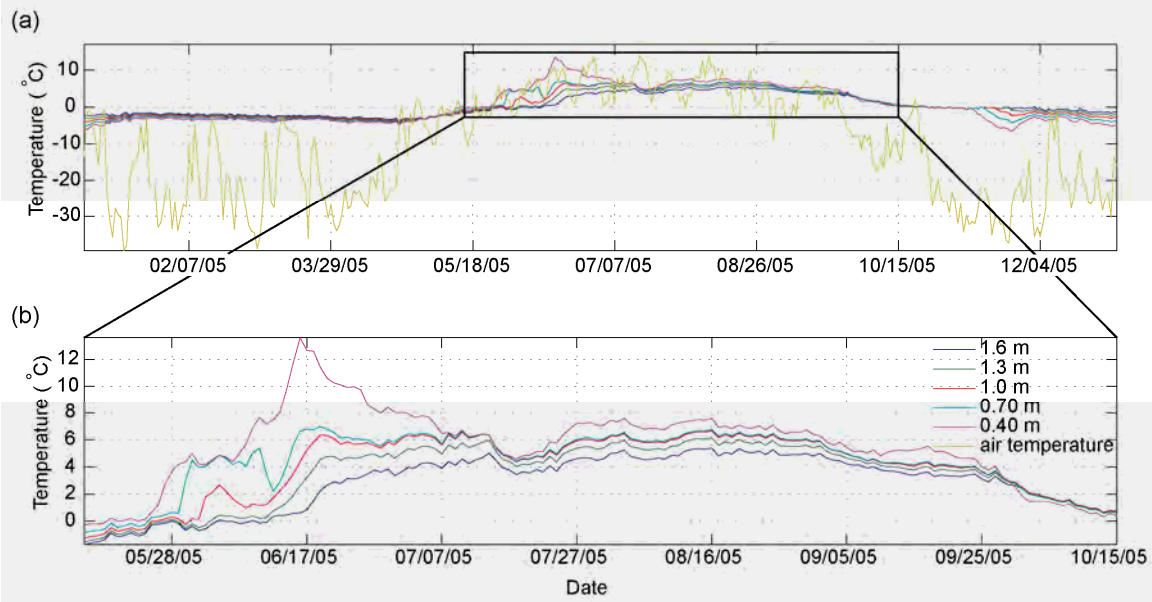

Figure 5.9. Daily average temperature profile recorded at the 8O stream site. (a) Recorded temperatures for 2005 with temperatures measured from 0.40 to 1.6m depth at 0.30m increments. Air temperatures were recorded at the Toolik Field Station Meteorological Station [*Shaver*, 2005]. (b) Subset of the recorded temperatures used for model validation (15 May to 15 October).

The same model parameters used at 8I were also applied to the 8O thermal model except for the volumetric water content value. The multi-offset GPR transect gathered across the 8O temperature site was complicated by scattering attenuation; however, a stacking velocity of 0.085 m ns^{-1} displayed a reflection interpreted as the thaw bulb/permafrost boundary [*Brosten et al.*, in review] with a maximum thaw bulb thickness of 3.4 ± 0.42 m. Using the normal move-out velocity of 0.085 m ns^{-1} we use the Topp equation [*Topp et al.*, 1980] and estimate the bulk water content at 23% (7% less than the 8I site).

Temperature differences between simulated and observed temperatures at 0.70, 1.0, 1.3, and 1.6 m also progressively increased with depth except during the period where temperatures spiked at 0.40 m depth from June 6 to July 7 (Figure 5.10). Temperature

differences at the 1.6 m depth interval averaged 1.3 ˚C with a maximum difference of 1.6 ˚C on July 13 (Figure 5.11d). Model results estimated a maximum thaw depth at 2.88m on August 29 (Figure 5.11). Compared to the multi-offset GPR transect collected on August 7, with an estimated thaw depth of 3.4 ± 0.42 m, the thermal model underestimates the thaw depth with a value at 2.78 ± 0.05 m.

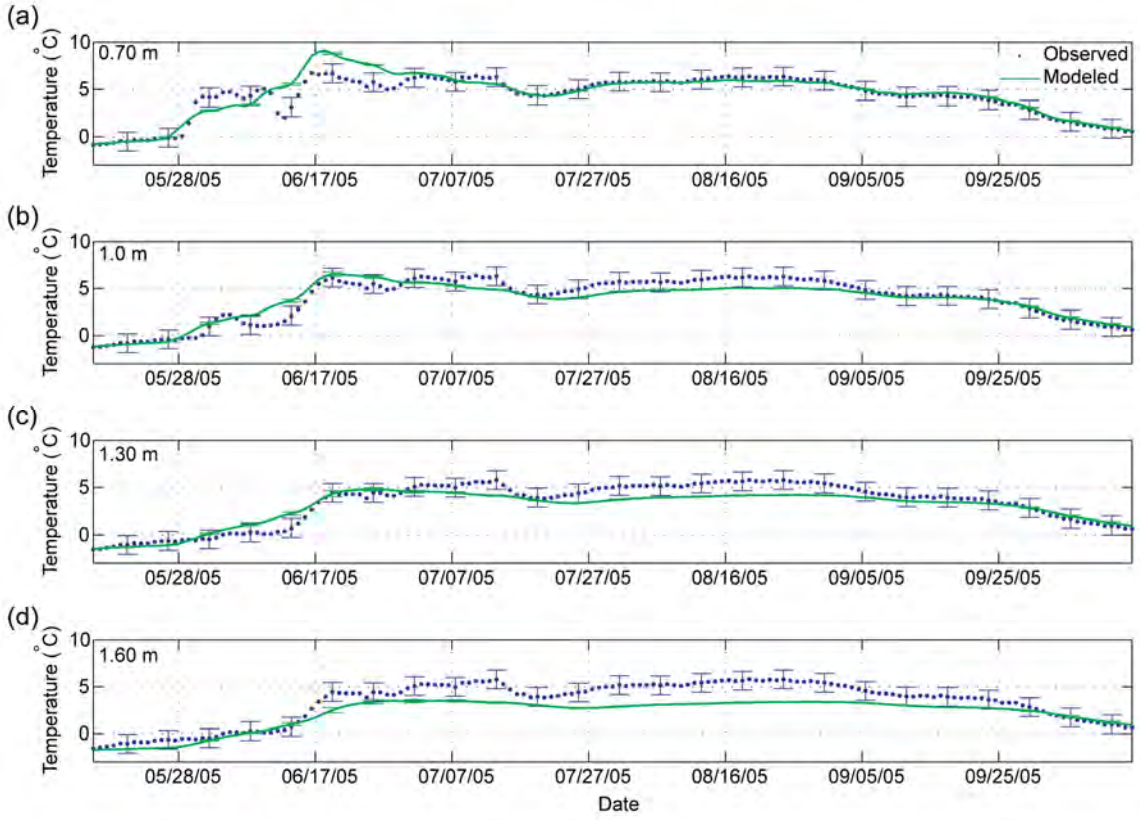

Figure 5.10. Comparison between 2005 daily averaged predicted and observed temperatures at (a) 0.70m; (b) 1.0m; (c) 1.30m; and (d) 1.60m.

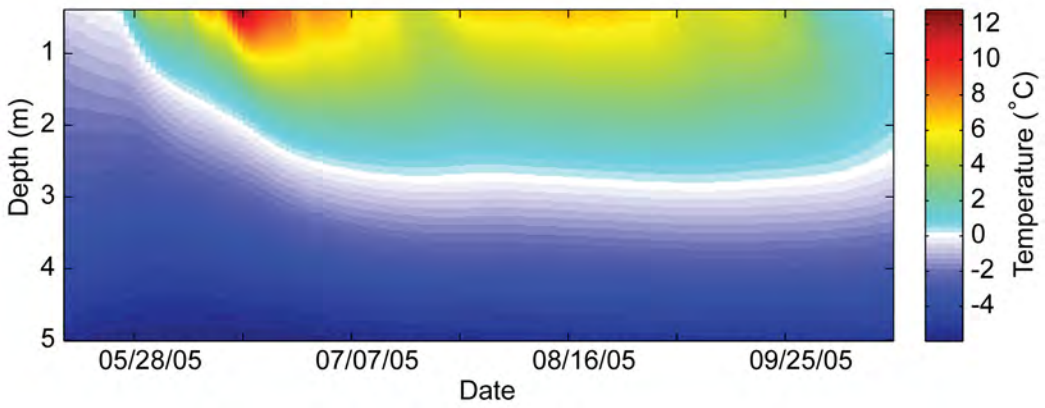

Figure 5.11. Simulated temperature results for 8O 2005. (a) Comparison between observed temperatures, thermal model with conduction, and thermal model with conduction and convection term. (b) Isotherm plot of modeled temperatures at depth.

5.5.3 PI Site

The PI site is significantly different from the gravel-lined sites in its physical characteristics (e.g. material lining, slope, and channel water depth) and seasonal thermal response. Observed temperatures at 0.18 and 0.38 m depths were much slower to warm in response to the seasonal thermal processes with a more apparent temperature gradient between the two depths throughout the 2004 season (Figure 5.12) with temperature differences, between measurement depths, ranging up to 6 ˚C.

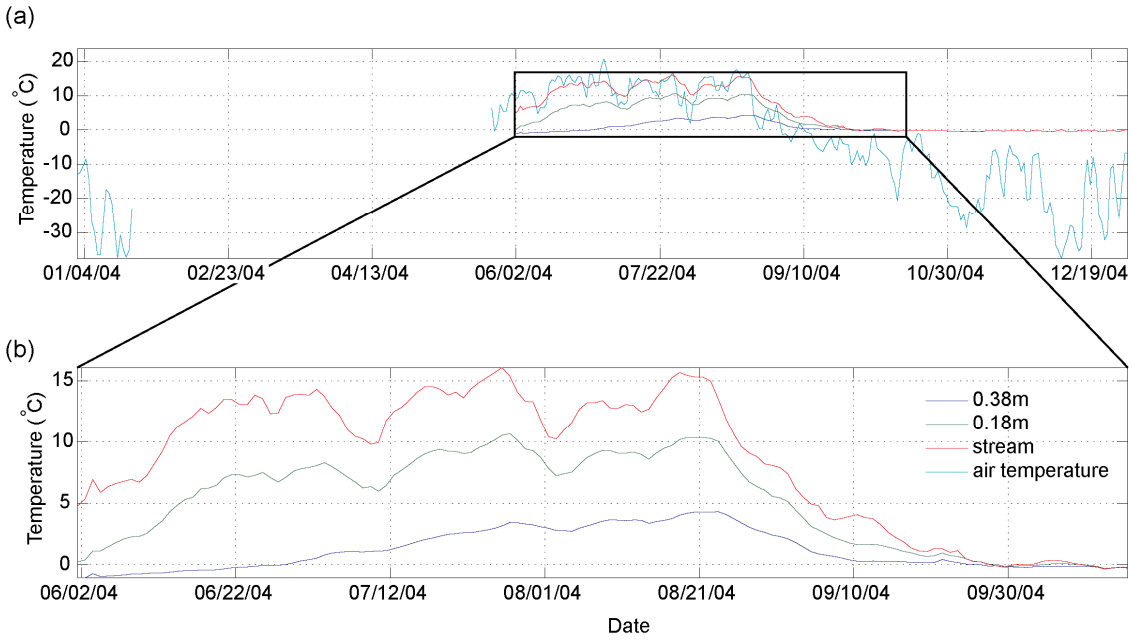

Figure 5.12. Daily average temperature profile recorded at the PI stream site. (a) Recorded temperatures for 2004 (temperature logging started May 28, 2004) with temperatures measure at stream water, 0.18m, and 0.38m. Air temperatures were recorded at the Toolik Field Station Meteorological Station [*Shaver*, 2004]. (b) Subset of the recorded temperatures used for model validation (1 June to 15 October).

Parameter values for the thermal model at PI include a thermal conductivity value of 0.25 W m^{-1}°C and a soil density of 700 kg m^{-3}. The volumetric water content, calculated from the multi-offset GPR transect, was estimated at ~0.50. A study of the hyporheic flow in 2005 at the PI stream site indicates subsurface flow occurring at depths no greater than 0.15 m [*Zarnetske et al.*, 2008] indicating little to no heat addition from subsurface flow. The resulting model progressively overestimate measured temperatures at 0.18 and 0.38 m with estimated temperatures exceeding the measured temperatures up to 3 ˚C at 0.18m and 6 ˚C at the 0.38 m depth interval (Figure 5.13). Model results estimate a maximum thaw depth of 1.06 m on September 6 (Figure 5.14a). A comparison between GPR thaw depth estimates to the modeled zero degree isotherm illustrates

consistently greater thaw depth estimates from the model throughout the 2004 season (Figure 5.14b).

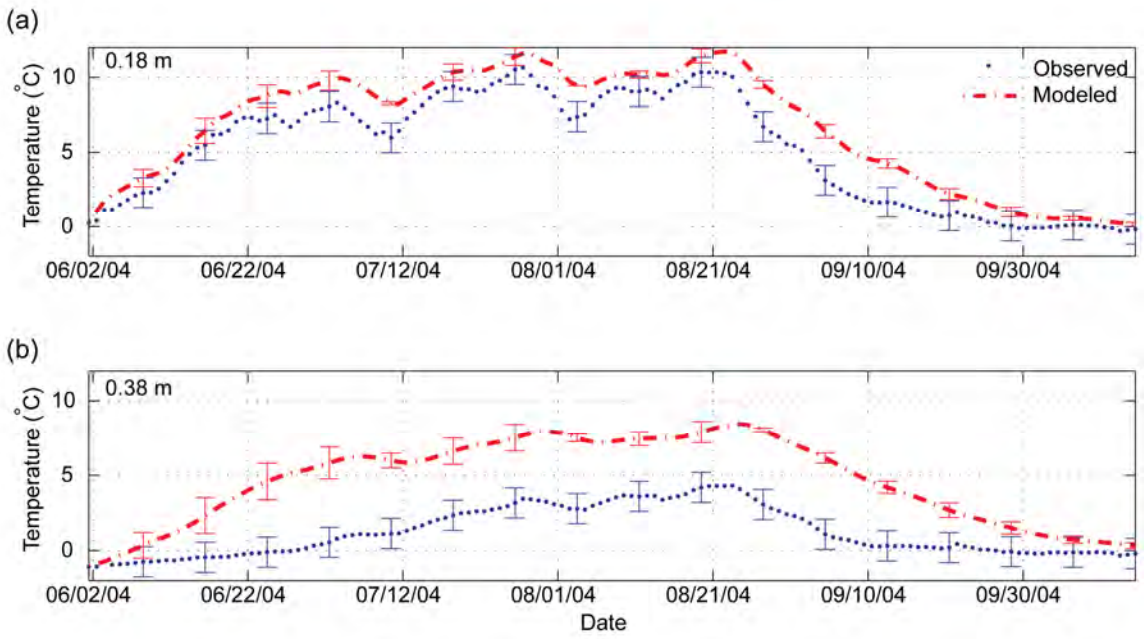

Figure 5.13. Simulated temperature results for PI 2004. Comparison between observed temperatures, thermal conduction model at (a) 0.18m and (b) 0.38m.

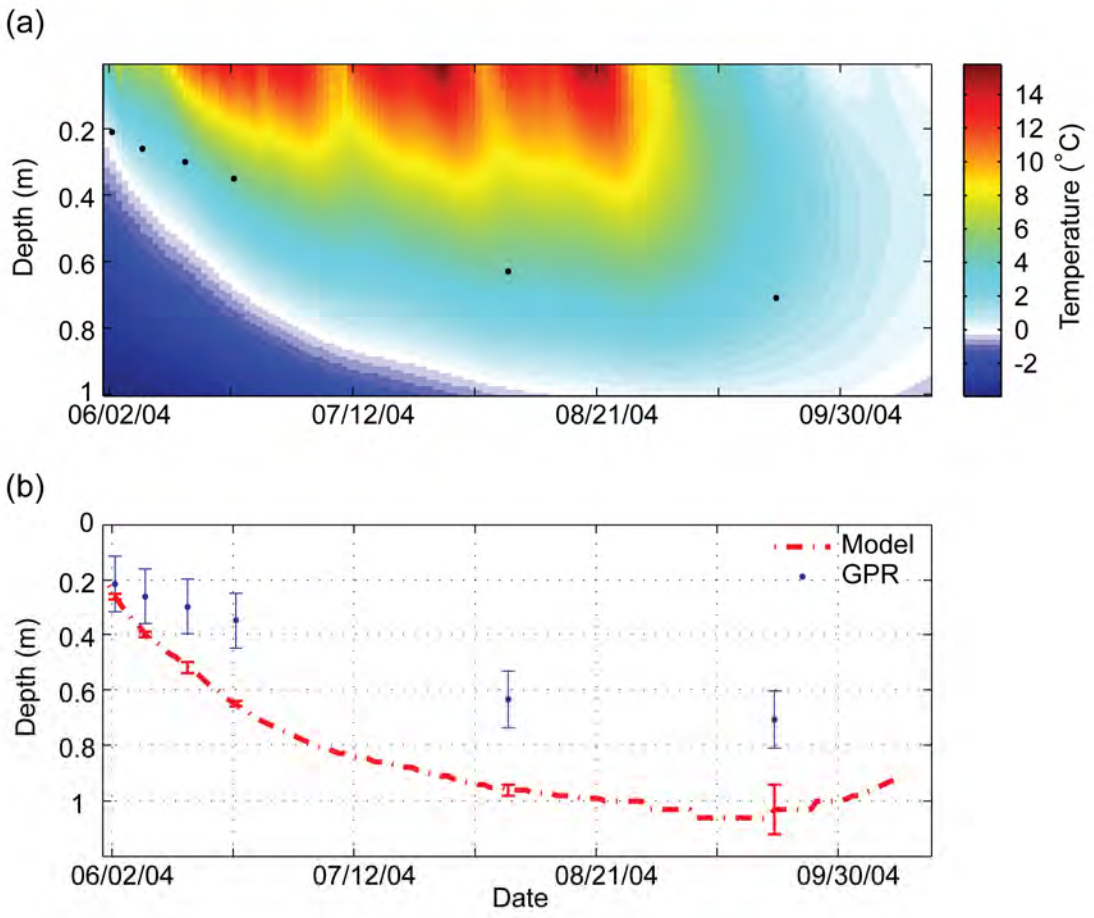

Figure 5.14. (a) Isotherm plot of modeled temperatures at depth for PI 2004. (●) represents thaw depth estimates from GPR transects collection on June 2, 7, 14, and 22, August 6, and September 19, 2004. (b) Comparison between the zero degree isotherm estimated from the thermal model, at depth, and estimated maximum thaw depths from GPR transects.

5.6 Discussion

Daily average temperature profiles at 8I show that values for the two shallowest depths (0.20 and 0.40 m) are nearly identical for most of the season throughout the summer (Figure 5.4 and Figure 5.5) implying a homogenous layer between these two depths with nearly identical response to thermal processes within the hyporheic zone. In addition these same temperatures invert periodically throughout the season (i.e.

temperatures at shallow depths become colder than temperatures at deeper depths) and may be responding to variations in seasonal temperatures.

Results from the thermal models for 8I illustrate conduction as the primary contributor to seasonal thaw. The enhanced conduction term improved results by removing the time lag between the observed and predicted peaks and troughs; however, improvements in temperature amplitudes from advective influence were minimal which implies an insignificant contribution to seasonal thaw. Estimated thaw depth comparisons between the GPR interpretations and predicted temperatures for 2004 were in good agreement for the first four GPR acquisition dates. In September the thaw depth interpreted from the GPR data, 2.0 ± 0.33 m, was ~1 m shallower than the predicted model, 3.15 ± 0.05 m (Figure 5.7b). Model assumptions including homogeneous soil properties, oversimplification of convective influence, and 1D model assumptions all contribute to discrepancies between the modeled results and true temperatures.

Observed temperatures at 8O are significantly different from 8I due to the lake effect which acts as a heat sink. As warm water enters the lake much of its heat is lost from mixing with the colder lake water. Temperatures of water exiting the lake have been dampened to a lower more constant temperature due to lake volume and residence time within the lake. The thermocouple site located less than 100 m downstream of the lake outlet provides channel water temperatures representative of the lake effect given the short distance for influence from season thermal radiation from the gravel bed lining material.

Predicted temperatures at 8O were, overall, in better agreement with the observed temperatures due to less thermal heterogeneity in comparison to the 8I modeled results. Influence from advective processes at 8O is negligible where the driving boundary, located at the 0.40 m depth interval, is below depths where advection would be greatest. The largest discrepancy between observed and predicted temperatures occurs from June 6 to July 13 and is caused by the large temperature increase at 0.40 m that occurred over the same time period (Figure 5.9b). Since the recorded temperatures at 0.40 m were used as the driving boundary for the model the same temperature anomaly propagated downward becoming less prevalent at greater depths (Figure 5.10).

The thaw depth estimate from the GPR transect recorded on August 7, 2005 was greater than the thermal model estimate (3.4 ± 0.42 m vs. 2.78 ± 0.05 m) and is also greater than any of the interpreted GPR transects recorded at 8I. The existence of greater thaw depths at 8O are likely caused by the presence of larger exposed black rocks above the water line resulting in greater amounts of thermal radiation transferring into the subsurface. Observed temperatures also remain above 0 ˚C for an additional month compared to 8I temperatures possibly due to greater amounts of heat from radiation processes. The cause for underestimated thaw depths from the thermal model are attributed to soil heterogeneities creating heat flow paths not accounted for in the model.

Model results from the PI site compared poorly to the observed temperatures with overestimated temperature values at 0.18 and 0.38 m throughout the summer period, May to September (Figure 5.13). The rapid deviation between measured and modeled values at depth between 0.18 and 0.38 m implies assumptions not representative of the true

conditions. An inaccurate representation of unfrozen water content could be the primary cause of modeled temperature over-estimations. Observed temperatures illustrate a slow response to seasonal temperatures and a consistent thermal gradient that could be caused by a low thermal conductivity from greater amounts of unfrozen water mixed with frozen peat material occurring over a larger temperature range than what has been modeled.

Thaw depth estimates from GPR transects imply a slow thaw response that may continue to thicken past the last GPR acquisition in September (Figure 5.14). The thermal model illustrates a more rapid response, compared to the GPR interpretations, to seasonal temperatures; however, the trend of the zero degree isotherm is very similar to the GPR thaw depth interpretations indicating refreezing of the active layer soon after the last GPR acquisition date.

Within the gravel-lined sites maximum thaw depths predicted from the thermal models appear to overestimate at the inlet site, 8I, and underestimate at the outlet site, 8O, compared with GPR interpretations. This implies differences in subsurface thermal property variations between the two sites not accounted for in the models. Predicted thaw depths at the PI site exceed GPR thaw depth estimates and are likely due to unfrozen water content that contributes to soil property variations not accounted for in the thermal model.

5.7 Conclusions

A 1D heat conduction transport model with phase change was used to simulate seasonal thaw beneath arctic streams. Results indicate thermal conduction as the primary

contributor to seasonal thaw. Modeled temperature magnitudes, using the effective conductivity values, did not change significantly compared to temperature results from conduction values alone supporting evidence that conduction is the primary heat transfer process. The additional advection term improved the model response by removing the time lag between the measured and predicted temperatures. Differences between modeled and true temperatures are, primarily, due to homogenous soil property assumptions made in the models that affect the amount of thermal contributions from conduction. This study utilizes two distinctly different methods for seasonal thaw depth verification beneath arctic streams (GPR and thermal modeling). Disagreement between the two methods indicates the need for soil property measurements in order to better constrain numerical model results.

REFERENCES

Al-Chalabi, M. (1973), Series approximation in velocity and traveltime computations, *Geophysical Prospecting*, *21*, 783-795.

Al-Chalabi, M. (1974), An analysis of stacking, RMS, average, and interval velocities over a horizontally layered ground, *Geophysical Prospecting*, *22*, 458-475.

Anderson, D. M., et al. (1973), The unfrozen water and the apparent specific heat capacity of frozen soils paper presented at Proceeding Second International Conference on Permafrost, National Academy of Sciences.

Anderson, N. L., et al. (2007), Ground-penetrating radar: A tool for monitoring bridge scour, *Environmental & Engineering Geoscience*, *13*(1), 1-10.

Annan, A. P., and J. L. Davis (1976), Impulse radar sounding in permafrost, *Radio Science*, *11*(4), 383-394.

Arcone, S. A., and A. J. Delaney (1982), Dielectric properties of thawed active layers overlying permafrost using radar at VHF, *Radio Science*, *17*, 618-626.

Arcone, S. A., et al. (1992), Short-pulse radar detection of groundwater in the Sagavanirktok River floodplain in early spring, *Water Resources Research*, *28*(11), 2925-2936.

Arcone, S. A., et al. (1993), Radar reflection and refraction profiles of seasonal thaw over permafrost in Fairbanks, Alaska, in *Proceedings of the second Government Workshop on Ground-Penetrating Radar*, edited, pp. 241-256.

Arcone, S. A., et al. (1998a), Seasonal structure of taliks beneath arctic streams determined with ground-penetrating radar, in *Proceedings of the seventh International Permafrost Conference* edited by A. Lewkowicz and A. M, pp. 19-24, International Permafrost Association, Canadian National Committee, Yellowknife, Canada.

Arcone, S. A., et al. (1998b), Ground-penetrating radar reflection profiling of groundwater and bedrock in an area of discontinuous permafrost, *Geophysics*, *63*(5), 1573-1584.

Arcone, S. A., and A. J. Delaney (2003), Radiowave pulse refraction and ground wave propagation through permafrost and the active layer, in *Proceedings of the eighth International Conference on Permafrost* edited, pp. 21-25, Zurich, Switzerland.

Arntzen, E. V., et al. (2006), Effects of fluctuating river flow on groundwater/surface water mixing in the hyporheic zone of a regulated, large cobble bed river, *River Research and Applications*, *22*, 937-946.

Arp, C. D., et al. (2007), Stream geomorphology in a mountain lake district: hydraulic geometry, sediment sources and sinks, and downstream lake effects, *Earth Surface Processes and Landforms*, *32*, 525-543.

Asprion, U., and T. Aigner (1999), Towards realistic aquifer models: three-dimensional georadar surveys of Quaternary gravel deltas (Singen Basin, SW Germany), *Sedimentary Geology*, *129*, 281-297.

Bear, J. (1972), *Dynamics of Fluids in Porous Media*, American Elsevier, New York.

Beres, M., et al. (1995), Mapping the architecture of glaciofluvial sediments with three-dimensional georadar, *Geology*, *23*(12), 1087-1090.

Best, H., et al. (2005), Association of ice and river channel morphology determined using ground-penetrating radar in the Kuparuk River, Alaska, *Arctic, Anarctic, and Alpine Research*, *37*(2), 157-162.

Bradford, J. H. (2003), GPR offset-dependent reflectivity analysis for characterization of a high-conductivity LNAPL plume, in *Proceedings of the Symposium on the Application of Geophysics to Environmental and Engineering Problems (SAGEEP)*, edited, pp. 238-252, Environmental and Engineering Geophysical Society, San Antonio, TX.

Bradford, J. H. (2004), 3D multi-offset, multi-polarization acquisition and processing of GPR data: A controlled DNAPL spill experiment, in *Proceedings of the Symposium on the Application of Geophysics to Environmental and Engineering Problems (SAGEEP)*, edited, pp. 514-527, Environmental and Engineering Geophysical Society.

Bradford, J. H., et al. (2005), Measuring thaw depth beneath peat-lined arctic streams using ground-penetrating radar, *Hydrological Processes*, *19*, 2689-2699.

Bradford, J. H. (2006), Applying reflection tomography in the postmigration domain to multifold ground-penetrating radar data, *Geophysics*, *71*(1), K1-K8.

Bradford, J. H., and J. C. Deeds (2006), Ground-penetrating radar theory and application of thin-bed offset-dependent reflectivity, *Geophyiscs*, *71*(3), K47-K57.

Bradford, J. H., and Y. Wu (2007), Time-frequency mapping via wavelet matching with application to 3D GPR contaminated site characterization, *The Leading Edge*, *26*, 1018-1023.

Bradford, J. H. (2008), Measuring lateral and vertical heterogeneity in vadose zone water distribution using multi-fold GPR with reflection tomography, *Vadose Zone Journal*, *7*(1), 184-193.

Brosten, T. R., et al. (2006), Profiles of temporal thaw depths beneath two arctic stream types using ground-penetrating radar, *Permafrost and Periglacial Processes*, *17*, 341-355.

Brosten, T. R., et al. (in review), Multi-offset GPR methods for hyporheic zone investigations, *Near Surface Geophysics*.

Cardenas, M. B., and J. L. Willson (2004), Impact of heterogeneity, bed forms, and stream curvature on subchannel hyporheic exchange, *Water Resources Research*, *40*, W08307.

Carman, P. C. (1937), Fluid flow through granular beds, *Transactions of the Institution Chemistry Engineering*, *15*, 150-166.

Cox, G. F. N., and W. F. Weeks (1975), Brine drainage and initial salt entrapment in sodium chloride ice 85 pp, U.S. Army Cold Regions Research and Engineering Lab, Hanover, NH.

Davis, J. L., and A. P. Annan (1977), electromagnetic detection of soil moisture: Progress report 1, *Canadian Journal of Remote Sensing*, *3*(1), 76-86.

Davis, J. L., and A. P. Annan (1989), Ground-penetrating radar for high-resolution mapping of soil and rock stratigraphy, *Geophysical Prospecting*, *37*, 531-551.

Deeds, J. L., and J. H. Bradford (2002), Characterization of an aquitard and direct detection of LNAPL at Hill Air Force Base using GPR AVO and migration velocity analysis, in *Proceedings of the ninth International Conference on Ground Penetrating Radar*, edited, pp. 323-329, International Society for Optical Engineering.

Delaney, A. J., et al. (1990), Winter short-pulse studies on the Tanana River, Alaska, *Arctic*, *43*(3), 244-250.

Dillard, D. S., and K. D. Timmerhaus (1966), Low temperature thermal conductivity of solidified H_2O and D_2O, *Pure Applied Cryogenics*, *4*, 35-44.

Dix, C. H. (1955), Seismic velocities from surface measurements, *Geophysics*, *34*, 180-195.

Doolittle, J. A., et al. (1990), A ground-penetrating radar study of active layer thicknesses in areas of moist sedge and wet sedge tundra near Bethel, Alaska, U.S.A., *Arctic and Alpine Research*, *22*(2), 175-182.

Doolittle, J. A., et al. (1992), A ground-penetrating radar study of Goodream Palsas, Newfoundland, Canada, *Arctic and Alpine Research*, *4*(2), 173-178.

Dorsey, N. E. (1940), *Properties of Ordinary Water-Substance*, 673 pp., Hafner, New York.

Edwardson, K. J., et al. (2003), The hydraulic characteristics and geochemistry of hyporheic and parafluvial zones in arctic tundra streams, North Slope, Alaska, *Advances in Water Resources*, *26*, 907-923.

Everdingen, R. V. (2005), Multi-language glossary of permafrost and related ground-ice terms, edited by R. V. Everdingen, Boulder, CO.

Fisher, E., et al. (1992), Acquisition and processing of wide-aperture ground-penetrating radar data, *Geophysics*, *57*(3), 495-504.

Fitts, C. R. (2002), *Groundwater Science*, Academic Press, San Diego.

Freed, J. S., et al. (2006), Geologic Map of the Deadwood River 30 x 60 Minute Quadrangle, Idaho, Idaho Geological Survey, 2006.

Goodrich, L. E. (1982), The influence of snow cover on teh ground thermal regime, *Canadian Geotechnical Journal*, *19*, 421-432.

Gooseff, M. N., et al. (2002), Weathering reactions and hyporheic exchange controls on stream water chemistry in a glacial meltwater stream in the McMurdo Dry Valleys, *Water Resources Research*, *38*(12), 1279.

Grasmueck, M. (1996), 3D ground-penetrating radar applied to fracture imaging in gneiss, *Geophyiscs*, *61*, 1050-1064.

Grasmueck, M., et al. (2004), Three-dimensional ground-penetrating radar imaging of sedimentary structures, fractures, and archaeological features at submeter resolution, *Geology*, *32*(11), 933-936.

Greaves, R. J., et al. (1996), Velocity variation and water content estimated from multi-offset, ground-penetrating radar, *Geophysics*, *61*(3), 683-695.

Greenwald, M. J., et al. (2008), Hyporheic exchange and water chemistry of two arctic tundra streams of contrasting geomorphology, *Journal of Geophysical Research, 113*.

Guidry, S. A., et al. (2007), Karst and early fracture networks in carbonates, turks and Caicos Islands, British West Indies, *Journal of Sedimentary Research, 77*, 508-524.

Hanafy, S., and S. A. Hagrey (2006), Ground-penetrating radar tomography for soil-moisture heterogeneity, *Geophysics*, *71*(1), K9-K18.

Harlan, R. L. (1973), Analysis of coupled heat-fluid transport in partially frozen soil, *Water Resources Research*, *9*(3), 1314-1323.

Harvey, J. W., and K. E. Bencala (1993), The effect of streambed topography on surface-subsurface water exchange in mountain catchments, *Water Resources Research*, *29*(1), 89-98.

Harvey, J. W., and B. J. Wagner (2000), *Quantifying hydrologic interactions between streams and their subsurface hyporheic zones*, Academic Press, San Diego.

Hill, A. R., et al. (1998), Hyporheic zone hydrology and nitrate dynamics in relation to the streambed topography of a N-rich stream, *Biogeochemistry*, *42*, 285-310.

Hinkel, K. M., et al. (2001), Detection of subsurface permafrost features with ground-penetrating radar, Barrow, Alaska, *Permafrost and Periglacial Processes, 12*, 179-190.

Hinzman, L. D., et al. (1991), Hydrologic and thermal properties of the active layer in Alaskan Arctic, *Cold Regions Science and Technology, 19*, 95-110.

Huisman, J. A., et al. (2003), Measuring soil water content with ground-penetrating radar: A review, *Vadose Zone Journal, 2*, 476-491.

Incropera, F. P., and D. P. DeWitt (2002), *Fundamentals of heat and mass transfer*, 5 ed., 981 pp., John Willey & Sons, Inc.

Jame, Y. W., and D. J. Norum (1980), Heat and mass transfer in a freezing unsaturated porous medium, *Water Resources Research, 16*(4), 811-819.

Jones, J. B., et al. (1995), Nitrification in the hyporheic zone of a desert stream ecosystem, *Journal of the North American Benthological Society, 14*, 249-258.

Jorgenson, M. T., et al. (2000), Permafrost degradation and ecological changes associated with a warming climate in central Alaska, *Climate Change, 48*(4), 551-579.

Kane, D. L., et al. (1991), Thermal response of the active layer to climatic warming in permafrost environment, *Cold Regions Science and Technology, 19*, 111-122.

Kasahara, T., and S. M. Wondzell (2003), Geomorphic controls on hyporheic exchange flow in mountain streams, *Water Resources Research, 39*(1), 1005.

Kostic, B., and T. Aigner (2007), Sedimentary architecture and 3D ground-penetrating radar analysis of gravelly meandering river deposits (Neckar Valley, SW Germany), *Sedimentology, 54*, 789-808.

Kruse, S., et al. (2006), Sinkhole structure imaging in covered karst terrain, *Geophysical Research Letters*, *33*, L16405.

Lachenbruch, A. H., et al. (1982), Permafrost, heat flow, and the geothermal regime at Prudhoe Bay, Alaska, *Journal of Geophysical Research, 87*(B11), 9301-9316.

Lachenbruch, A. H., and B. V. Marchall (1986), Changing climate: geothermal evidence from permafrost in the Alaskan Arctic, *Science, 234*, 689-696.

Lane, J. W. J., et al. (2006), Geophysical monitoring of a field-scale biostimulation pilot project, *Ground Water*, *44*, 440-443.

Leckebush, J. (2003), Ground-penetrating radar: A modern three-dimensional prospection method, *Archaeological Prospection, 10*, 213-240.

Leucci, G., and S. Negri (2006), Use of ground penetrating radar to map subsurface archaeological features in an urban area, *Journal of Archaeological Science, 33*, 502-512.

Liberty, L. M., and J. R. Pelton (1994), A comparison of ground-penetrating radar methods: Multi-fold data vs. single fold data, in *30th Symposium on Engineering Geology and Geotechnical Engineering: Hydrogeology, Waste Disposal, Science and Politics*, edited by P. K. Link, pp. 321-324, Pocatello, ID.

Ling, F., and T. Zhang (2004), A numerical model for surface energy balance and thermal regime of the active layer and permafrost containing unfrozen water, *Cold Regions Science and Technology, 38*, 1-15.

LTER (2004), Arc LTER Weather Data, edited, Toolik Lake Main.

Lumley, D. E. (2001), Time-lapse seismic reservoir monitoring, *Geophyiscs, 45*, 312-322.

Lunt, I. A., et al. (2005), Soil moisture content estimation using ground-penetrating radar reflection data, *Journal of Hydrology, 307*, 254-269.

MacBeth, C. M., et al. (2006), Going quantitative with 4D seismic analysis, *Geophiscal Prospecting*, *54*, 303-317.

Miller, C. R., et al. (2008), Application of time-lapse ERT imaging to watershed characterization, *Geophyiscs*, *73*(3), G7-G17.

Moorman, B. J., et al. (2003), Imaging periglacial conditions with ground-penetrating radar, *Permafrost and Periglacial Processes*, *14*, 319-329.

Morrice, J., et al. (1997), Aluvial characteristics, groundwater-surface water exchange and hydrological retention in headwater streams, *Hydrological Processes*, *11*, 253-269.

Mulholland, P. J., et al. (1997), Evidence that hyporheic zones increase heterotrophic metabolism and phosphorous uptake in forest streams, *Limnology and Oceanography*, *42*, 443-451.

Munroe, J. S., et al. (2007), Aplication of ground-penetrating radar imagery for three-dimensional visualization of near-surface structures in ice-rich permafrost, Barrow, Alaska, *Permafrost and Periglacial Processes*, *18*, 309-321.

Nakano, Y., and J. Brown (1972), Mathematical modeling and validation of teh thermal regimes in tundra soils, Barrow, Alaska, *Arctic and Alpine Research*, *4*(1), 19-28.

Negri, S., and G. Leucci (2006), Geophysical investigation of the Temple of Apollo (Hierapolis, Turkey), *Journal of Archaeological Science*, *33*, 1505-1513.

Olhoeft, G. R. (1981), Electrical properties of rocks, in *Physical properties of rocks and minerals*, edited by Y. S. Touloukian, et al., pp. 257-330, McGraw-Hill.

Osterkamp, T. E., and M. W. Payne (1981), Estimates of permafrost thickness from well logs in northern Alaska, *Cold Regions Science and Technology*, *5*, 13-27.

Osterkamp, T. E. (1987), Freezing and thawing of soils and permafrost containing unfrozen water or brine, *Water Resources Research*, *23*(12), 2279-2285.

Osterkamp, T. E., and J. P. Gosink (1991), Variations in permafrost thickness in response to changes in paleoclimate, *Journal of Geophysical Research*, *94*(B3), 4423-4434.

Osterkamp, T. E., et al. (1994), Evidence for a cyclic variation of permafrost temperatures in northern Alaska, *Permafrost and Periglacial Processes*, *5*, 101-110.

Osterkamp, T. E. (1995), Further evidence for warming and thawing of permafrost in Alaska, *EOS, Transactions of the American Geophysical Union*, *76*(46), F244.

Osterkamp, T. E., and V. E. Romanovsky (1996), Characteristics of changing permafrost temperature in the Alaskan Arctic, U.S.A., *Arctic and Alpine Research*, *28*(3), 267-273.

Osterkamp, T. E., and V. E. Romanovsky (1997), Freezing of the active layer on the coastal plain of the Alaskan Arctic, *Permafrost and Periglacial Processes*, *8*, 23-44.

Osterkamp, T. E., and V. E. Romanovsky (1999), Evidence for warming and thawing of discontinuous permafrost in Alaska, *Permafrost and Periglacial Processes*, *10*, 17-37.

Osterkamp, T. E., et al. (2000), Observations of thermokarst in boreal forests in Alaska, *Arctic, Anarctic, and Alpine Research*, *32*(3), 303-315.

Osterkamp, T. E. (2003), Establishing long-term permafrost observatories for active-layer and permafrost investigations in Alaska: 1977-2002, *Permafrost and Periglacial Processes*, *14*, 331-342.

Pickens, J. F., and G. E. Grisak (1981), Scale-dependent dispersion in a stratified granular aquifer, *Water Resources Research*, *17*(4), 1191-1211.

Pilon, J. A., et al. (1985), Monitoring permafrost ground conditions with ground probing radar (G.P.R.), US Army Corps of Engineers, Cold Regions Research and Engineering Laboratory, Golden, Colorado.

Pipan, M., et al. (1999), 2-D and 3-D processing and interpretation of multi-fold ground penetrating radar: A case history from an archaeological site, *Journal of Applied Geophysics*, *41*, 271-292.

Pipan, M., et al. (2003), Multifold ground-penetrating radar and resistivity to study the stratigraphy of shallow unconsolidated sediments, *The Leading Edge*, *22*, 876-881.

Ponizovsky, A. A., et al. (1999), Performance of TDR calibration models as affected by soil texture, *Journal of hydrology*, *218*, 35-43.

Riseborough, D. H. (2002), The mean annual temperature at the top of permafrost, the TTOP model, and the effect of unfrozen water, *Permafrost and Periglacial Processes*, *11*, 219-239.

Romanovsky, V. E., and T. E. Osterkamp (1995), Interannual variations of the thermal regime of the active layer near-surface permafrost in Northern Alaska, *Permafrost and Periglacial Processes*, *6*, 313-335.

Romanovsky, V. E., and T. E. Osterkamp (1997), Thawing of the active layer on the coastal plain of the Alaskan Arctic, *Permafrost and Periglacial Processes*, *8*, 1-22.

Romanovsky, V. E., and T. E. Osterkamp (2000), Effects of unfrozen water on heat and mass transport processes in the active layer and permafrost, *Permafrost and Periglacial Processes*, *11*, 219-239.

Schwamborn, G. J., et al. (2002), High-resolution seismic and ground-penetrating radar - geophysical profiling of a thermokarst lake in the western Lena delta, northern Siberia, *Permafrost and Periglacial Processes*, *13*, 259-269.

Scott, W. J., et al. (1990), Geophysics in the study of permafrost, in *Geotechnical and Environmental Geophysics, Vol. 1: Review and Tutorial*, edited.

Shaver, G. (2004), Daily weather summaries from Toolik Field Station Meteorological Station, Toolik Lake, Alaska for 2004, edited.

Shaver, G. (2005), Daily weather summaries from Toolik Field Station Meteorological Station, Toolik Lake, Alaska for 2005, edited.

Stork, C. (1992), Reflection tomography in the postmigrated domain, *Geophysics*, *57*(5), 680-692.

Tice, A. R., et al. (1981), Unfrozen water contents of submarine permafrost determined by nuclear magnetic resonance, *Engineering Geology*, *18*, 135-146.

Topp, G. C., et al. (1980), Electromagnetic determination of soil water content; measurements in coaxial transmission lines, *Water Resources Research*, *16*, 574-582.

Touloukian, Y. S., et al. (1970), *Thermophysical Properties of Matter*, Plenum, New York.

Vervier, P., et al. (1993), Role of interaction zones between surface and ground waters in DOC transport and processing: Considerations for river restoration, *Freshwater Biology*, *29*, 275-284.

Wankiewicz, A. (1982), Hydrothermal processes beneath arctic river channels, *Water Resources Research*, *20*(10), 1417-1426.

Williams, P. J., and M. W. Smith (1989), *The Frozen Earth: Fundamentals of Geocryology*, 306 pp., University Press, Cambridge.

Wondzell, S. M., and F. J. Swanson (1999), Floods, channel change, and the hyporheic zone, *Water Resources Research*, *35*, 555-567.

Wong, J., et al. (1977), Permafrost: electrical properties of the active layer. In situ, *Canadian Journal of Earth Science*, *14*, 582-586.

Woo, M.-k., and Z. Xia (1996), Effects of hydrology on the thermal conditions of the active layer, *Nordic Hydrology*, *27*, 129-142.

Wright, K. K., et al. (2005), Restricted hyporheic exchange in an alluvial river system: implications for theory and management, *Journal of the North American Benthological Society*, *24*(3), 447-460.

Wroblicky, G. J., et al. (1998), Seasonal variation in surface-subsurface water exchange and lateral hyporheic area of two stream-aquifer systems, *Water Resources Research*, *34*(3), 317-328.

Yilmaz, O. (2001), *Seismic data analysis*, Society of Exploration Geophysicist.

Zarnetske, J. P., et al. (2007), Transient storage as a function of geomorphology, discharge, and permafrost active layer conditions in Arctic tundra streams, *Water Resources Research*, *43*, W07410.

Zarnetske, J. P., et al. (2008), Influence of morphology and permafrost dynamics on hyporheic exchange in arctic headwater streams under warming climate conditions, *Geophysical Research Letters*, *35*, L24405.

Zhang, T., and T. E. Osterkamp (1993), Climate and permafrost temperatures in Alaska north of the Brooks Range, *EOS, Transactions of the American Geophysical Union*, *74*(16), 89.

Zhang, T., et al. (1996), Influence of the depth hoar layer of the seasonal snow cover on the ground thermal regime, *Water Resources Research*, *32*(7), 2075-2086.

Zhang, T., and K. Stamnes (1998), Impact of climatic factors on the active layer and permafrost at Barrow, Alaska, *Permafrost and Periglacial Processes*, *9*, 229-246.

APPENDIX A

Wave Propagation

WAVE PROPAGATION

Radar propagation is limited by the conductivity of the medium where only in low-loss media can radar penetrate deep enough for a useful subsurface image. To derive the wave equation for an EM wave propagating in a conductor we will start with Maxwell's equations. Combining Faraday's law, $\nabla \times \vec{E} = -\frac{\partial \vec{B}}{\partial t}$ with Ampere's law, $\nabla \times \vec{H} = \vec{J} + \frac{\partial \vec{D}}{\partial t}$, in addition to the constitutive relationships yields the following electric field wave equation for a homogeneous isotropic medium,

$$\nabla^2 \vec{E} = \mu\sigma \frac{\partial \vec{E}}{\partial t} + \mu\varepsilon \frac{\partial^2 \vec{E}}{\partial t^2}, \tag{A.1}$$

where $\vec{E}$ is the electric field strength vector (V/m), $\vec{B}$ is the magnetic flux density vector (T), $\vec{D}$ is the electric displacement vector (C/m^2), $\vec{H}$ is the magnetic field intensity (A/m), $\vec{J}$ is the electric current density vector (A/m^2), t is time (s), and ε, μ, and σ are the electric permittivity, magnetic permeability, and conductivity of the medium. The first term on the right side (A.1) represents conduction effects by the applied electric field and the second term describes the polarization effects caused by the field.

A solution to equation (A.1) of the form

$$\vec{E} = \vec{E}_0 e^{i(kx - \omega t)} \tag{A.2}$$

yields the complex wave number squared

$$k^2 = \mu\varepsilon\omega^2 + i\mu\sigma\omega. \tag{A.3}$$

Taking the square root of equation (A.3) and solving for the real and imaginary parts the wave number k can be written as

$$k = \alpha + i\beta\,, \tag{A.4}$$

where the real part of the wave number is described by

$$\alpha = \frac{\omega}{c}\left[\frac{K}{2}\left(\sqrt{1+\tan^2\delta}+1\right)\right]^{\frac{1}{2}} \tag{A.5}$$

and the imaginary part of the wave number, attenuation coefficient, and is described by

$$\beta = \frac{\omega}{c}\left[\frac{K}{2}\left(\sqrt{1+\tan^2\delta}-1\right)\right]^{\frac{1}{2}}. \tag{A.6}$$

The parameters c and K_e are the velocity of an electromagnetic wave in free space, $c = \frac{1}{\sqrt{\mu_0\varepsilon_0}}$, and the dielectric permittivity of the medium, $K = \frac{\varepsilon}{\varepsilon_0}$, respectively, where ε_0 is the dielectric permittivity of free space, $8.85\times10^{-12}\,F/m$, and μ_0 is the magnetic permeability of free space. For a plane-wave propagating with the angular frequency, ω, the loss tangent, $\tan\delta$, is the ratio of conduction to displacement current density assuming that both σ and ε are real

$$\tan\delta = \frac{\sigma}{\omega\varepsilon}. \tag{A.7}$$

GPR is most effective when the loss tangent is very small and the diffusion term can be neglected. Such that $\tan\delta << 1$, the wave number reduces to

$$\alpha = \frac{\omega}{c}\sqrt{K}\,, \tag{A.8}$$

and the velocity, *v*, is frequency independent given by

$$v \approx \frac{\omega}{\alpha} \approx \frac{c}{\sqrt{K}}. \qquad \text{(A.9)}$$

This discussion of the wave equation does not consider material properties that are also frequency dependent in which case they should be treated as complex numbers. In the frequency range of GPR, 10 MHz - 1 GHz, the frequency dependence of the dielectric permittivity can be assumed to be constant [*Davis and Annan*, 1989]. In the research presented in this dissertation we treat the dielectric permittivity as real and related it to the propagation velocity by the expression found in equation (A.9). We acknowledge that frequency dependence, in addition to, scattering loss, source/receiver antenna power, transmission characteristics, and ground coupling are not accounted for and assume that these factors change much more slowly than the dielectric permittivity and are therefore, neglected.

APPENDIX B

Petrophysical Relationship

PETROPHYSICAL RELATIONSHIP

The complex dielectric permittivity, K^*, (sometimes called the complex dielectric constant) is given by Topp et al. [1980] as

$$K^* = K + \left(K' + \frac{\sigma}{\omega \varepsilon_0} \right) i, \tag{B.1}$$

where $K = \frac{\varepsilon}{\varepsilon_0}$, is the real part of the dielectric permittivity, ε_0 is the permittivity of a vacuum $8.85 \times 10^{-12} F/m$, and ε is the permittivity of the material. The imaginary part is the sum of two relaxation mechanisms where K' is the imaginary part of the dielectric permittivity representing the non-conductive part; $\frac{\sigma}{\omega \varepsilon_0}$ represents the conductive medium part where σ is the zero-frequency conductivity and ω is the angular frequency.

The electromagnetic (EM) wave velocity, *v*, defined by Topp et al. [1980] is

$$v = \frac{c}{\sqrt{K \frac{1 + \left\{ 1 + \tan^2 \delta \right\}^{\frac{1}{2}}}{2}}}, \tag{B.2}$$

where *c* is the velocity of an electromagnetic wave in free space (3×10^8 m/s) and the loss tangent, the ratio of the imaginary to real parts of the complex modulus, is

$$\tan \delta = \frac{\left\{ K' + \left(\frac{\sigma}{\omega \varepsilon_0} \right) \right\}}{K}. \tag{B.3}$$

Davis and Annan [1977] indicated that the dielectric loss of the imaginary part was much less than the real part in frequency ranges from 1 MHz to 1 GHz and if the loss tangent, $\tan\delta$, is much less than 1 and that the magnetic permeability of the soil, μ, is equal to that of free space, μ_0, then

$$v \approx \frac{c}{\sqrt{K}}. \tag{B.4}$$

With the assumption that the magnetic permeability is equal to that of free space and the electric conductivity is low Topp et al. [1980] developed an equation to obtain water content, θ_w, from the measured dielectric permittivity, *K*, where

$$K = 3.03 + 9.30(\theta_w) + 146.00(\theta_w)^2 - 76.70(\theta_w)^3. \tag{B.5}$$

While not measurable Topp et al. [1980] noted some electrical loss in their estimate of dielectric permittivity and therefore called their measured dielectric permittivity the apparent dielectric permittivity, K_a, where for low-loss nearly homogenous materials $K_a \approx K$.

Equation B.5 was determined from regression analysis of data obtained from four different soils with varying water content and clay. The inverse form of the Topp equation (B.5) has become one of the standard methods for estimating water content from dielectric measurements:

$$\theta_w = -5.3\times10^{-2} + 2.92\times10^{-4}(K) - 5.5\times10^{-4}(K)^2 + 4.3\times10^{-6}(K)^3. \tag{B.6}$$

The advantage of using the Topp equation to estimate water content is that only dielectric permittivity measurements are needed. The disadvantage is the empirical

nature of its development and limited accuracy when applied to materials different from the ones used to develop the relationship. For the purpose of this research we assume that the material properties at each arctic study site are similar to the electrical properties of soils used by Topp et al. [1980] keeping in mind that these values are an approximation.

APPENDIX C

Thermal Parameters for Conduction with Unfrozen Water Content

THERMAL PARAMETERS FOR CONDUCTION WITH UNFROZEN WATER CONTENT

An analytical solution presented by Osterkamp [1987] is used to account for effects of unfrozen water content on temperature dependent thermal properties for freezing and thawing soils within the active layer and near-surface permafrost. For this solution the phase boundary is diffuse where the amount of ice gradually increases and the amount of unfrozen water gradually decreases from the phase boundary. Thermal parameters needed for the conduction model include the thermal conductivity, apparent volumetric heat capacity, and thermal diffusivity.

Assuming a fully saturated system the thermal conductivity is a mixture of soil particles, unfrozen water, and ice and can be represented a geometric mean equation [*Ling and Zhang*, 2004]

$$K = K_s^{\theta_s} K_u^{\theta_u} K_i^{\theta_i} \tag{C.1}$$

where K_s, K_i, and K_u are the thermal conductivities of soil, ice, and water. The volumetric fractions of ice, θ_i, unfrozen water content, θ_u, and soil particles, θ_s, sum to one. The unfrozen water content is represented by a power law [*Tice et al.*, 1981] as

$$\theta_u = \left(\frac{\rho_b}{\rho_u} \right) a |T|^b \tag{C.2}$$

where ρ_b and ρ_u are the dry bulk densities the partially frozen soil and the unfrozen water, a and b are empirically derived material-dependent constants. The thermal conductivity for ice, K_i, is temperature dependent [*Dillard and Timmerhaus*, 1966] represented by

$$K_i = 0.4685 + \frac{488.19}{273.15 + T}, \tag{C.3}$$

and the temperature dependence equation for the thermal conductivity of unfrozen water content, K_u, [*Touloukian et al.*, 1970] is

$$K_u = 0.11455 + 1.6318 \times 10^{-3}\left(273.15 + T\right). \tag{C.4}$$

The apparent volumetric heat capacity for a mixture of soil particles, unfrozen water, and ice is calculated from

$$C = C_v - L\frac{\partial \theta_u}{\partial T} \tag{C.5}$$

where the volumetric heat capacity, C_v, is estimated by the weighted mean

$$C_v = \theta_s C_s + \theta_i C_i + \theta_u C_u, \tag{C.6}$$

C_s, C_i, and C_u are the volumetric heat capacities of the soil, ice, and unfrozen water. Substitute (C.2) into the second term on the right-hand side of (C.5) yields

$$L\frac{\partial \theta_u}{\partial T} = -\left(\frac{\rho_b}{\rho_u}\right) Lab\left|T\right|^{b-1}. \tag{C.7}$$

The volumetric heat capacity for peat particles, C_p, and silt particles, C_s, are [*Ling and Zhang*, 2004]

$$C_p = -0.1333 + 6.255 \times 10^{-3}\left(273.15 + T\right), \tag{C.8}$$

and

$$C_s = 0.4091 + 5.433 \times 10^{-3}\left(273.15 + T\right). \tag{C.9}$$

From Dorsey [1940], the volumetric heat capacity for ice is

$$C_i = 1.94 + 7.14 \times 10^{-3} \tag{C.10}$$

and the volumetric heat capacity for water is [*Cox and Weeks*, 1975]

$$C_u = 4.20843 + 1.11362 \times 10^{-1} T + 5.12142 \times 10^{-3} T^2 + 9.3482 \times 10^{-5} T^{-3}. \tag{C.11}$$

The volumetric latent heat for ice freezing from the water is [*Cox and Weeks*, 1975]

$$L = \rho_u \left(333.2 + 4.955T + 0.02987T^2\right). \tag{C.12}$$

Thermal conductivities used for peat and sand/gravel particles are 0.5 and 2.92 $Wm^{-1}°C^{-1}$, respectively, and were used in equations (C.1)-(C.4) to calculate values for thermal conductivities (Figure C.1). Equations (C.6) – (C.12) were substituted into equation (C.5) to estimate values for the apparent volumetric heat capacity (Figure C.1b). Water content estimates calculated from equation (C.2) are shown in Figure C.1c and, finally, the resulting diffusivity values, shown in Figure C.1d, represent values used in the heat transport equation (C.5) for peat and sand/gravel soils, respectively.

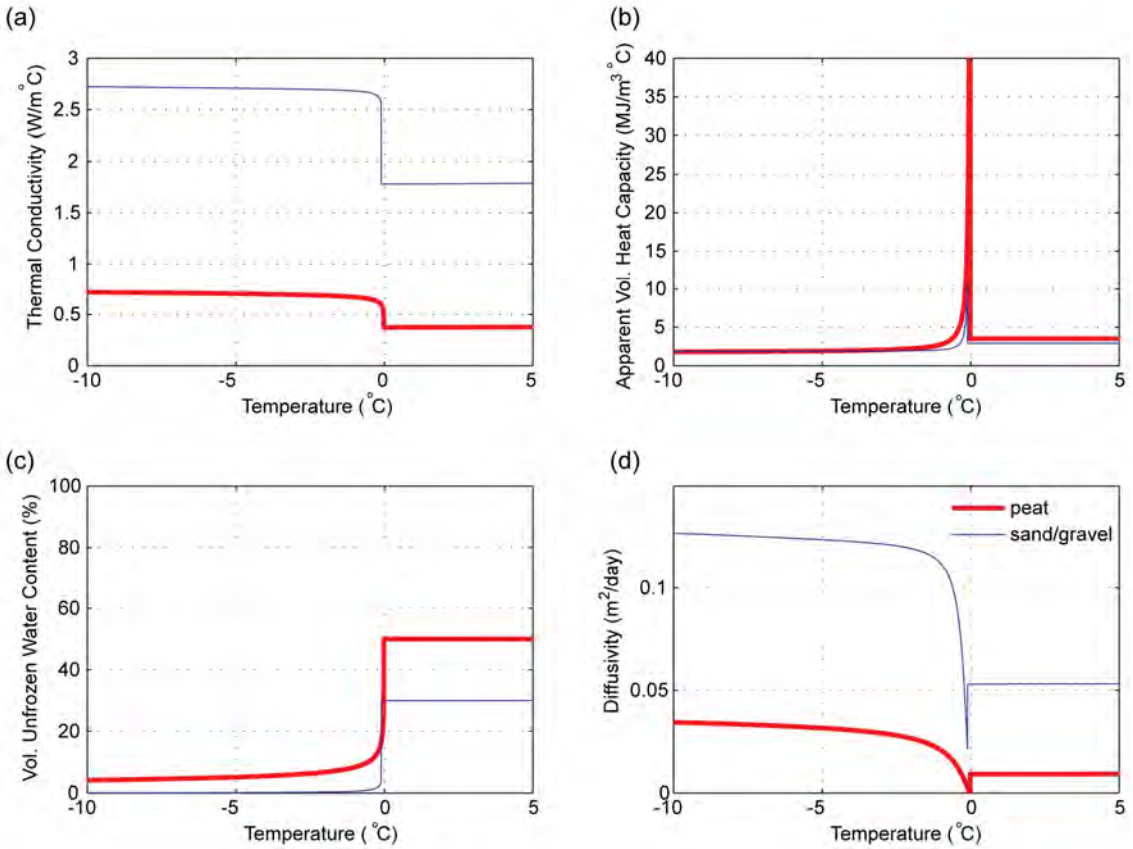

Figure C.1. Variations of (a) thermal conductivity, (b) apparent volumetric heat capacity, (c) volumetric water content, and (d) diffusivity with respect to temperature for peat and sand/gravel soils.